UNIVERSITY OF TRENTO - Italy

Freie Universität Berlin

Erasmus Mundus Joint Doctorate School in Science for MAnagement of Rivers and their Tidal System

---

Milad Niroumand-Jadidi

Rivers Hydromorphological Characterization from High Resolution Remotely Sensed Data

© DigitalGlobe. WorldView-2 image of Maipo River, Santiago, Chile.

Erasmus Mundus

Autumn, 2017

Doctoral thesis in “Science for Management of Rivers and their Tidal System”,

Cycle (IV)

Primary Institution: **Department of Civil, Environmental and Mechanical Engineering, University of Trento, Italy**

Secondary Institution: **Freie Universität Berlin, Berlin, Germany**

Associate Partner: **Leibniz Institute for Freshwater Ecology and Inland Fisheries (IGB), Berlin, Germany**

Supervisors

Prof. Alfonso Vitti, University of Trento

Prof. Franz Hölker, Leibniz Institute for Freshwater Ecology and Inland Fisheries (IGB), Berlin, Germany

Academic year **2014/2017**

The SMART Joint Doctorate Programme

Research for this thesis was conducted with the support of the Erasmus Mundus Programme[1], within the framework of the Erasmus Mundus Joint Doctorate (EMJD) SMART (Science for MAnagement of Rivers and their Tidal systems). EMJDs aim to foster cooperation between higher education institutions and academic staff in Europe and third countries with a view to creating centres of excellence and providing a highly skilled 21st century workforce enabled to lead social, cultural and economic developments. All EMJDs involve mandatory mobility between the universities in the consortia and lead to the award of recognised joint, double or multiple degrees.

The SMART programme represents collaboration among the University of Trento, Queen Mary University of London, and Freie Universität Berlin. Each doctoral candidate within the SMART programme has conformed to the following during their 3 years of study:

(i) Supervision by a minimum of two supervisors in two institutions (their primary and secondary institutions).

(ii) Study for a minimum period of 6 months at their secondary institution

(iii) Successful completion of a minimum of 30 ECTS of taught courses

(iv) Collaboration with an associate partner to develop a particular component / application of their research that is of mutual interest.

(v) Submission of a thesis within 3 years of commencing the programme.

[1]This project has been funded with support from the European Commission. This publication reflects the views only of the author, and the Commission cannot be held responsible for any use which may be made of the information contained therein

Acknowledgements

This thesis reflects the results of my PhD research during three years full of amazing experiences, collaborations and discoveries resulting in both academic and personal growth. My PhD completion would not have been possible without the support of family, friends and colleagues to whom I would like to express my gratitude.

First and foremost, I would like to thank Prof. Alfonso Vitti, my supervisor at University of Trento, who has helped me beyond words. He has provided me with great support through his insights, constructive comments, and his great personality and by giving me confidence to explore my ideas. In addition, I sincerely appreciate Prof. Franz Hölker, my supervisor in Berlin, and his colleague Dr. Andreas Jechow for their support and understanding throughout my research.

My great thanks go to the academic board of the SMART programme. I highly appreciate Prof. Guido Zolezzi for his management and support throughout the course of my PhD. My special thanks to Marina Rogato who always provided a solution for all my administrative requests. I would like to thank Prof. Katrin Premke, Dr. Ina Severin and Stefanie Burkert for their administrative support during my stay in Berlin.

I acknowledge the Imagery Grant awarded by DigitalGlobe Foundation and the kind responses from my contact persons Doven Libby and Dr. Fabio Pacifici. I highly appreciate the Alexander Goetz instrument support program of ASD Inc. for awarding me short-term usage of a spectroradiometer to perform my experiments. I am grateful to Prof. Aronne Armanini, Prof. Maurizio Righetti, Fabio Sartori and technicians at the hydraulic laboratory of University of Trento for their support during my experiments.

I was lucky to meet Prof. David Lyzenga from University of Michigan at the IGARSS 2015 conference. As pioneer scientist in the field, I was able to learn much from his deep insights about the physics of aquatic remote sensing and coauthored a paper with him. The same conference allowed me to later work with Prof. Nima Pahlevan from NASA Goddard Space Flight Center who supported my research with radiative transfer modeling and constructive comments as coauthor of another paper.

At last but certainly not least, my greatest and hearty thanks to my lovely parents, brother and his wife who made my research and life more enjoyable.

Milad Niroumand-Jadidi, November 2017

List of Publications

1- **Niroumand-Jadidi, M.** and Vitti, A., 2017. Reconstruction of River Boundaries at Sub-pixel Resolution: Estimation and Spatial Allocation of Water Fractions, *ISPRS International Journal of Geo-Information. 6(12):383.*

2- **Niroumand-Jadidi, M.**, Vitti, A. and Lyzenga, D., Multiple Optimal Depth Predictors Analysis (MODPA) for River Bathymetry: Findings from Spectroradiometry, Simulations and Satellite Imagery, *Remote Sensing* (submitted)

3- **Niroumand-Jadidi, M.**, Pahlevan, N. and Vitti, A., Bottom Reflectance Retrieval in Shallow Rivers: Findings from Spectroscopy, Radiative Transfer Modeling and Satellite Imagery, *Remote Sensing of Environment* (submitted)

4- **Niroumand-Jadidi, M.** and Vitti, A., 2017. Grain Size Mapping in Shallow Rivers Using Spectral Information: A Lab Spectroradiometry Perspective, Proc. SPIE 10422, *Remote Sensing of the Ocean, Sea Ice, Coastal Waters, and Large Water Regions 2017*, 104220B. doi: 10.1117/12.2278646

5- **Niroumand-Jadidi, M.** and Vitti, A., 2016. Improving the Accuracies of Bathymetric Models Based on Multiple Regression for Calibration (Case Study: Sarca River, Italy), Proc. SPIE 9999, *Remote Sensing of the Ocean, Sea Ice, Coastal Waters, and Large Water Regions 2016*, 99990Q, doi: 10.1117/12.2242083.

6- **Niroumand-Jadidi, M.** and Vitti, A., 2016. Optimal Band Ratio Analysis of WorldView-3 Imagery for Bathymetry of Shallow Rivers (case Study: Sarca River, Italy), *ISPRS- International Archives of the Photogrammetry, Remote Sensing and Spatial Information Sciences*, Volume XLI-B8, 2016, pp. 361-364. doi:10.5194/isprsarchives-XLI-B8-361-2016.

7- **Niroumand-Jadidi, M.** and Vitti, A., 2015. Sub-Pixel Mapping of Water Boundaries Using Pixel Swapping Algorithm (Case Study: Tagliamento River, Italy), Proc. SPIE 9638, *Remote Sensing of the Ocean, Sea Ice, Coastal Waters, and Large Water Regions 2015*, 96380G; doi:10.1117/12.2194579.

List of Achievements

1- **Best Paper and Oral Presentation Award**, 2017, SPIE Remote Sensing Conference, Warsaw, Poland.

2- **Invited Talk**, 2017, SPIE Remote Sensing Conference, Warsaw, Poland.

3- **Best Paper and Oral Presentation Award**, 2016, SPIE Remote Sensing Conference, Edinburgh, UK.

4- **SPIE Scholarship for Potential Long-range Contributions to the Field of Optics and Photonics**, 2016, awarded by SPIE (International Society for Optics and Photonics).

5- **Alexander Goetz Instrument Support Award**, 2016, short-term usage of a field spectroradiometer fully supported by ASD Inc.

6- **Best Paper and Oral Presentation Award**, 2015, SPIE Remote Sensing Conference, Toulouse, France.

7- **Imagery Grant**, 2015 and 2017, awarded by DigitalGlobe Foundation.

Abstract

Remote sensing techniques could enable remarkable advances in characterizing rivers hydromorphology by providing spatially and temporally explicit information. Remote mapping of hydromorphology can play a decisive role in a wide range of river science and management applications including habitat modeling and river restoration. High resolution satellite imagery (HRSI) has recently emerged as potentially powerful means of mapping riverine environments. This research aims to develop advanced methodologies for processing HRSI to map and quantify a set of key hydromorphological attributes including: (1) river boundaries, (2) bathymetry and (3) riverbed types and compositions.

Boundary pixels of rivers are subject to spectral mixture that limits the accuracy of river areas extraction using conventional hard classifiers. To address this problem, unmixing and super resolution mapping (SRM) are focused as two steps, respectively, for estimation and then spatial allocation of water fractions within the mixed pixels. Optimal band analysis for NDWI (OBA-NDWI) is proposed to identify the pair of bands for which the NDWI values yield the highest correlation with water fractions. The OBA-NDWI then incorporates the optimal NDWI as a predictor of water fractions through a regression model. Water fractions obtained from the OBA-NDWI method are benchmarked against the results of simplex projection unmixing (SPU) algorithm. The pixel swapping (PS) and interpolation-based algorithms are applied on water fractions for SRM. In addition, a simple modified binary PS (MBPS) algorithm is proposed to reduce the computational time of the original PS method. Water fractions obtained from the proposed OBA-NDWI method are demonstrated to be in good agreement with those of SPU algorithm (R^2=90%, RMSE=7% for WorldView-2 (WV-2) image and R^2=87%, RMSE=9% for Geoeye image). The spectral bands of WV-2 provide a wealth of choices through the proposed OBA-NDWI to estimate water fractions. The interpolation-based and MBPS methods lead to sub-pixel maps comparable with those obtained using the PS algorithm, while they are computationally more effective. SRM algorithms improve user/producer accuracies of river areas about 10% with respect to conventional hard classification.

This research introduces multiple optimal depth predictors analysis (MODPA) that combines previously developed depth predictors along with other measures such as the intensity components of HSI color space. To avoid over-fitting of the linear model, statistically optimal predictors are selected based on one of partial least square (PLS), stepwise and principal component (PC) regressions. The primary focus of this study is on shallow and clearly flowing streams where

substrate variability could have pronounced effect on depth retrievals. Spectroscopic experiments are performed in controlled condition of a hydraulic laboratory to examine the robustness of bathymetry models with respect to changes in bottom types. Further, simulations from radiative transfer modeling are used to extend the analysis by isolating the effect of inherent optical properties (IOPs) and also by investigating the performance of bathymetry models in optically complex and also deeper streams. Bathymetry of Sarca, a shallow river in Italian Alps, is also mapped using a WorldView-2 (WV-2) image where the atmospheric compensation (AComp) product is evaluated for the first time. Results indicate the robustness of multiple-predictor models particularly MODPA rather than single-predictor models such as optimal band ratio analysis (OBRA) with respect to heterogeneity of bottom types, IOPs and atmospheric effects. This study suggests extra predictors when the multiple regression is assisted with an optimal predictors selection process (e.g. MODPA). The extra predictors enhance the accuracy of depth retrievals particularly in optically complex waters and also for low spectral resolution imagery (e.g. GeoEye). Further, enhanced spectral resolution of WV-2 compared to GeoEye improves the bathymetry retrievals. MODPA based on PLS regression provided improvements on the order of 0.05 R^2 and 0.7 cm RMSE compared to multiple Lyzenga and 0.18 R^2 and 2 cm RMSE compared to OBRA using AComp reflectances of WV-2 for Sarca River with a maximum 0.8 m depth. In addition, a theoretical approach namely hydraulically assisted bathymetry (HAB) is assessed and further modified for calibration of bathymetry models that provided comparable results with the empirical calibration approach.

Substrate mapping in fluvial systems has not received as much attention as that in nearshore optically shallow waters of inland and coastal areas. The research to date has been primarily based on surface spectral reflectance data without accounting for water column attenuations. This study aims at retrieving the bottom reflectances in shallow rivers and then examining the effectiveness of inferred bottom spectra in mapping of substrate types. Bathymetry and diffuse attenuation coefficient (k_d) are derived from above-water reflectances for which some in-situ/known depths are required. Following the retrievals of depth and k_d, bottom reflectances are estimated based on a water column correction method. Moreover, the efficacy of vegetation indices (VIs) is examined for making distinction among the densities of submerged aquatic vegetation (SAV) using either above-water or retrievals of bottom reflectances. This research benefits, for the first time, from three different approaches including controlled spectroscopic measurements in a hydraulic lab, simulations from radiative transfer modeling and an 8-band WordView-3 (WV-3) image. The results indicate the significant enhancements of streambed mapping using inferred bottom reflectances than using above-water spectra. This is evident, for instance, on clustering of three bottom types using simulated spectra with 20% enhancement of overall accuracy. Deep-water

correction demonstrated to have most of an impact on retrievals of bottom reflectances only in NIR bands when the water column is relatively thick (> 0.5 m) and/or when the water is turbid. The red-edge (RE) band of WV-3/WV-2 improves remarkably the detection of SAV densities based on the VIs either using above-water or retrieved bottom spectra. Further, the simulated spectra suggest that enhanced spectral resolution of 8-band WV-3 leads to improvements in streambed mapping compared to traditional 4-band imagery. This study demonstrated the feasibility of retrieving bottom reflectances and mapping SAV densities from space in a shallow river using the WV-3 image (user and producer accuracies of 67% and 60% in average for three levels of SAV densities). Moreover, the feasibility of mapping grain size classes is assessed using spectral information based on laboratory experiments coupled with simulations. The changes in grain sizes affect the magnitude of reflectances while the shape of spectra remains almost identical. This characteristic feature demonstrated high potentials for mapping grain size classes by retrieving the bottom reflectances.

In summary, HRSI provided promising results and effective means of mapping the selected hydromorphological attributes of shallow rivers in spatially continuous and in large extents.

Dedicated to my parents,

Table of Contents

List of Figures

List of Tables

Chapter 1: Introduction

1.1 Rivers Hydromorphology

Fluvial geomorphology, hydraulics and hydrology are closely linked to each other so that their relevant attributes are frequently described together as “hydromorphology” (Orr et al., 2008, Vaughan et al., 2009; Belletti et al., 2014; Woodget, 2015; Rinaldi et al., 2017). The key attributes describing the hydromorphology of rivers encompass dimensions and shape of the channel, continuity and connectivity of the stream, inclination or slope angle of the channel, bed topography, substrate type and size, water depth and flow velocity. The description of a river system can be enhanced by means of knowledge about hydrological and geomorphological processes (e.g. sediment transport), and the spatiotemporal arrangement of the hydromorphological units (Poff et al., 1997; Maddock, 1999; Gilvear et al., 2004; Vaughan et al., 2009).

Mapping and monitoring of rivers hydromorphological features are of particular importance in river restoration (Sundermann et al., 2011; Poppe et al., 2016; Piégay et al., 2016; Marteau et al., 2017), characterizing aquatic habitats (Parasiewicz, 2007; Conallin et al., 2010; Bergeron and Carbonneau, 2012; Demarchi et al., 2016; Belletti et al., 2017), making linkages between physical and biological conditions of riverine environments for understanding biodiversity and ecosystem functioning (Poole, 2010; Elosegi et al., 2010; Belletti et al., 2017), hazard identifications and management applications (Legleiter et al., 2002; Neal et al., 2009; Bizzi et al., 2016; Rinaldi et al., 2017). More specifically, assessment of hydromorphological conditions of river systems could be considered as the backbone of common habitat simulation models such as MesoHABSIM

(Parasiewicz, 2001). In this regard, there is a very close correspondence between hydromorphological units and meso-habitats so that they are usually used as synonyms (Parasiewicz, 2001; Maddock and Bird, 1996).

The hydromorphology and ecology of fluvial systems interact through complex processes that opens up interdisciplinary researches for managing and conservation of rivers and enhancement of ecosystem services (Vaughan et al. 2009; Meitzen et al., 2013; Rinaldi et al., 2017). These interactions have recently received many attentions so that an "ecohydromorphology" field has been suggested for further developments in river sciences (Clarke et al., 2003; Vaughan et al. 2009; Meitzen et al., 2013). A schematic overview of interactions among geomorphology, hydrology and ecology of riverine systems is illustrated in Figure 1.1.

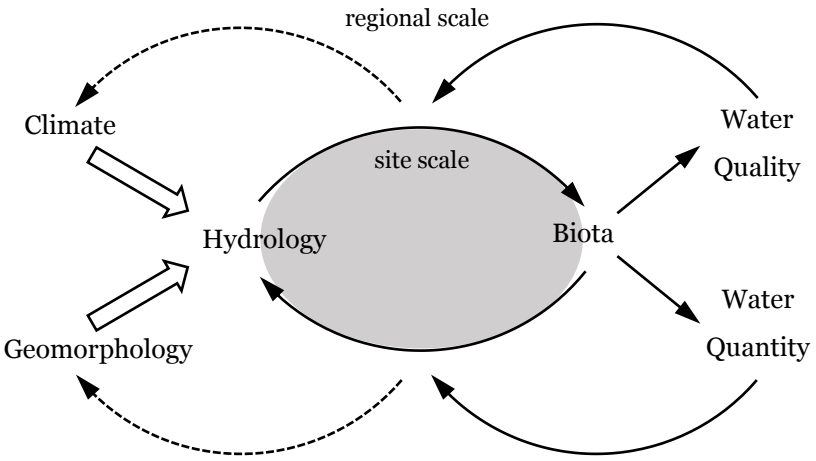

Figure 1.1 The structure of direct and indirect interactions among hydrology, geomorphology and ecology at different scales (Trepel and Kluge, 2002).

Hydromorphological attributes of rivers are traditionally being mapped based on field surveys (Vezza et al., 2014; Belletti et al., 2017). Field measurements are based on series of survey forms and can be supported by topographic instruments (e.g. total stations, GPS devices) and mobile mapping tools (e.g. ArcPAD, QGIS Mobile) to record spatial features of hydromorphological attributes along with parameters such as flow depth and velocity and substrate type (Parasiewicz, 2007; Vezza et al., 2014; Belletti et al., 2017). However, filed surveys are subject to fundamental shortcomings so that "*they do not meet the requirements of the increasingly recognized 'riverscape' paradigm* (Woodget, 2015)". In-situ observations are limited to small spatial extents

of accessible reaches and at discrete sampling locations (Moody and Troutman, 2002, Leckie et al., 2005; Carbonneau and Piégay, 2012; Marcus et al., 2012; Woodget, 2015). Further, the frequency of field-based measurements is not sufficient enough for understanding temporal variability of hydromorphological attributes (Poole et al., 1997; Leuven et al., 2002; Legleiter et al., 2002; Casado et al., 2015). In-situ measurements are time/cost consuming and rely on the expertise of the surveyor for the identification of hydromorphological features that hinders the objective reassessment of field records (Casado et al., 2015; Bizzi et al., 2016). In this regard, remote sensing provides alternative for mapping and characterization of riverine systems. In this work, original methodologies are presented to extract key hydromorphological attributes including river boundaries, bathymetry and riverbed properties for high resolution satellite imagery (HRSI).

1.2 Remote Sensing of Hydromorphology

Remote sensing techniques can be an alternative to traditional field-based measurements and also have the potential to enhance our understanding of fluvial systems by providing spatially and temporally explicit information (Marcus and Fonstad, 2008; Marcus and Fonstad, 2010; Legleiter and Overstreet, 2012; Shintani and Fonstad, 2017; Demarchi et al., 2017). Remote sensing and image processing techniques have long been interesting for a wide range of fluvial science and management applications (Winterbottom and Gilvear, 1997; Legleiter et al., 2002; Marcus et al, 2003; Leckie et al., 2005; Legleiter, 2013; Marcus and Fonstad, 2010; Hugue et al., 2016). With the advancement of aerial imagery, remotely mapping of rivers at large scales also has been emerged and developed. However, interpretation of airborne images in conjunction with field observations has been used generally for mapping of usually single or limited number of attributes (Lapointe and Carson, 1986; Gilvear et al., 1995; Gilvear et al., 1999; Leuven et al., 2002; Gilvear and Bryant, 2003; Bertoldi et al., 2011).

Remotely sensed data from either active or passive sensors has been used for characterization of different hydromorphological attributes. Synthetic aperture radar (SAR) is used for mapping flood extents and to extract some basic geometric features such as channel dimensions and

planforms as well as monitoring river morphology (Neal et al. 2009; Mitidieri et al., 2016). Light detection and ranging (LiDAR) data providing digital surface models (DSMs) can be used for inferring channel slope and dimensions (Biron et al. 2013). Optical imagery (multi/hyperspectral) are frequently used for mapping and monitoring of different hydromorphological attributes such as delineation of river area (Fisher et al. 2013; Niroumand-Jadidi and Vitti, 2015) and bathymetry (Winterbottom and Gilvear, 1997; Legleiter, 2013; Niroumand-Jadidi and Vitti, 2016b). Marcus et al. (2003) used airborne 128-band hyperspectral imagery with high spatial resolution (1 m) to map in-stream habitats, depths, and woody debris where they found good agreements with field observations. Piégay et al. (2009) used aerial photographs for spatiotemporal census investigation of braided rivers in the French Alps. Legleiter (2012) investigated the mapping of river channel form by fusion of LiDAR and optical imagery. Michez et al. (2013) characterized several attributes of riparian zones using aerial LiDAR data applied to Houille river (Belgium and France). Demarchi et al. (2016) delineated in-stream mesohabitats of Orco river (Italy) with very high accuracy based on an object-based classification and by fusing very high resolution (0.4 m) airborne imagery and LiDAR point clouds. Demarchi et al. (2017) produced a database of hydromorphological attributes for a large area of river floodplains using very high resolution (0.4 m) aerial imagery and low-resolution LiDAR data. There are several research concerned with grain size mapping using optical imagery that they are mostly based on texture analysis over exposed bed materials (Adams, 1979; Ibbeken and Schleyer, 1986; Butler et al., 2001; Carbonneau and Lane 2004; Arif et al., 2016). For instance, Carbonneau and Lane (2004) used airborne digital imagery for mapping grain sizes of exposed bed materials along river channel where they found that only very high resolution imagery (3 cm) allow automated grain size mapping based on analyzing the texture or local image semivariance.

The advancement of water-penetrating green LiDAR systems has recently opened up new possibilities for studying rivers hydromorphology (Kinzel et al., 2013; Legleiter et al., 2016). Using green/bathymetric LiDARs, it is possible to infer water depths and map submerged and surface elevations without using any field data for calibration (Legleiter et al., 2016). Kinzel et al. (2013) evaluated the potentials of green LiDAR for mapping the bathymetry of rivers. Mandlburger et al. (2015) developed techniques for modeling the water surface and depth using airborne

bathymetric LiDAR in order to map and monitor hydromorphological units in Pielach river (Austria). Pan et al. (2015) proposed a continuous wavelet based approach for processing high resolution airborne full waveform LiDAR for bathymetry of Snake, Blue and Colorado rivers (USA). Legleiter et al. (2016) compared the capabilities of hyperspectral imagery and bathymetric LiDAR for depth retrievals in a range of riverine environments with different optical properties of water column. They found that bathymetric LiDAR yield relatively low accuracies so that unable to detect very shallow depths (< 10 cm deep).

Remote sensing using unmanned aerial vehicles (UAVs) has received growing recent interest for characterizing rivers hydromorphology (Overstreet and Legleiter, 2017). Flynn and Chapra (2014) used an RGB digital camera mounted on a UAV for mapping green algae of Clark Fork river (USA) with shallow and clearly flowing water. Tamminga et al. (2015) used a small quadcopter UAV to map a set of hydromorphological attributes including bathymetry, grain sizes, undercut banks, forested channel margins, and large woods for suitability analysis of aquatic habitat in Elbow river (Canada). Visser et al. (2015) investigated the bathymetry mapping of Wylye and Frome rivers (UK) using spectral measurements from a UAV. Bathymetric LiDAR systems are also becoming available for UAVs with some applications for mapping rivers hydromorphology (Mandlburger et al. 2016).

Structure-from-motion photogrammetry (SfM) has been also recently emerged as an advancing tool for studying fluvial hydromorphology (Fonstad et al. 2013; Marteau et al., 2017). SfM is capable of generating three dimensional (3D) geometry of a scene using a series of overlapping 2D images (Woodget, 2015). Fonstad et al. (2013) demonstrated the applicability of SfM for producing digital elevation models (DEMs) of riverine environments from low-altitude platforms. Javernick et al. (2014) performed a comprehensive analysis on terrain models achieved from SfM techniques in braided Ahuriri river (New Zealand). Woodget (2015) demonstrated the potentials of SfM techniques applied to imagery acquired by a UAV for mapping key in-stream habitat indicators including topography and flow depth, substrate size and surface flow types. More recently, the application of SfM photogrammetry has been explored for mapping and evaluation of the geomorphic changes associated with river restoration actions based on UAV observations (Marteau et al., 2017).

The increased number of satellite missions together with the enhancements in spatial and spectral resolutions can also provide remarkable benefits for fluvial studies (Legleiter and Overstreet, 2012; Hugue et al., 2016; Niroumand-Jadidi and Vitti, 2016a). More specifically, advances in simultaneous acquisition of both high spatial and spectral resolutions from spaceborne sensors can lead potentially to interesting applications for fluvial studies applicable even for small rivers (Legleiter and Overstreet, 2012; Hugue et al., 2016; Niroumand-Jadidi and Vitti, 2016b). For instance, WorldView-2 (WV-2) provides 1.85 m spatial resolution with 8 multispectral bands (see Table 1.1) that recently have been used for river bathymetry (Legleiter and Overstreet, 2012; Niroumand-Jadidi and Vitti, 2016a; Niroumand-Jadidi and Vitti, 2016b).

On the other hand, the recently launched twin satellites of Sentinel-2A and Sentinel-2B provide medium resolution images (10-60 m) with high spectral and temporal resolution which are freely available for public. Applications of Sentinel-2 data in fluvial hydromorphology have been emerged in a few recent researches such as for grain size mapping (Marchetti, 2017).

Marcus and Fonstad (2010) announced the emergence of a major sub-discipline in river sciences termed “Fluvial Remote Sensing” due to the growing integration of remote sensing and fluvial studies. Considering the more recent advances in fluvial remote sensing according to the abovementioned elements, the remote sensing of fluvial systems is now in a revolutionary era. These key elements are summarized in Figure 1.2.

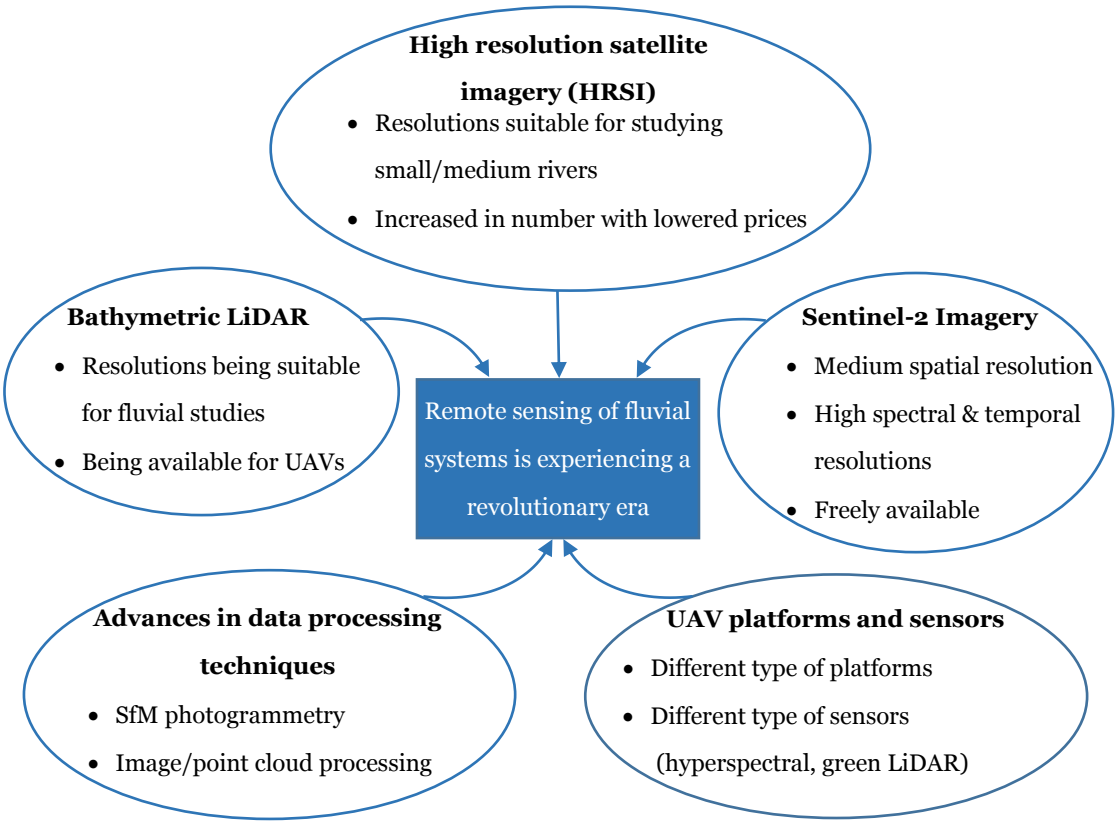

Figure 1.2 The recent key advances revolutionizing the remote sensing of fluvial systems.

Although airborne and UAV-based sensors can provide high-resolution data, either spatially or spectrally, they are limited in terms of spatial coverage, temporal resolution and accessibility to remote areas. In contrast, spaceborne sensors provide global spatial coverage with high temporal resolution that can facilitate long-term and large-scale studies of rivers. Whited et al., (2011) used imagery from Landsat and Quickbird satellites for analyzing some geometric features of Pacific Rim rivers (e.g. channel length, sinuosity, number and density of nodes) as well as the percentage of wetted and vegetated areas. An object-based classification approach has been applied on Landsat and Aster imagery for mapping of some hydromorphological attributes including whitewater (an indicator for water turbulence in order to identify rapids, pools, etc.), islands and bank cover as well as qualitative depth classes in Congo River (Ridgeway, 2006).

With the recent enhancements in spatial resolution of the satellite sensors, new opportunities have emerged for fluvial applications and in particular for studying small/medium rivers (Legleiter and Overstreet, 2012; Hugue et al., 2016). Legleiter and Overstreet (2012) performed a feasibility analysis on mapping river bathymetry from space and using WV-2 imagery. Hugue et

al., (2016) used WV-2 image to map structural patterns in hydraulic habitat availability of the Kiamika River (Canada) by inferring the water depths based on empirical ratio models and then cross-sectional estimations of flow velocity assuming a known discharge.

1.2.1 High Resolution Satellite Imagery (HRSI)

This section summarizes specifications of the main high resolution satellites including WV-2 and GeoEye which are used in this study. There have been dramatic enhancements in the highest spatial resolution achieved from satellites since the launch of first earth observation satellite in 1972 (Figure 1.3).

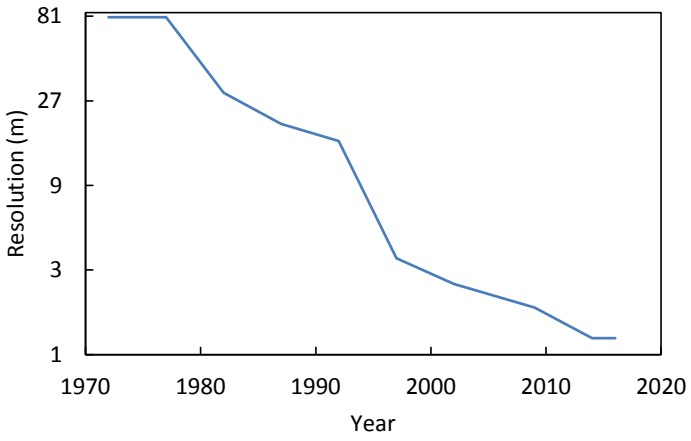

Figure 1.3 Time evolution of the highest resolution multispectral sensors onboard land imaging civilian satellites adapted from (Belward and Skøien, 2015). Note that the resolutions are shown with a logarithmic scale.

With the launch of first high resolution satellite (IKONOS) in 1999, new opportunities opened up for studying land/water surfaces at high spatial resolution. A decade later, a new generation of HRSI became available with the launch of WV-2 satellite. WV-2 is the first satellite which provides a unique combination of high spatial and spectral resolutions (DigitalGlobe, 2009). The previous multispectral high resolution sensors (e.g. IKONOS, QuickBird, Geoeye) record the spectral responses of land/water surfaces in three visible bands (RGB) and one near-infrared (NIR) band. This is while, WV-2 provides 8 spectral bands ranging from visible (400 nm) to NIR (1040 nm) at a spatial resolution of 1.84 m (Table 1.1). In addition to the traditional RGB-NIR bands, four new spectral bands have been added which include coastal blue (400-450 nm), yellow

(585-625 nm), red-edge (705-745 nm) and NIR-2 (860-1040 nm). The main specifications of high spatial resolution satellites are listed in Table 1.1. Note that this table includes only satellites launched by DigitalGlobe Company which are the main and widely used sensors for remote sensing applications at high resolution. The WV-3 satellite launched in 2014 is the first super-spectral sensor that provides 8 additional bands in shortwave infrared (SWIR). The very recent satellite of DigitalGlobe namely WV-4 provides RGB-NIR bands as continuity of the previous 4-band missions.

Table 1.1 High resolution satellites launched by DigitalGlobe (2017) and their specifications. Pan and MS denote panchromatic and multispectral, respectively.

Satellite	**Launch year**	**Swath width**	**Spatial resolution**	**Spectral resolution**	**Dynamic range**	**Average revisit at 40°N latitude**
IKONOS	1999	11.3 km	Pan: 0.82 m MS: 3.2 m	1 Pan Band 526 – 929 nm 4 MS Bands Blue: 445 – 516 nm Green: 506 – 595 nm Red: 632 – 698 nm NIR: 757 – 853 nm	11 bits	~ 3 days
Quickbird	2001	14.9 km	Pan: 0.55 m MS: 2.16 m	1 Pan Band 405 - 1053 nm 4 MS Bands Blue: 430 - 545 nm Green: 466 - 620 nm Red: 590 - 710 nm NIR: 715 - 918 nm	11 bits	2-12 days
WorldView-1	2007	17.7 km	Pan: 0.5 m	1 Pan Band 397 – 905 nm	11 bits	1.7 days
GeoEye	2008	15.3 km	Pan: 0.41 m MS: 1.64 m	1 Pan Band 450–800 nm 4 MS Bands Blue: 450 - 510 nm Green: 510 - 580 nm Red: 655 - 690 nm NIR: 780 - 920 nm	11 bits	< 3 days
WorldView-2	2009	16.4 km	Pan: 0.46 m MS: 1.85 m	1 Pan Band 450–800 nm 8 MS Bands Coastal: 400 - 450 nm	11 bits	1.1days

				Blue: 450 - 510 nm Green: 510 - 580 nm Yellow: 585 - 625 nm Red: 630 -690 nm Red Edge: 705 - 745 nm NIR-1: 770 - 895 nm NIR-2: 860 - 1040 nm		
WorldView-3	2014	13.2 km	Pan: 0.31 m MS: 1.24 m SWIR: 3.7 m CAVIS: 30 m	1 Pan Band 450–800 nm 8 MS Bands Coastal: 397–454 nm Blue: 445–517 nm Green: 507–586 nm Yellow: 580–629 nm 8 Red: 626–696 nm Red Edge: 698–749 nm NIR-1: 765–899 nm NIR-2: 857–1039 nm 8 SWIR Bands SWIR-1: 1184–1235 nm SWIR-2: 1546–1598 nm SWIR-3: 1636–1686 nm SWIR-4: 1702–1759 nm SWIR-5: 2137–2191 nm SWIR-6: 2174–2232 nm SWIR-7: 2228–2292 nm SWIR-8: 2285–2373 nm 12 CAVIS Bands Desert Clouds: 405-420 nm Aerosol-1: 459- 509 nm Green: 525- 585 nm Aerosol-2: 635- 685 nm Water-1: 845- 885 nm Water-2: 897- 927 nm Water-3: 930- 965 nm Cirrus: 1365 - 1405 nm Snow: 1620 - 1680 nm Aerosol-1: 2105 - 2245 nm Aerosol-2: 2105 - 2245 nm	Pan & MS: 11 bits SWIR: 14 bits	1 day
WorldView-4	2016	13.1 km	Pan: 0.31 m MS: 1.24 m	1 Pan Band 450–800 nm 4 MS Bands Blue: 450 - 510 nm Green: 510 - 580 nm Red: 655 - 690 nm NIR: 780 - 920 nm	11 bits	1 day

This research benefits from 8-band WV-2 imagery for extractions of hydromorphological attributes. In addition, GeoEye images are also used to get more insights into the effectiveness of WV-2's additional bands compared to traditional 4-band HRSI.

1.2.2 Optical Remote Sensing of Rivers

This section provides an overview about principles of optical remote sensing over water bodies and in particular rivers. Specific theoretical background and state of the art concerned with each objective of the research are discussed in details at the beginning of corresponding chapters.

Passive optical remote sensing has a sound background in coastal research for instance for bathymetry, mapping seagrass and coral reef as well as retrieval of water quality indicators (Lyzenga, 1978, Lyzenga, 1981; Philpot, 1988; Louchard et al., 2003; Lesser and Mobley, 2007; Pahlevan et al., 2017a). The remote sensing techniques for studying inland waters and fluvial systems are mainly adapted from the traditional ocean color methods (Legleiter et al., 2004; Legleiter et al., 2016b; Niroumand-Jadidi and Vitti, 2016a; Overstreet and Legleiter, 2017). In this regard, Legleiter et al. (2004) carried out for the first time a comprehensive study on the physical concept of remotely mapping of shallow streams in order to gain insights into potentials of optical imagery for studying rivers hydromorphology and in particular bathymetry. In this way, they have investigated the radiative transfer model and the interaction of light with different environments (i.e. atmosphere, water surface, water column and stream bed) through its traveling pass from sun to reflecting back to the sensor.

In summary, total at-sensor radiance over water bodies (L_T), encompass four different components of radiances upwelling from water body's bed (L_b), water column (L_c), water surface (L_S), and the atmosphere (L_p). Each component depends on the wavelength (λ) which can be associated to a spectral band. The radiance components are summarized in Equation 1.1 and shown in Figure 1.4.

$$L_T(\lambda) = L_b(\lambda) + L_c(\lambda) + L_S(\lambda) + L_p(\lambda) \quad (1.1)$$

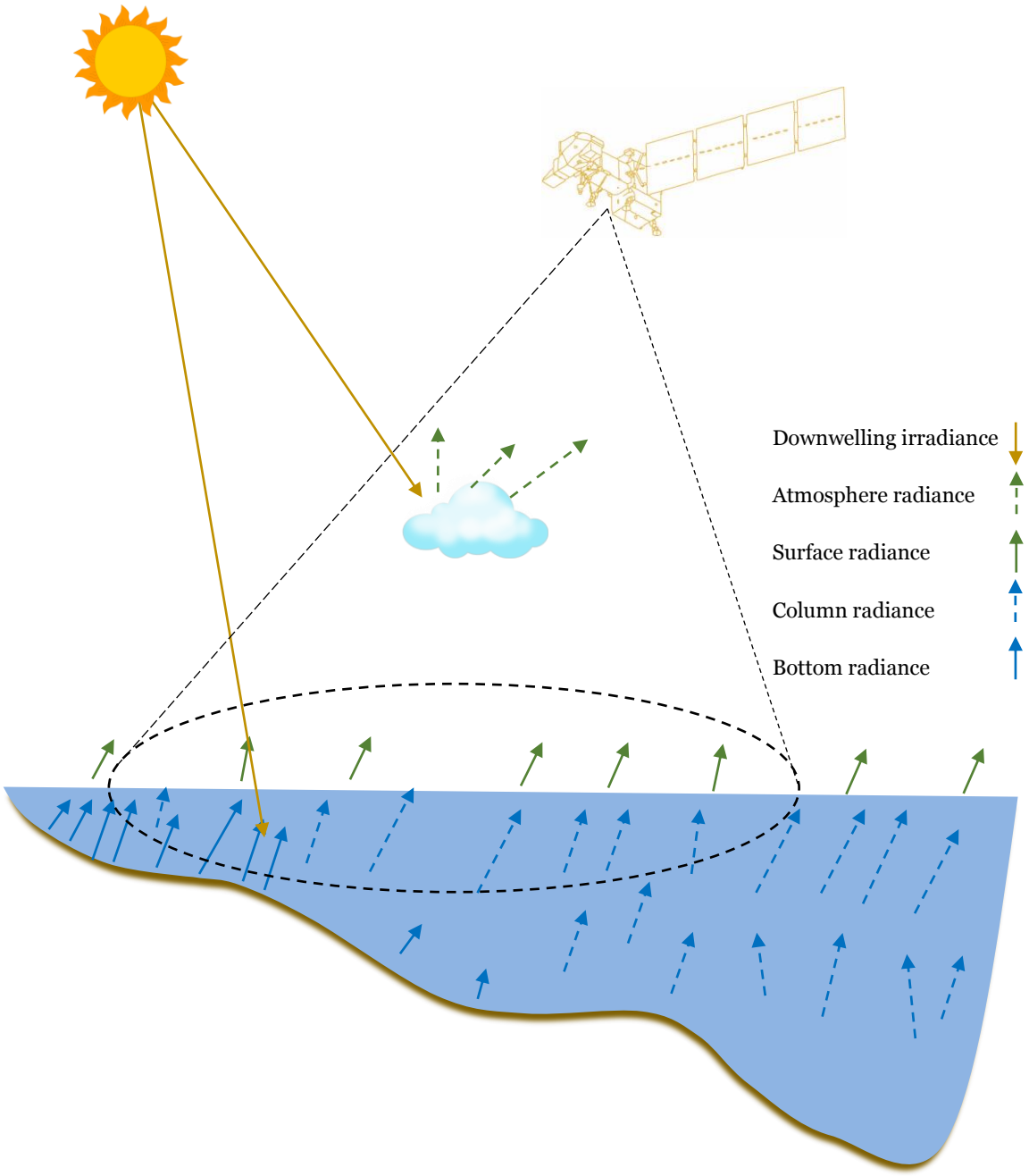

Figure 1.4 Four components involved in the total at-sensor radiance through passive remote sensing of shallow to deep waters.

According to a basic physical concept recognized as Beer-Lambert law, attenuation of the light through traveling water column can be described as an exponential model (Equation 1.2) which is central for characterizing the effect of water column on total-at-sensor radiance and consequently retrieval of key parameters such as water depths and bottom reflectances.

$$I = I_0 e^{-kd} \tag{1.2}$$

where I_o is the intensity of incident light, e is the Euler number. k stands for the attenuation coefficient (a constant indicating the strength of absorption per unit depth) and I is the intensity of light in a given water depth of d (Denny, 2003).

Considering the Beer-Lambert's law and expanding the Equation 1.1 reveal the main parameters involved in passive remote sensing of river bodies:

$$L_T = E_d\, CT(R_b - R_c)\exp(-kd) + E_d CTR_c + T\rho L_k + L_P \tag{1.3}$$

where E_d is the downwelling solar irradiance. R_b and R_c denote the bottom and volume reflectance of water body, respectively. C and T stand for transmission across air–water interface and atmosphere transmittance, respectively. The reflectance of the air–water interface is denoted by ρ. Diffuse sky radiance and path radiance from the atmosphere are denoted by L_k and L_p, respectively.

Aside L_p, each of the above-mentioned radiance components can be associated to a specific property of the water body. For instance, surface component of the radiance can be linked to the roughness of the water surface which in turn is a function of local hydraulics in riverine environments and can potentially reveal information about the flow velocity (Overstreet and Legleiter, 2017). The bathymetry information is embedded in the bottom component of radiance which is affected not only by water depth but also by the bottom type (Lee et al., 1998; Stumpf et al., 2003; Legleiter et al., 2009). Thus, in order to retrieve the water depth, it is essential to remove or reduce the following effects from total at-sensor radiance: (a) radiance components upwelling from water column, water surface and the atmosphere, and (b) substrate variability (Legleiter et al., 2004; Legleiter et al., 2009). As evident in Figure 1.4, bottom reflected radiance is the dominant component of total at-sensor radiance with respect to the signal upwelling from water body in shallow waters and it would be negligible over deep waters (Legleiter et al., 2004; Legleiter et al., 2009; Niroumand-Jadidi and Vitti, 2016a). This would be beneficiary for bathymetry retrieval in shallow rivers due to having a strong signal from bottom. However, the substrate variability can complicate depth retrievals.

In summary, it is essential to isolate the radiance component of interest or to reduce the effect of other undesirable components to retrieve a parameter of interest. The radiance components and their affecting parameters are listed in Table 1.2. For instance, the component of radiance associated with the water column is affected by the inherent optical properties (IOPs) of the water column including total suspended sediment (TSS), chlorophyll-a (Chl-a) and colored dissolved organic matter (CDOM).

Table 1.2 The radiance components of total at-sensor radiance observed over river bodies and their influencing parameters, adapted from (Legleiter et al., 2004 and Legleiter et al., 2009).

Radiance component	Influencing parameters
Stream bed	water depth, substrate type
Water column	TSS, Chl-a, CDOM
Water surface	surface roughness and viewing geometry
Atmosphere	water vapor, aerosols, etc.

In this work, a set of spectra is simulated using Hydrolight radiative transfer modeling (Mobley and Sundman, 2008) in order to understand the spectral responses of shallow waters with respect to some of abovementioned parameters including water depth, bottom type, TSS and CDOM. Figure 1.5 shows the remote sensing reflectances (Rrs) defined as ratio of water-leaving radiance to the total downwelling irradiance just above water (Mobley, 1994). The spectra are convolved to match the spectral bands of WV-2 sensor which is the satellite of interest in this research. As shown in Figure 1.5a, the long wavelengths (NIR) are very sensitive to the changes in water depths in very shallow waters. This is unlike the relatively deep waters in coastal environments where NIR bands become saturated due to the strong absorption by pure water in this spectrum. The substrate type also affects the spectra, which are illustrated for three different materials in a constant water depth and IOPs (Figure 1.5b). The impacts of changes in TSS and CDOM are also illustrated in Figures 1.5c and 1.5d, respectively. As evident, the increased TSS make the water appear brighter which is due to increased volume scattering within the water column (Legleiter et al., 2009). The increase in CDOM increases the absorption of light in short wavelengths (Mobley, 1994).

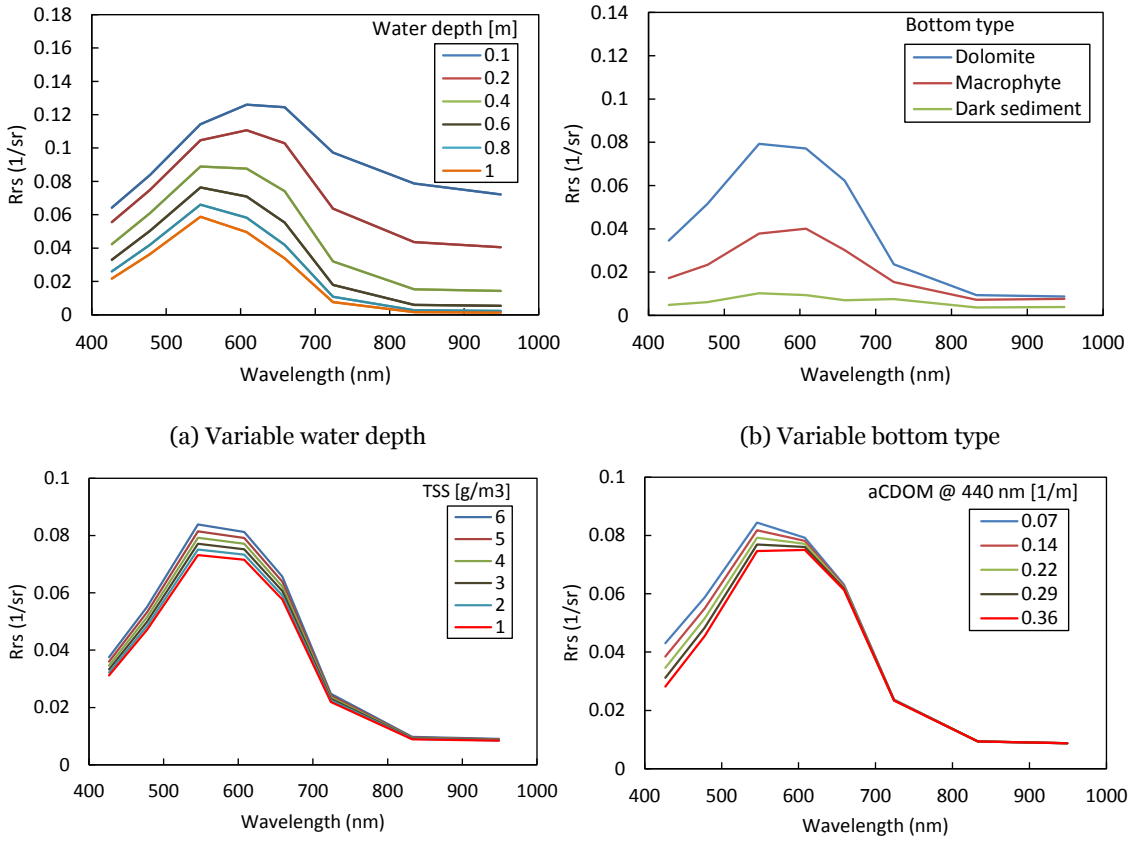

(a) Variable water depth

(b) Variable bottom type

(c) Variable TSS

(d) Variable CDOM

Figure 1.5 Rrs of shallow waters in a range of (a) water depths, (b) bottom types, (c) CDOM and (d) TSS. The values of CDOM are expressed by the absorption coefficient (aCDOM) at the 440 nm. The fixed parameters where applicable are as follows: dolomite bottom type, 0.5 m water depth, TSS=3 g/m^3, Chl-a= 2 mg/m^3 and aCDOM= 0.14 1/m.

These illustrations from radiative transfer modeling show some simple examples about the spectral signature of shallow waters associated with riverine environments in a range of parameters. In this work also spectroradiometric experiments are conducted along with simulations to develop and assess the methods in line with the research objectives.

1.3 Research Objectives

This research aims to develop advanced methods for analyzing HRSI to map and quantify three fundamental hydromorphological aspects of riverine environments including: (a) river boundaries, (b) bathymetry and (c) riverbed types and compositions. Comprehensive assessments

are conducted to elaborate the capabilities of 8-band WV-2 and 4-band GeoEye imagery for extraction of aforementioned hydromorphological elements. The research gaps followed by the objectives of this study are presented in the following for each of three topics.

- **Delineation of river boundaries**

The extraction of river boundaries is an essential aspect of characterizing the hydromorphology of a river (Güneralp et al., 2014; Demarchi et al., 2017). The common methods for delineation of river areas from optical imagery rely on hard classification approaches where each pixel can be assigned to a single land cover class such as water or non-water classes (Mather, 2004; Foody, 2006). This approach is subject to uncertainty when dealing with the mixed pixels that the presence of which is remarkably pronounced at river boundaries. The pixels forming the river boundaries are mostly mixed with the riparian zone so that hard labeling of pixels lead to uncertainties by neglecting decomposition of the spectral mixture. This can affect the estimation of wetted area, construction of cross-sections and consequently the accuracies of estimating hydraulic parameters such as discharge and cross-sectional velocity (Jiang et al., 2014; Wang et al., 2015b; Horkaew and Puttinaovarat, 2017). To tackle this problem, this research aims at reconstruction of river boundaries at sub-pixel resolution considering the spectral mixture issue. In this regard, two key steps are followed: (a) estimation of water fractions (i.e. unmixing) and then (b) spatial allocation of the fractions (i.e. super resolution mapping, SRM) within the mixed pixels. The following specific objectives are followed accordingly:

- developing a new method based on normalized difference water index (NDWI) to estimate water fractions and assessing the method's performance with respect to an advanced existing unmixing algorithm;
- spatial allocation of water fractions based on known SRM methods (e.g. pixel swapping) and enhancement of the methods to speed-up the mapping processes;
- assessing the impact of unmixing process on the final sub-pixel map by applying the SRM methods to semi-simulated fractions;
- assessing the accuracies of river boundaries extracted at sub-pixel resolution and comparing them to the conventional hard classification methods;

- assessing the potentials and drawbacks of conventional threshold-based methods for hard classification of water bodies;
- assessing the effectiveness of additional bands of WV-2 for extraction of river boundaries compared to the GeoEye imagery.

▪ **River bathymetry**

Bathymetry of rivers is still little explored from space and the techniques are being recently translated from conventional methods of ocean color remote sensing. Lyzenga's model (Lyzenga, 1978; Lyzenga, 1981) and optimal band ratio analysis (OBRA) developed by Legleiter et al. (2009) are the main empirical techniques to retrieve bathymetry from optical imagery. The existing models assume a linear relation between image-derived predictor/s and water depths either using single bands or band ratios. However, these methods are built solely upon single/multiple Lyzenga predictor/s or a single ratio predictor through a linear regression model. In this research, existing depth predictors and also some extra predictors are combined to take advantage from multiple informative predictors. Statistically significant predictors are then selected as optimal predictors for mapping the bathymetry. Further, a thorough analysis is conducted on the performance of proposed method compared to the existing methods with respect to several parameters affecting the optical properties of river bodies. The main objectives are listed as follows:

- developing a new method for bathymetry retrieval based on combining existing predictors and also defining extra predictors from color space transformation;
- selection of the optimal predictors based on partial least squares (PLS), stepwise and principal component (PC) regressions;
- assessing the performance of proposed bathymetry method compared to other techniques with respect to factors complicating the optical properties of river body including: variations in bottom types and IOPs (Chl-a, TSS and CDOM) and also atmospheric effects;
- assessing and modification of a theoretical approach for calibration of bathymetry

models;

- taking the advantage from spectroradiometric experiments and radiative transfer modeling to assess the performance of models with controlled parameters;
- assessing the potentials of WV-2's additional bands for river bathymetry.

▪ **Riverbed mapping**

Mapping of riverbed types and compositions is a very recent application of remote sensing to fluvial systems (Legleiter et al., 2016b). However, most of the existing research attempted to map the bottom properties in very shallow rivers without considering the attenuation effects of the water column. This research aims to adapt the techniques from ocean color remote sensing in order to estimate the diffuse attenuation coefficient (k_d) and then to retrieve the bottom reflectances. The effectiveness of retrieved bottom reflectances is assessed for riverbed mapping and in particular for classification of the submerged aquatic vegetation (SAV) densities. The following objectives are then perused:

- retrieving the k_d parameter using above-water spectra for some know water depths;
- assessing the accuracies of bottom reflectance retrievals in visible and NIR bands;
- assessing the effect of deep-water correction on bottom reflectance retrieval and streambed mapping;
- assessing the effectiveness of bottom reflectance retrievals compared to the above-water spectra for classification of the riverbed;
- assessing different vegetation indices for estimation of SAV densities using either retrieved bottom reflectances or above-water spectra;
- taking the advantage from spectroradiometric experiments and radiative transfer modeling to assess the performance of bottom reflectance retrieval with controlled parameters;
- evaluating the potentials of WV-2's additional bands for streambed mapping and in particular the effectiveness of red-edge band for detection of SAV densities.

1.4 Thesis Structure

The thesis is structured in five chapters which is illustrated in Figure 1.6. Chapters 2, 3 and 4 are associated with one of the hydromorphological elements considered in this study: delineation of river boundaries, bathymetry and riverbed mapping, respectively. Each of these chapters includes an introductive section presenting the state of the art and background information. As data and in particular spectroradiometric experiments and simulations are slightly different for each element, the dataset and experiments setup are then described for each chapter individually. Then the data analysis and results are presented in each chapter. Finally, Chapter 5 provides an overview and discussions about the key findings from each chapter along with making some suggestions for future works.

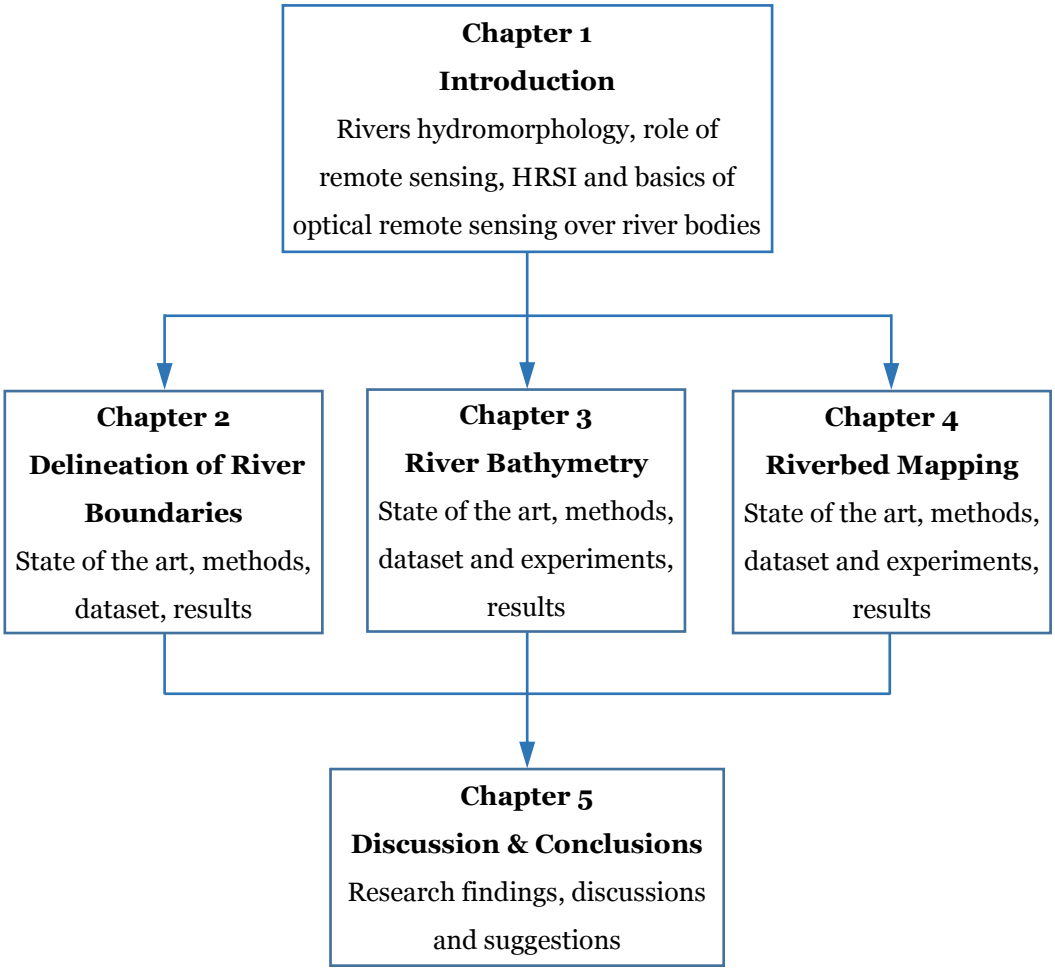

Figure 1.6 Thesis structure and main aspects of each chapter.

Chapter 2: Delineation of River Boundaries

2.1 Introduction

Extraction of river area is the primary task required for a wide range of remote sensing applications in fluvial systems spanning from hydrological, ecological, and morphological studies to mapping the habitat suitability for different aquatic species (Legleiter et al., 2004; Marcus and Fonstad, 2010; Hirpa et al., 2013; Feyisa et al., 2014; Güneralp et al., 2014). Thresholding on spectral bands (e.g. NIR band) or on water indices such as normalized difference water index (NDWI), as well as image classification (supervised or unsupervised) are the main techniques for delineation of water bodies from optical imagery (Jiang et al., 2014; Xie et al., 2016). However, most of the techniques consider a hard labeling approach for producing the water mask. This means that mixtures within the pixels are considered very roughly so that each pixel can be assigned to only a single water/non-water class which represents the most abundant class within the pixel. The spectral mixture can occur at every spatial resolution, particularly in the boundary pixels (Mather, 2004; Foody, 2006). This point deserves more attention in terms of remotely mapping of rivers, as the boundaries of river channels are inevitably subject to uncertainties concerned with mixture of water with surrounding land covers. Mixed boundary pixels can suppress the extraction of river area, geometric features, as well as construction of cross-sections. Accordingly, accurate mapping of river area and construction of boundaries can play a decisive role in studying rivers morphodynamics, ecological restoration, estimation of hydraulic parameters (e.g. discharge) and management of water resources (Jiang et al., 2014; Wang et al., 2015b; Horkaew and Puttinaovarat, 2017).

To address the problem of spectral mixture, a wide variety of unmixing and soft classification algorithms including physics-based and data driven techniques are developed (Keshavaand and Mustard, 2002; Bioucas-Dias et al., 2012; Heylen et al., 2014; Tran et al., 2014). These techniques estimate the fraction of each class within the pixels and is representing on a set of grayscale images. Although soft classifiers can reveal sub-pixel information, spatial distribution of fractions still remains unknown. To tackle this problem, super resolution mapping (SRM) techniques such as pixel swapping (Atkinson, 2005) are developed in order to spatially allocate the sub-pixels corresponding to fractions obtained from soft classification.

This research aims first at the estimation of water fractions within the mixed pixels (i.e. unmixing) and then at the spatial allocation of corresponding sub-pixels (i.e. SRM) in order to map river boundaries at the sub-pixel level. To this end, NDWIs are leveraged for the estimation of water fractions. As different combinations of spectral bands can be used in the structure of NDWI, a full search approach is proposed to identify the optimal pair of bands leading to the highest correlation of NDWI values with water fractions. The effectiveness of a regression model is explored for estimation of water fractions from NDWI values. The accuracy of the proposed method is compared against an advanced unmixing method, namely fully constrained simplex projection unmixing (SPU). A thorough investigation is carried out on the performance of SRM techniques in the context of river mapping. Several SRM techniques are focused including spatial optimization techniques such as pixel swapping (PS) as well as some interpolation-based algorithms. Furthermore, the PS algorithm is modified to speed up the binary water/non-water classification. Both semi-simulated and the fractions derived from real imagery are used for evaluation of SRM techniques. The first of these provides the possibility of accuracy assessment of the sole spatial allocation of sub-pixels task, while the latter considers also the uncertainties involved in estimation of water fractions. In addition, effectiveness of current thresholding methods on NDWIs is examined for hard water/non-water classification. Small rivers have been the interest of this study and, accordingly, HRSI including WorldView-2 (WV-2) and Geoeye imagery are used to exercise the implementations.

The remainder of this chapter is organized as follows: the following Section provides a brief overview about the sub-pixel reconstruction of river boundaries. Section 2.3 describes the

proposed methodology encompassing estimation of water fractions as well as SRM techniques. The case studies and the results of implementations are outlined in Sections 2.4 and 2.5, respectively.

2.2 Sub-pixel Reconstruction of River Boundaries

Labeling of each pixel purely as water or non-water has been a long-standing approach for masking out water features from the optical imagery. The techniques range from single-band thresholding (Jain et al., 2005) and water indices thresholding (McFeeters,1996; Xu, 2006; Feyisa et al., 2014) to supervised and unsupervised classifications (Thomson, 1998; Lira, 2006). Apart from some inherent shortcomings of these techniques such as challenges of defining robust thresholds for single bands or water indices (Ji et al., 2009), the classified maps are subject to uncertainties of partially neglecting the fractions of other classes within the mixed pixels. This problem would be highly pronounced for river boundaries that in vast majority of the cases run through the pixels leading to mixture with surrounding land covers.

Although several techniques are applied for retrieving sub-pixel details, most of the research has been limited to the estimation of water proportions regardless of sub-pixel mapping (e.g. Wang et al., 2015b; Ji et al., 2015). Concerned with sub-pixel mapping, there have been some attempts to apply SRM techniques for shoreline and waterline detection (Foody et al., 2003; Foody et al., 2005; Muslim et al., 2007), flood inundation mapping (Li et al., 2015a; Li et al., 2015b), as well as for river mapping (Niroumand-Jadidi and Vitti, 2015). Two key steps are required in order to address the problem in a proper way. First, water fractions should be estimated and then spatial distribution of the fractions is to be determined within each pixel. The former step is known widely as unmixing and the latter as SRM. Both of these steps are addressed herein in order to develop and evaluate the unmixing and SRM techniques for reconstruction of river channel boundaries at the sub-pixel resolution.

2.3 Proposed Methodology

As mentioned, estimation of water fractions is central for the sub-pixel mapping of river boundaries, which provides the input for SRM algorithms. Both real and semi-simulated water fractions are considered in order to isolate and examine the effect of fractions on final sub-pixel maps. The “semi-simulated” fractions are contrived input for SRM algorithms with known water fractions. As the real geometry of the river is considered for simulations, the term “semi-simulated” is preferred rather than “simulated”. On the other hand, the “real fractions” refers to the fractions obtained from unmixing of real imagery. These two testing scenarios are highlighted in the general workflow of the proposed methodology in Figure 2.1. The proposed methodology is elaborated in detail in the following sub-sections emphasizing both unmixing and SRM steps.

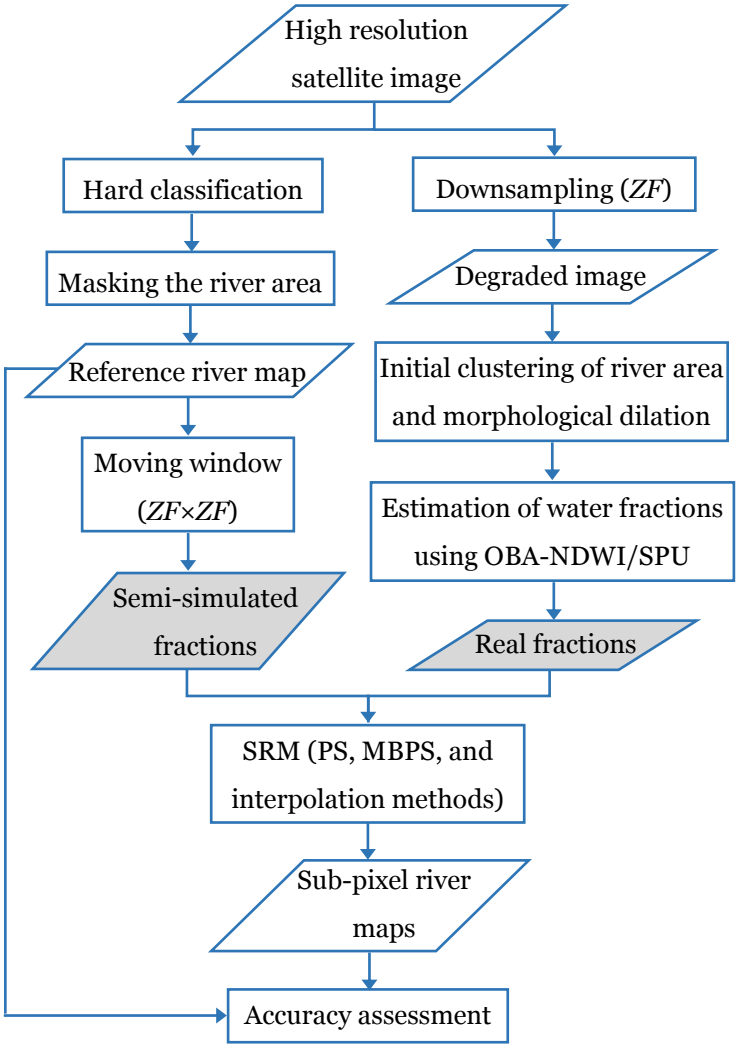

Figure 2.1 Flowchart of the proposed methodology for the mapping and assessment of river boundaries at the sub-pixel resolution using both real and semi-simulated fractions, ZF represents the zoom factor.

2.3.1 Estimation of Water Fractions

2.3.1.1 Semi-simulated Fractions

The accuracy of estimated water fractions can inescapably affect the output sub-pixel maps of SRM techniques. In order to evaluate the performance of SRM algorithms only through the spatial arrangement of sub-pixels, it is essential to supply the algorithms with fractions of no uncertainty. In support of this objective, semi-simulated fractions are contrived in such a way to provide known and free of error water fractions. The term “semi-simulated” is chosen because the

river area corresponding to the fractions is derived from real imagery and hence it has the natural shape and morphology of the real river.

The river area is initially masked out on the high resolution image using a hard classifier to take it as the reference map which has binary water/non-water labels. Then, a moving window with the dimensions equivalent to the desired zoom factor (*ZF*) is applied on the reference map. The number of water pixels is counted in each window which can be simply converted to the fractions in the [0, 1] range. The content of each window (i.e. number of water pixels) is known from the high resolution reference map; thereby the fractions can be considered known and with no uncertainty. For instance, semi-simulated fractions are calculated by moving a 5×5 window (*ZF=5*) on the reference water map in Figure 2.2. The semi-simulated fractions can provide free-of-error inputs not only for SRM algorithms but also for hard classifiers. This is because the most abundant class is known within the windows (coarse pixels). Therefore, a water/non-water label can be assigned without the usual uncertainties of hard classifiers concerned with spectral confusions and similarities existing among different land cover classes (Figure 2.2c). After the simulation of water fractions, SRM algorithms and conventional hard classification can be applied and compared. A possible random arrangement of sub-pixels for the given example is presented in Figure 2d where the goal of SRM algorithms is to find the proper spatial distribution of sub-pixels.

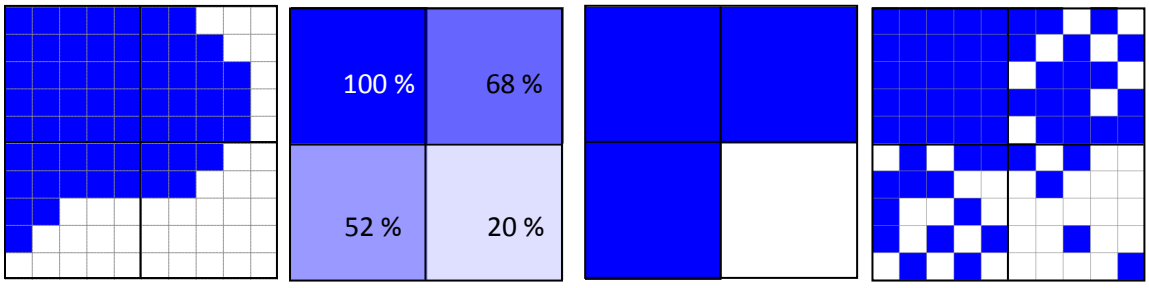

Figure 2.2 (a) Reference high resolution map, (b) semi-simulated fractions with *ZF=5*, (c) hard classified map, and (d) a possible random sub-pixel map.

2.3.1.2 Real Fractions

Real fractions are used to examine the accuracy of the entire procedure of sub-pixel mapping considering both unmixing and SRM stages. To this end, a new method based on water indices (i.e. OBA-NDWI) is developed for estimation of water fractions. The proposed method is compared with an advanced spectral unmixing method, namely the fully constrained simplex projection unmixing (SPU) developed by Heylen et al. (2011).

According to the proposed methodology (Figure 2.1), the river area and a buffer zone along the channel is initially masked by applying an unsupervised clustering followed by a morphological dilation. This is for ease of computations and selection of training samples. However, the unmixing procedure can be applied on the entire image scene. The unmixing methods are then applied on down-sampled imagery (with the same ZF of desired sub-pixel map) so that the hard classification of original high resolution images are considered as reference maps for accuracy assessment of sub-pixel maps (see Figure 2.1).

- **Optimal Bands Analysis for NDWI (OBA-NDWI)**

Making use of water indices has been a long-standing interest of researchers for delineating water features (McFeeters, 1996; Xu, 2006; Li et al., 2013, Xie et al., 2016). McFeeters (1996) developed the original normalized difference water index (NDWI) based on green (G) and near-infrared (NIR) bands of multispectral imagery (Equation 2.1). Afterward, Xu (2006) presented the modified NDWI (MNDWI) by replacing the NIR band with the shortwave-infrared (SWIR) band.

$$NDWI\_original = \frac{G - NIR}{G + NIR} \tag{2.1}$$

The spectral channels of WV-2 provide a wealth of choices for developing different types of spectral indices (e.g. water, vegetation and soil indices) compared to the conventional HRSI (e.g. Geoeye images). Different combinations of spectral bands can be considered for calculation of NDWI from WV-2 images; for instance, (G, NIR-2) and (coastal-blue (CB), NIR-2) are pairs of bands used in some previous research (Xiaocheng et al., 2012; Wolf, 2012; Maglione et al., 2014). More recently, Xie et al. (2016) considered the normalized ratio of a relatively high-reflective

band (b_h) and a low-reflective band (b_l) for which different pairs of bands can be employed for the computation of NDWI according to the following equation:

$$NDWI\_Xie = \frac{b_h - b_l}{b_h + b_l} \tag{2.2}$$

The outputs of NDWIs range from -1 to 1 where selection of an appropriate threshold is the main barrier to distinguish among water and non-water pixels (Ji et al., 2009; Feyisa et al., 2014). McFeeters (1996) and Xu (2006) considered zero as the threshold when they introduced NDWI and MNDWI. Ji et al. (2009) have investigated the efficiency of NDWIs by considering different combination of spectral bands on coarse and moderate-resolution imagery (e.g. MODIS and Landsat ETM+). They have determined threshold values based on synthetic mixture of the three dominant land-cover types (water, vegetation and soil). Moreover, Otsu's thresholding method (Otsu, 1979), which is based on the maximum between-class variance criterion, is used in several articles to mask out water pixels (Du et al. 2012; Li et al. 2013; Du et al., 2014). However, the main aim of previous research is mainly binary (hard) classification of water features whereas the estimation of water fractions received less attention.

In this research, image-derived spectra for the afore-mentioned major land-cover types (i.e. water, vegetation and bare earth/soil) are mixed linearly with all the possible fractions of the classes with one percent intervals. This approach has been adapted from Ji et al. (2009); however, in the case of presence of an outstandingly different major class (endmember), number of classes can be increased. Note that the number of classes cannot exceed the number of spectral bands to solve the common unmixing methods such as linear spectral unmixing and SPU (Mather, 2004). This issue can limit the number of unmixing classes using imagery with low spectral resolution. However, the mentioned three major classes which can be derived from grouping the sub-classes with similar spectral characteristics are representative for a wide range of applications and particularly for the riparian zones. This assumption on the number and type of major classes (endmembers) is well-established in the previous research (Wu, 2004; Ji et al., 2009; Wetherley et al., 2017).

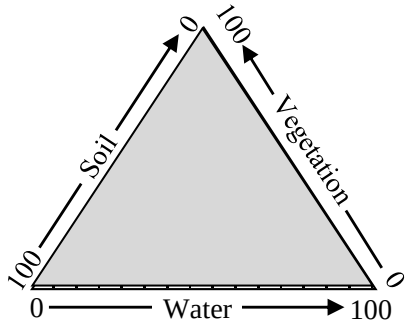

Figure 2.3 The scheme for linear spectral mixture of three dominant endmembers of land surface (i.e. water, vegetation and soil). Each point inside the triangle represents a possible combination of fractions; adapted from Ji et al. (2009).

After producing the synthetic spectra with all the possible fractions of the three classes, the NDWI values of the spectra are regressed against known water fractions. In this regard, an Optimal Band Analysis for NDWI (OBA-NDWI) is proposed to identify the pair of bands for which the corresponding NDWI values yield the highest correlation with the water fractions. All the possible combinations of spectral bands are considered to calculate the NDWI values (Equation 2.3) in order to examine their potential for estimation of water fractions by assessing the coefficient of determination and RMSE of the regression models. This provides a full search among all the possible options for choosing a pair of spectral bands which is also common in other applications such as bathymetry from optical imagery (Legleiter et al., 2009).

$$NDWI\_proposed = \frac{b_i - b_j}{b_i + b_j} \qquad (2.3)$$
$$i = \{1,2,\ldots,number\ of\ bands-1\},\quad j = \{i+1,\ldots,number\ of\ bands\}$$

After identification of the optimal combination of bands to be used for calculation of NDWI, the corresponding regression model is used to predict the water fractions of the image pixels. The regression-based approaches are previously used for estimation of fractional vegetation coverage using vegetation indices (Hurcom and Harrison, 1998; Elmore et al., 2000; Xiao and Moody, 2005) but have not been explored yet for estimation of water fractions based on water indices.

Moreover, the effectiveness of common thresholding methods is examined for the hard classification of river area using HRSI. In this regard, the sensitivity of thresholding methods on different NDWIs is investigated and accordingly the relevant cut-off water fraction for each NDWI

is determined. The determination of minimum water fraction within the masked pixels can reveal the performance of hard classification built upon each of thresholding methods. This is because, considering the concept of hard classification for binary mapping, at least half of a pixel should be occupied by the desired class (water) to be assigned to that class.

- **Simplex Projection Unmixing (SPU)**

The recent and advanced algorithm of SPU is also applied on the imagery to evaluate the efficiency of proposed OBA-NDWI method for estimation of water fractions. The SPU is a technique ensuring sum-to-unity as well as positivity of fractions. These constraints are prerequisites for most of SRM techniques such as the PS algorithm. The SPU method is built upon the geometrical interpretation of unmixing problem (Heylen et al., 2015). This algorithm uses a sequence of orthogonal projections on sub-simplexes formed by the endmembers. The solution derived from the SPU algorithm minimizes the least squares error while firmly respecting the sum-to-unity and non-negativity constraints on the fractions (see Heylen et al., 2011 for further mathematical details).

2.3.2 Super Resolution Mapping

SRM is required for spatial allocation of water fractions in order to reconstruct the river area at the sub-pixel level. Most of the SRM algorithms rely on maximizing the spatial proximity of sub-pixels with the same labels in their neighborhood (Atkinson, 2009; Wang et al., 2015). Several techniques are developed based on artificial intelligence optimization techniques such as genetic algorithms (Mertens et al., 2003; Tong et al., 2016) and neural networks (Tatem et al., 2001; Zhang et al., 2008) and also other methods based on Markov random fields (Wang and Wang, 2013). Besides these methods, the PS algorithm (Atkinson, 2005) is a widely-used and efficient method for SRM purposes (Xu and Huang, 2014). On the other hand, interpolation-based approaches could be considered as alternatives for SRM. These algorithms are non-iterative which can be an advantage when the computation time is considered. Although some interpolation methods (e.g. IDW and kriging) are tested for SRM using simulated imagery (Ling et al., 2013), a comparative analysis with respect to iterative techniques remains poorly investigated, particularly in terms of mapping water bodies. This research concentrates on the PS

algorithm as an iterative technique and a couple of interpolation methods as non-iterative solutions for sub-pixel mapping of river boundaries. In addition, a non-iterative approach is proposed for improving the speed of PS algorithm.

2.3.2.1 Pixel Swapping (PS)

The number of sub-pixels corresponding to the fraction of a given class within each pixel can be calculated based on the desired *ZF* according to the following equation:

$$N^k = round\ (F^k \times ZF^2), \tag{2.4}$$

where N^k and F^k stand respectively for the number of sub-pixels and fraction of the class *k* within a pixel. For the binary water/non-water classification, the number of sub-pixels is calculated for water class based on the Equation 2.4, and then its subtraction from ZF^2 gives the number of sub-pixels for the non-water class.

The PS algorithm (Atkinson, 2005; Thornton et al., 2006) allocates sub-pixel labels in random positions within each pixel. Then, the attractiveness of each sub-pixel with respect to a particular class is predicted as a distance-weighted function of its neighbors according to the following equation:

$$A^k = \sum_{i=1}^{n} \frac{F_i^k}{d_i}, \tag{2.5}$$

where A^k denotes the attractiveness of a sub-pixel with respect to the class *k*, F_i^k is the fraction of class *k* in the *i-th* neighbor pixel. The number of neighbor pixels is *n,* and d_i is the distance of the *i-th* neighbor pixel from the sub-pixel for which the attractiveness is computed.

Considering the attractiveness values of the class *k* in a pixel, the least attractive sub-pixel location initially allocated to the desired class (e.g. water) should be identified as well as the most attractive location initially allocated to the other class (e.g. non-water). If the attractiveness of the least attractive location is less than that of the most attractive location, then the classes are swapped, otherwise no change is made (Thornton et al., 2006; Atkinson, 2009). After applying

the swapping process on all image pixels, this process should be iterated until reaching a point that the algorithm is not able to perform anymore swaps. An example of the swapping process is illustrated in Figure 2.4 where the central pixel with 58% water fraction is divided to nine sub-pixels (*ZF=3*) and the attractiveness of each sub-pixel is calculated based on the eight neighboring pixels.

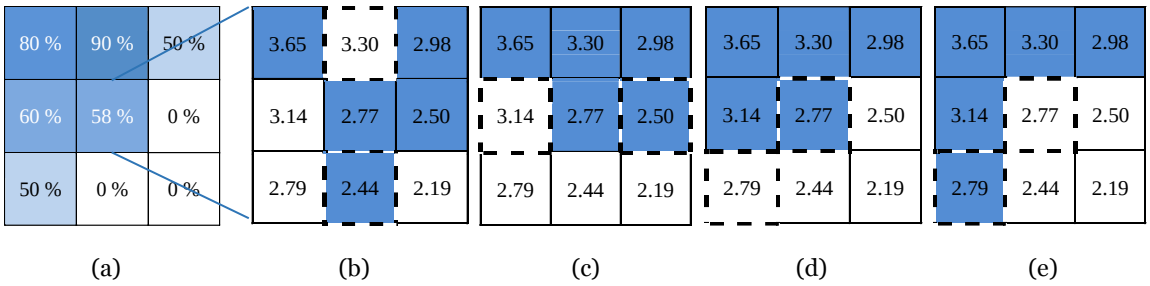

Figure 2.4 Water fractions and the PS process for spatial allocation of sub-pixels for a given pixel; (a) water fractions, (b) random allocation of sub-pixels, (c, d, e) swaps (candidate sub-pixels for swapping are highlighted by dash-lines); values of sub-pixels represent their attractiveness toward water class.

2.3.2.2 Modified Binary Pixel Swapping (MBPS)

After calculation of the attractiveness values for sub-pixel locations, the original PS algorithm commences with a random allocation of sub-pixels and then maximizes the spatial dependency in an iterative manner. This can be a barrier in terms of computational time when applying the algorithm on large extents. To tackle this problem, a simple non-iterative solution is examined in this research for the spatial allocation of binary classes (e.g. water and non-water). The proposed method suggests to simply allocate the sub-pixels of the desired class (water) in the N^k locations with the highest attractiveness values toward that class. The remaining sub-pixel locations are then directly assigned to the other class (non-water). The proposed modified binary PS (MBPS) method is applied on the same example discussed in Figure 2.4. In this case, the resultant sub-pixel map is the same as that of the original PS algorithm (Figure 2.5).

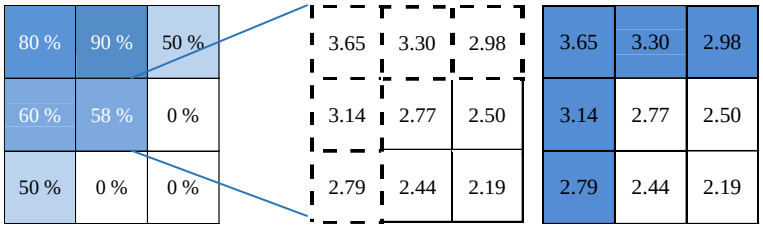

Figure 2.5 Water fractions and the proposed MBPS for spatial allocation of sub-pixels for a given pixel; (a) water fractions, (b) identification of sub-pixel locations with highest attractiveness, highlighted by dash-lines, (c) allocation of water and non-water sub-pixels; values of sub-pixels represent their attractiveness toward water class.

2.3.2.3 Interpolation-based SRM

The interpolation methods can be employed to develop non-iterative SRM. Assigning the fractions of classes to the center of the corresponding pixels, sub-pixel fractions can be estimated using common interpolation methods. In this research, several techniques including bilinear, bicubic and lanczos3 are tested; an example using bilinear method is shown in Figure 2.6. A hard labeling process can be applied then on interpolated points (i.e. sub-pixels) in such a way to assign each sub-pixel to the class with the highest estimated fraction. The main advantage of this technique is that the labeling procedure can be done in a single step which can improve the computational efficiency.

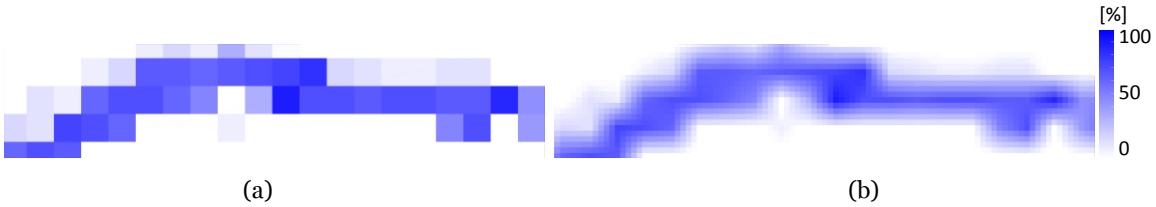

Figure 2.6 An example of bilinear interpolation of water fractions; (a) water fractions at the pixel level, (b) interpolated water fractions at the sub-pixel level with *ZF*=5.

2.4 Study Area and Dataset

Sarca and Noce, two Alpine rivers located in northeast Italy, are considered as the case studies (Figure 2.7). The areas of interest are about 19 km and 8 km long reaches, for Sarca and Noce rivers, respectively. As the studied rivers are narrow (about 20 m mean channel width), HRSIs

including a WV-2 image of the Sarca and Geoeye image of the Noce are selected. The use of both WV-2 and Geoeye images can also reflects the influence of additional spectral bands of WV-2 sensor for river mapping issues. It should be noted that the image of Sarca River is captured by the WV-3 sensor. However, only the 8-bands corresponding to that of the WV-2 are used, and then it is herein referred to the WV-2 sensor.

(a) (b)

Figure 2.7 True color composites of (a) WV-2 image of Sarca River and (b) Geoeye image of Noce River; the river channels are highlighted by blue lines.

2.5 Implementations and Results

2.5.1 Estimation of Water Fractions

Semi-simulated fractions are produced along the two rivers based on the methodology described in Section 2.3.1.1. As discussed in detail, this provides an input without any error for SRM methods as well as for the hard classification. The sub-pixel detail neglected by hard classifiers and the performance of SRM methods through allocation of sub-pixels are investigated thoroughly (Section 2.5.2).

Toward estimation of real water fractions using the proposed method relying on OBA-NDWI, training samples for the three desired classes (i.e. water, vegetation and soil) are selected from the imagery. The spectra of the endmembers are estimated based on the average values of the samples which are selected from different spots distributed along the rivers. For each endmember, about 30 pixels are selected by visual interpretation. Then the linear mixture is

performed to simulate all the possible fractions concerned with the three endmembers. NDWIs with all the possible combinations of spectral bands are applied on the synthetic WV-2 and Geoeye spectra; the outputs are plotted against the known values of water fractions (some examples are shown in Figures 2.8 and 2.9). The regression model providing the highest correlation is then used to predict the water fractions of all image pixels. In addition, zero-thresholds and Otsu's thresholds are applied on NDWI values to assess these two conventional threshold methods for hard delineation of water bodies.

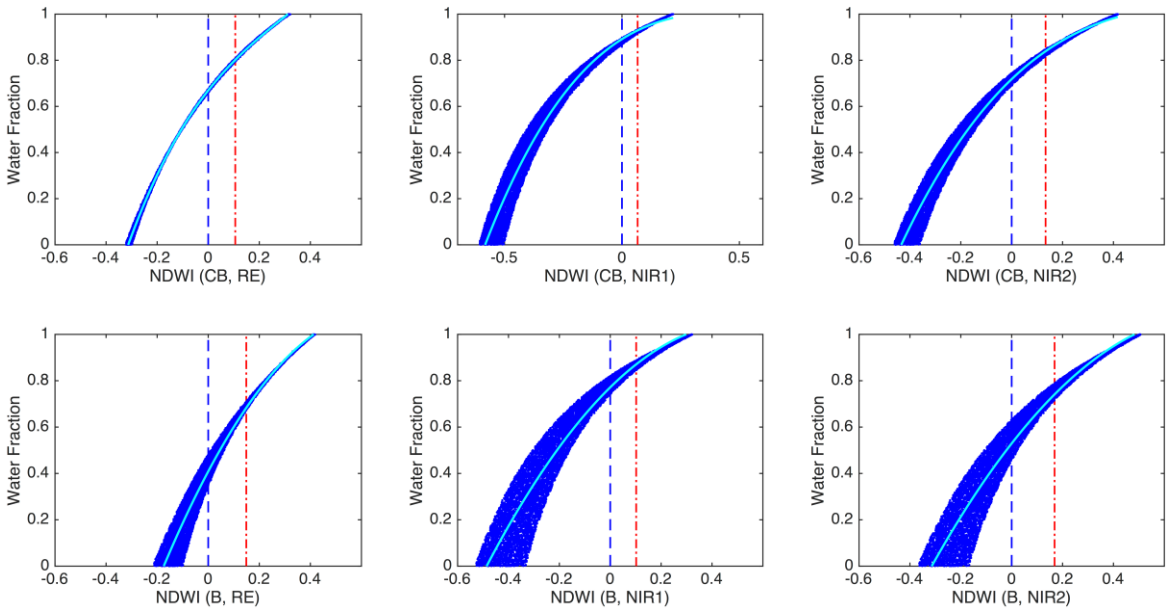

Figure 2.8 The regressions of NDWI values with different band combinations obtained from synthetic WV-2 spectra against known water fractions; the pair of bands used for calculation of NDWI is indicated on each graph (CB and RE stand for coastal-blue and red-edge bands, respectively); zero-threshold and Otsu's threshold are illustrated respectively with blue (dashed) and red (dot-dashed) lines.

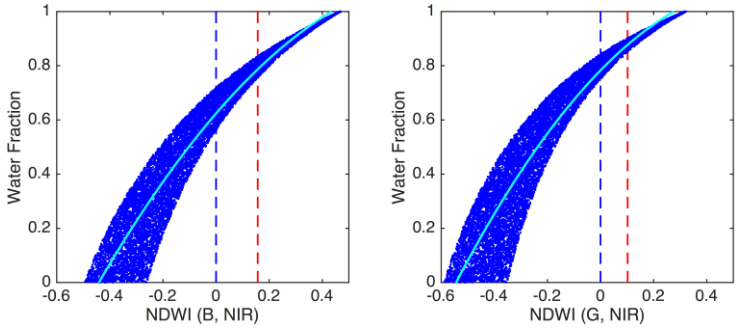

Figure 2.9 The regressions of NDWI values with different band combinations obtained from synthetic Geoeye spectra against known water fractions; the pair of bands used for calculation of NDWI is indicated on each graph; zero-threshold and Otsu's threshold are illustrated respectively with blue (dashed) and red (dot-dashed) lines.

As evident in Figure 2.8 and 2.9, the water fractions corresponding to zero-threshold and also Otsu's threshold are variable for different NDWIs and their difference can be outstanding. The minimum water fraction associated with zero-threshold on WV-2 image is significantly variable, from 87% to 35% for the NDWIs constructed respectively by two band combinations of (CB, NIR1) and (B, RE). This variation ranges from 91% to 67% for the Otsu's threshold with the same NDWIs. These fluctuations also exist for the Geoeye image for which the minimum water fraction for zero-threshold ranges from 57% to 75%, and for the Otsu's threshold from 75% to 85%, respectively using NDWIs based on (B, NIR) and (G, NIR) pairs of bands (Figure 2.10). Therefore, the range of water fractions of masked out pixels based on common thresholding methods can be variable depending on the spectral bands used in the calculation of NDWI. With generalization of all the classes excluding the water class to a single non-water class, each pixel with a minimum 50% water content can be labeled as water. This is a binary hard classification scheme which can be considered for delineation of water bodies based on thresholding on NDWI values. Keeping this in mind, Figure 10 reveals that Otsu's thresholding most probably occurs above the 50% water fraction which leads to underestimation of water pixels. For instance, the pixels with fractions ranging from 50% to 85% will be mislabeled as non-water pixels for the NDWI based on (B, NIR1) bands. On the other hand, zero-thresholding deals with both underestimation and overestimation of water pixels. For instance, every pixel with the minimum 35% water content will be labeled as water by applying zero-threshold on NDWI obtained from (B, RE) bands. This kind of mislabeling at the pixel level can increase the uncertainty of water mask in mixed

boundary pixels. However, extraction of the pure (near pure) water pixels in the main river channel would be less challenging.

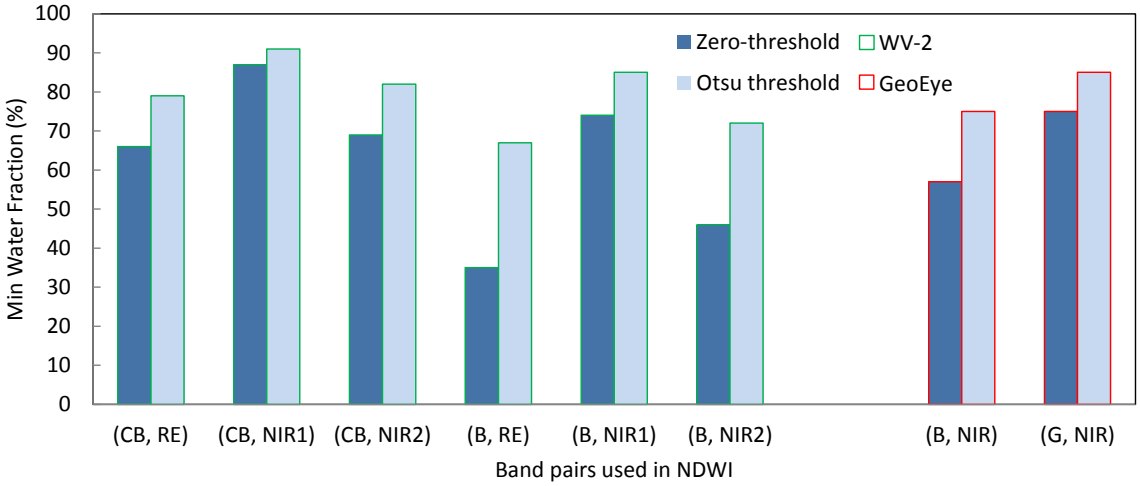

Figure 2.10 Minimum water fractions corresponding to zero-threshold and Otsu's threshold for several NDWIs using synthetic WV-2 and Geoeye spectra; CB and RE stand, respectively, for coastal-blue and red-edge bands.

The proposed OBA-NDWI method is applied on the synthetic spectra in order to exploit the strongest relation between water fractions and NDWI values (the regression lines are illustrated on Figure 2.8 and Figure 2.9). The OBA-NDWI performs quadratic regression of NDWI values versus water fractions for all possible combinations of spectral bands in order to identify the optimal pair of bands which their corresponding NDWI yields the highest coefficient of determination (R^2). Consideration of all the possible pair of bands is a systematic approach to identify the optimal structure of the NDWI that the results are in line with the assumption of Xie et al. (2016) regarding the use of a relatively high-reflective band and a low-reflective band for calculation of the NDWI. As illustrated in Figure 2.11, coastal-blue (CB), blue (B), and green (G) bands can be considered as optimal high-reflective bands (b_h) while the portion of spectrum covering red-edge (RE), NIR1, and NIR2 could be effective as low-reflective bands (b_l) using the WV-2 image. In particular, CB and RE bands provide the strongest relation with an R^2 on the order of 97% and an RMSE of 2%. Blue and NIR are the optimal pair of bands for the Geoeye image. Their corresponding NDWI yields an R^2 value of 92% and an RMSE value of 7% through a quadratic relation with water fractions (Figure 2.12).

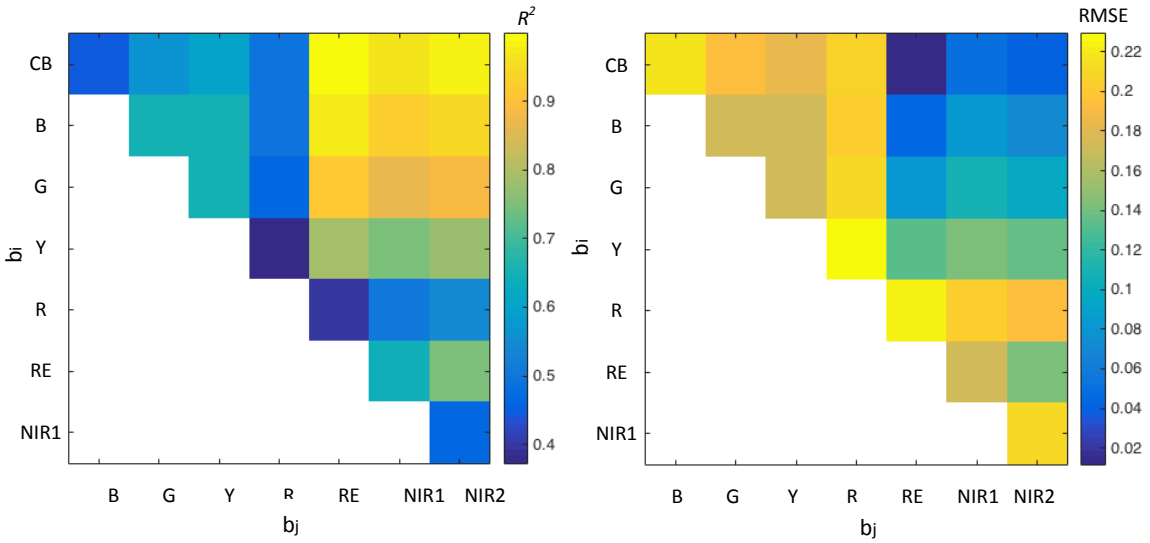

(a) (b)

Figure 2.11 OBA-NDWI for the synthetic WV-2 spectra; all possible combinations of spectral bands are considered in the structure of NDWI to perform a quadratic regression against water fractions. Values of (a) R^2 and (b) RMSE are represented by color bars.

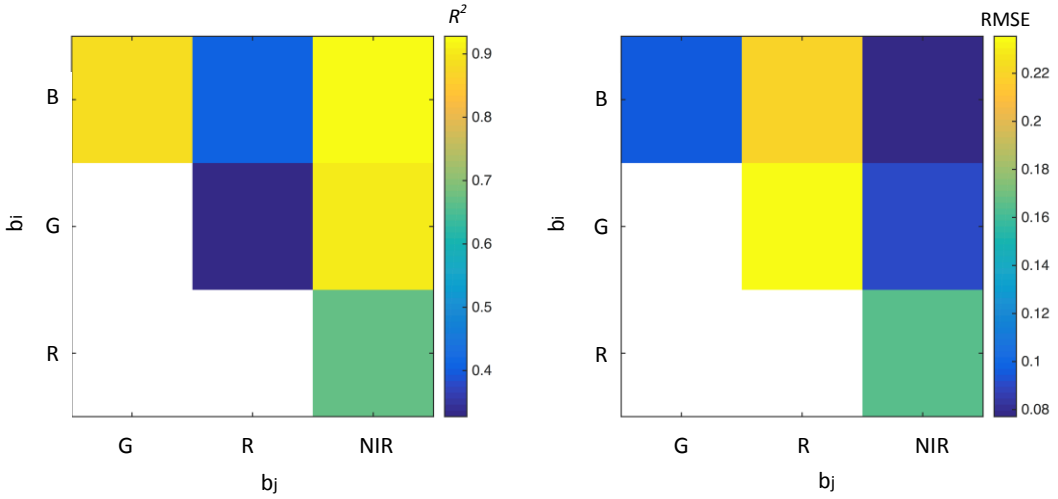

(a) (b)

Figure 2.12 OBA-NDWI for the synthetic Geoeye spectra; all possible combinations of spectral bands are considered in the structure of NDWI to perform a quadratic regression against water fractions. Values of (a) R^2 and (b) RMSE are represented by color bars.

The quadratic model obtained for the optimal pair of bands is used to predict the water fractions of all image pixels. Moreover, the same endmembers used for linear mixtures are introduced to

the SPU algorithm and the resultant fractions are compared with those obtained from the proposed method (Figure 2.13). In general, a strong correlation (R^2=90%, RMSE=7% for the WV-2 image and R^2=87%, RMSE=9% for the Geoeye image) is observed between the estimated fractions of the proposed OBA-NDWI method and the SPU algorithm.

(a) (b)

Figure 2.13 Water fractions of the WV-2 image obtained from (a) proposed OBA-NDWI method and (b) SPU algorithm.

2.5.2 Super Resolution Mapping (SRM)

The semi-simulated as well as the real water fractions are used as inputs for SRM algorithms. The super resolved maps obtained from the semi-simulated fractions are represented for a river segment in Figure 2.14. The sub-pixel mapping procedure of interpolation-based techniques is also illustrated in Figure 2.15 where the interpolated water fractions are represented (Figure 2.15d) along with the hard labels assigned to each sub-pixel (Figure 2.15e). As it is clear from the illustrations, hard classification is very rough on the river boundaries while the SRM techniques reconstruct boundaries with sub-pixel details.

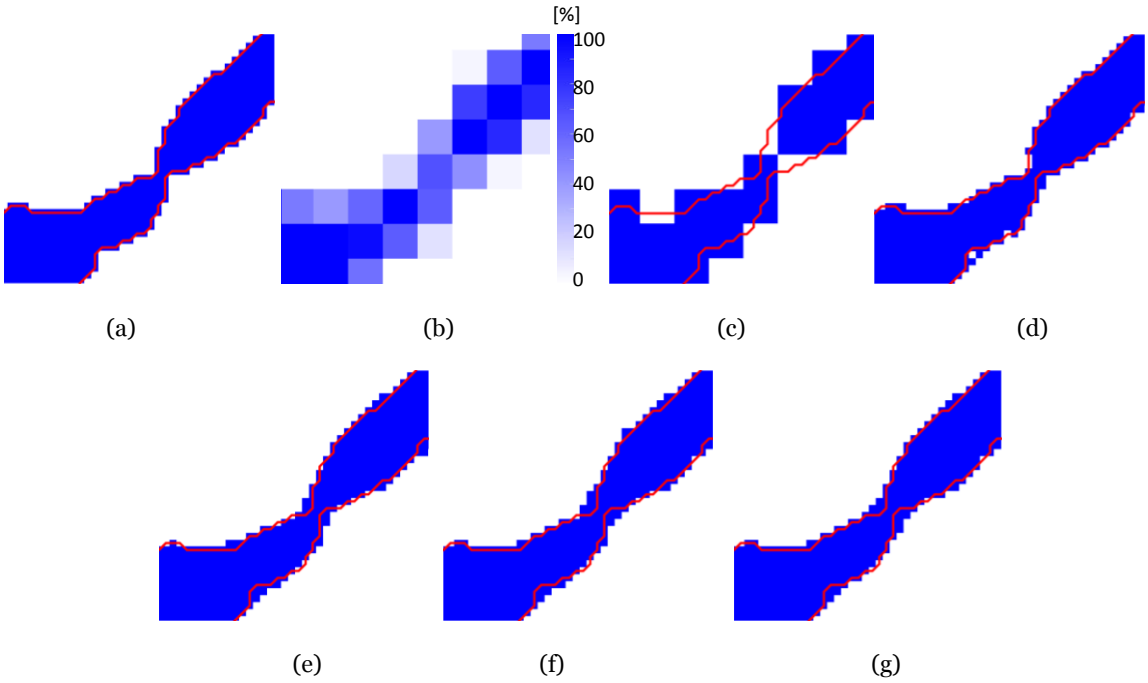

Figure 2.14 Sub-pixel maps resultant from different SRM algorithms using semi-simulated water fractions: (a) reference map, (b) semi-simulated water fractions (*ZF=5*), (c) hard classified map, sub-pixel maps of (d) PS, (e) bilinear, (f) bicubic, and (g) lanczos3 algorithms; reference river boundaries are represented by red lines on each map.

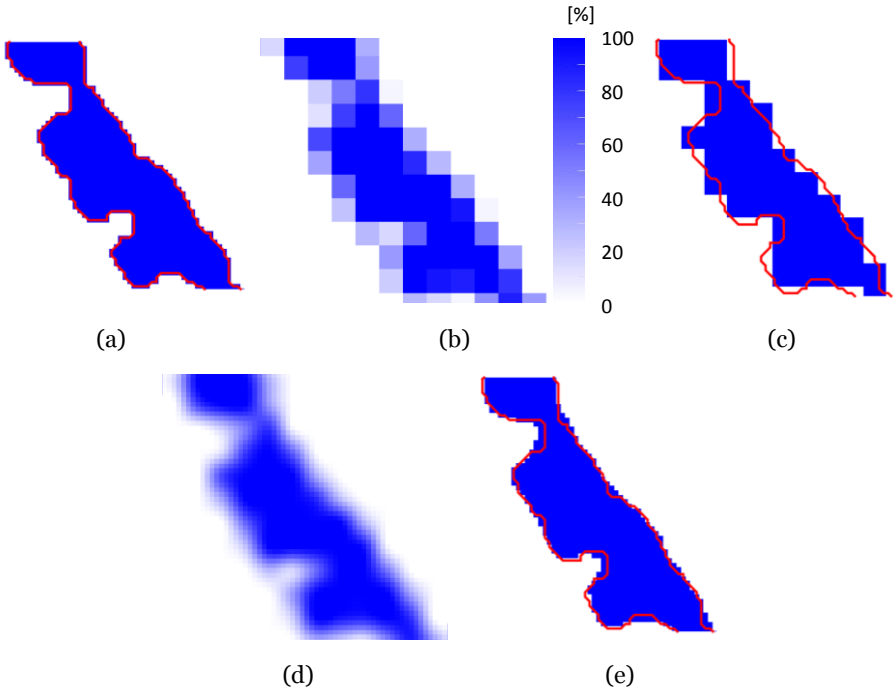

Figure 2.15 Interpolation-based SRM using semi-simulated water fractions: (a) reference map, (b) semi-simulated water fractions (*ZF=5*), (c) hard classifed map, (d) bicubic interpolation and (e) sub-pixel map.

User and producer accuracies of the river area extracted from hard classification and SRM of semi-simulated fractions are presented in Figures 2.16 and 2.17 for Sarca and Noce rivers, respectively.

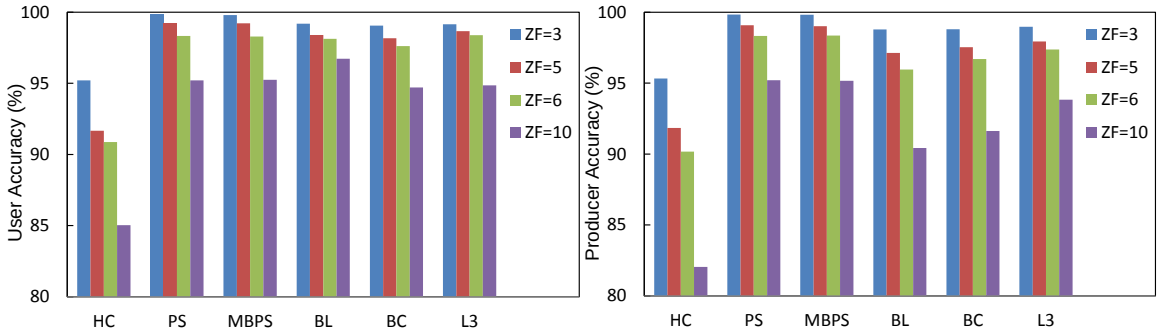

Figure 2.16 User and producer accuracies of hard classification and SRM algorithms using semi-simulated water fractions across a range of *ZF* for Sarca River; (HC: hard classification, PS: pixel swapping, MBPS: modified binary PS, BL: bilinear, BC: bicubic, L3: lanczos3).

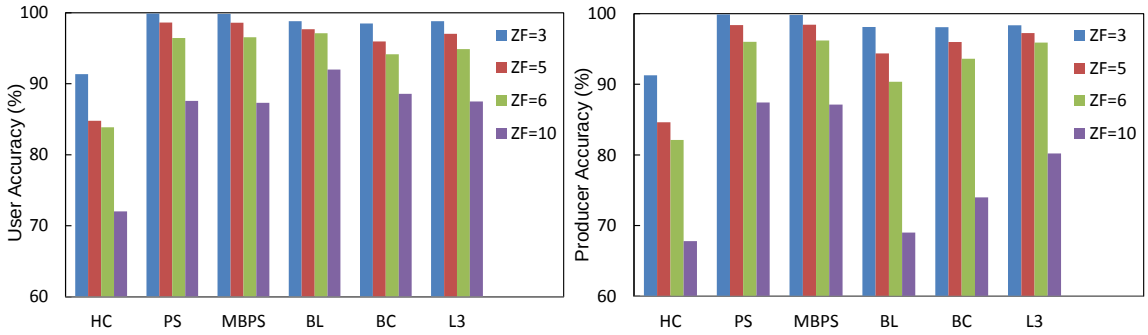

Figure 2.17 User and producer accuracies of hard classification and SRM algorithms using semi-simulated water fractions across a range of *ZF* for Noce River; (HC: hard classification, PS: pixel swapping, MBPS: modified binary PS, BL: bilinear, BC: bicubic, L3: lanczos3).

The user/producer accuracies of hard classification are remarkably lower than that of sub-pixel maps. This emphasizes the weakness of this type of classifier in the presence of mixed boundary pixels. For instance, the error maps of hard classification and a sub-pixel map of same area are represented in Figure 2.18 which shows that the hard classified map encompasses a large number of misclassified pixels. This issue gets worse with higher *ZF* where the difference between the accuracies of hard classification and SRM methods reaches above 10%. In general, interpolation-based SRM and MBPS lead to comparable accuracies with respect to the PS algorithm except at

higher zoom factors (*ZF=10*) where the producer accuracies of interpolation-based techniques are lower.

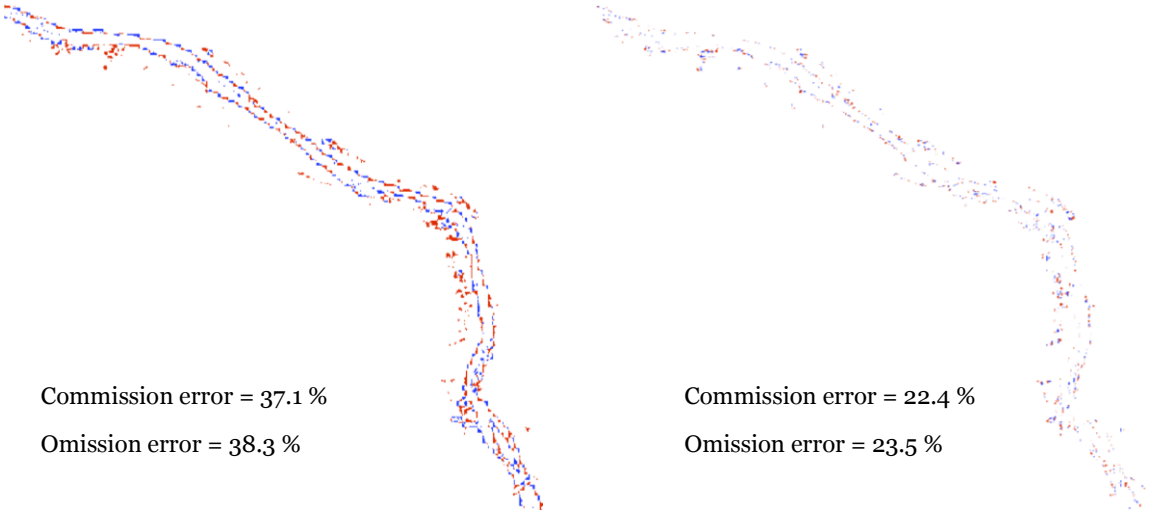

Figure 2.18 Error maps of (a) hard classification and (b) sub-pixel map obtained from MBPS for a segment of Sarca River using the WV-2 image with *ZF*=6, red and blue pixels show erroneously committed and omitted water pixels, respectively.

The real water fractions obtained from the SPU algorithm as well as those obtained from the proposed OBA-NDWI are used to supply the SRM algorithms. This provides the possibility of investigating the effect of uncertainties associated with water fractions on the final sub-pixel maps. Figure 2.19 illustrates the sub-pixel maps based on water fractions derived from the OBA-NDWI method. In Figure 20, outputs of the PS/MBPS algorithms are selected from parts of maps where some isolated groups of sub-pixels exist inside the river channel, which is due to errors of estimated water fractions. However, applying a majority filter on the resultant sub-pixel maps can reduce this drawback in order to produce homogenous maps (Figure 2.20e). These gaps, caused by underestimation of water fractions by unmixing methods either the OBA-NDWI or the SPU, obviously are not apparent on the maps of interpolation-based SRM methods due to interpolated values of fractions.

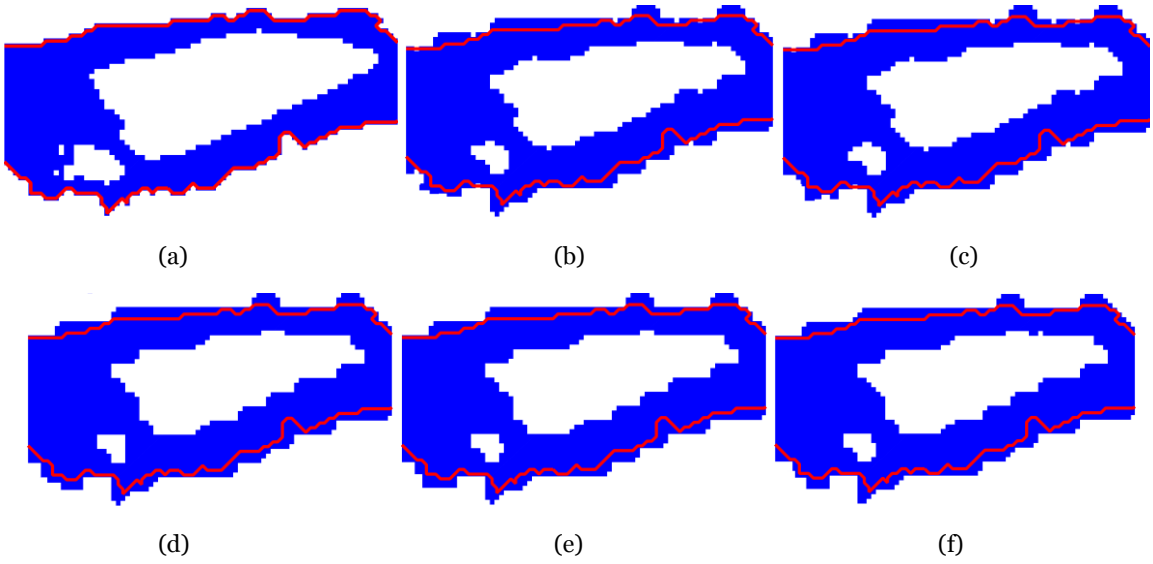

Figure 2.19 Sub-pixel maps obtained from real water fractions based on OBA-NDWI algorithm for Sarca River: (a) reference map, sub-pixel maps of (b) PS, (c) MBPS, (d) bilinear, (e) bicubic, and (f) lanczos3 algorithms, *ZF=5*.

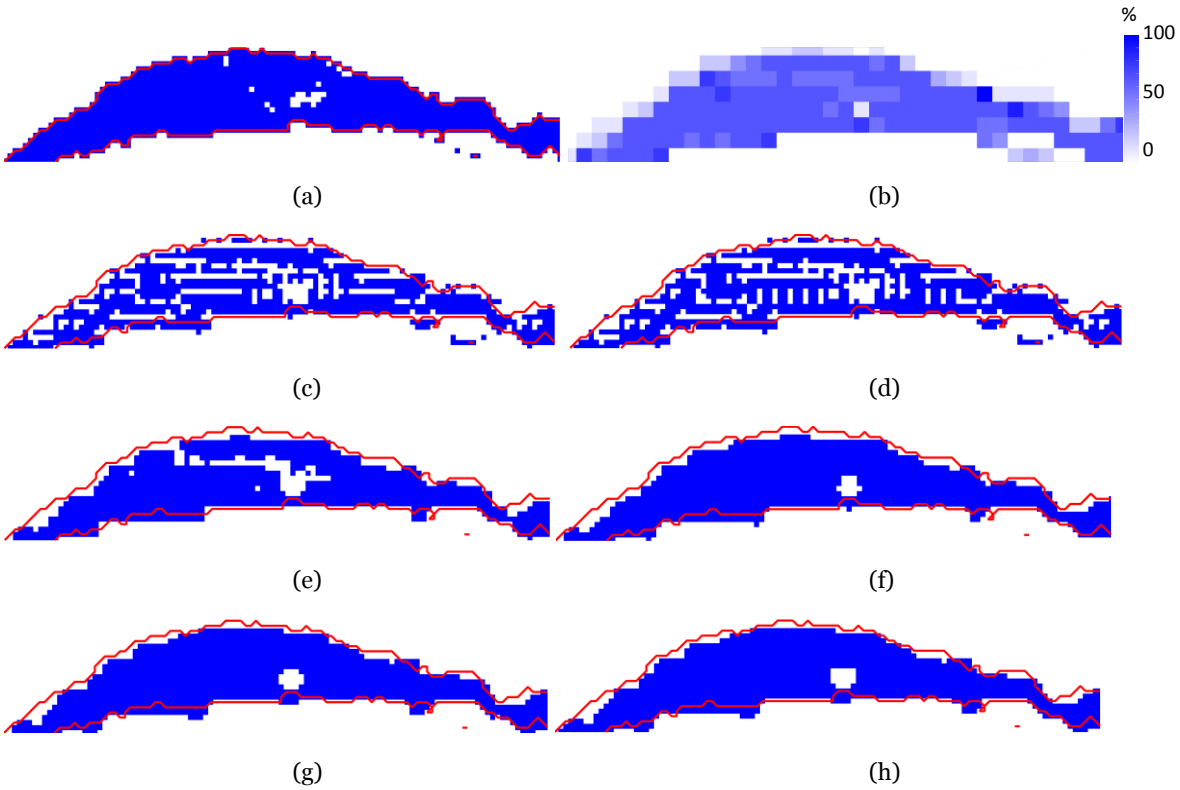

Figure 2.20 Sub-pixel maps obtained from real water fractions based on OBA-NDWI algorithm for Noce River: (a) reference map, (b) real water fractions based on OBA-NDWI algorithm; sub-pixel maps of (c) PS,

(d) MBPS, (e) majority filter applied on MBPS, (f) bilinear, (g) bicubic, and (h) lanczos3 algorithms, *ZF=5*.

User and producer accuracies of the sub-pixel river maps resultant from SRM of real fractions associated with the SPU and the OBA-NDWI algorithms are illustrated respectively in Figures 2.21 and 2.22 for Sarca and Noce rivers, respectively.

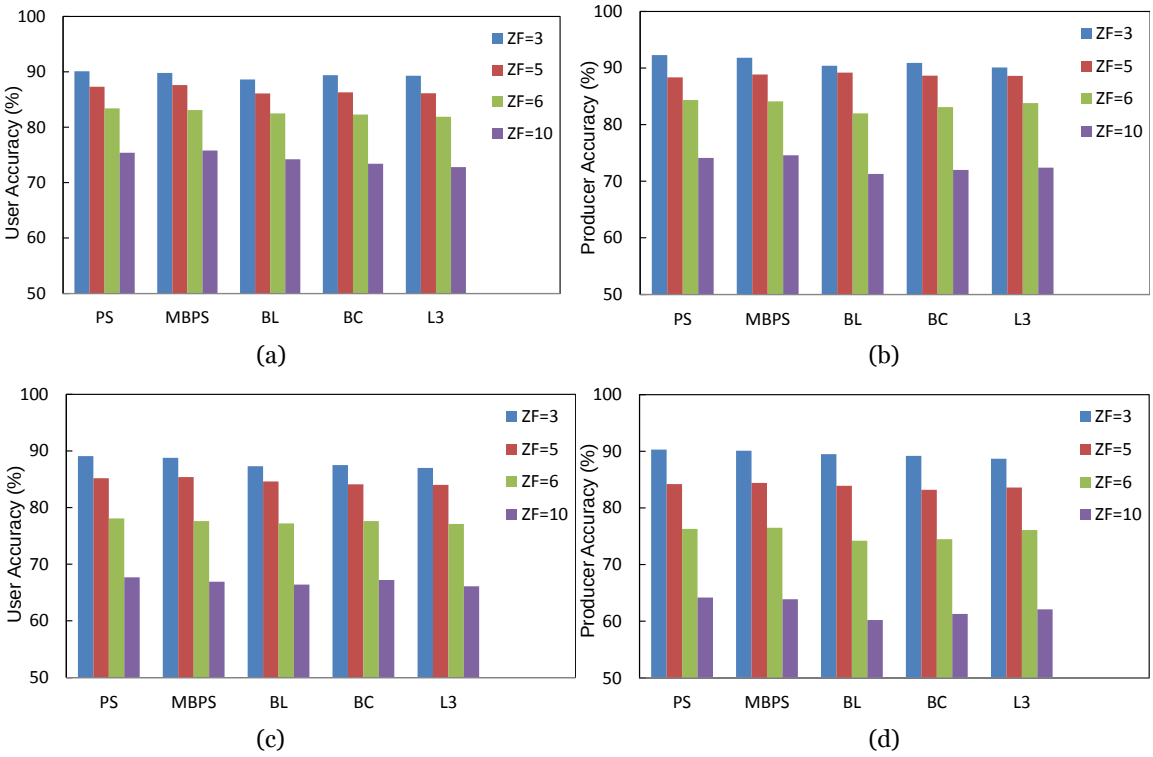

Figure 2.21 User and producer accuracies of SRM algorithms using real water fractions of: (a, b) the SPU algorthom, and (c, d) the OBA-NDWI algorithm across a range of *ZF* for Sarca River; (PS: pixel swapping, MBPS: modified binary PS, BL: bilinear, BC: bicubic, L3: lanczos3).

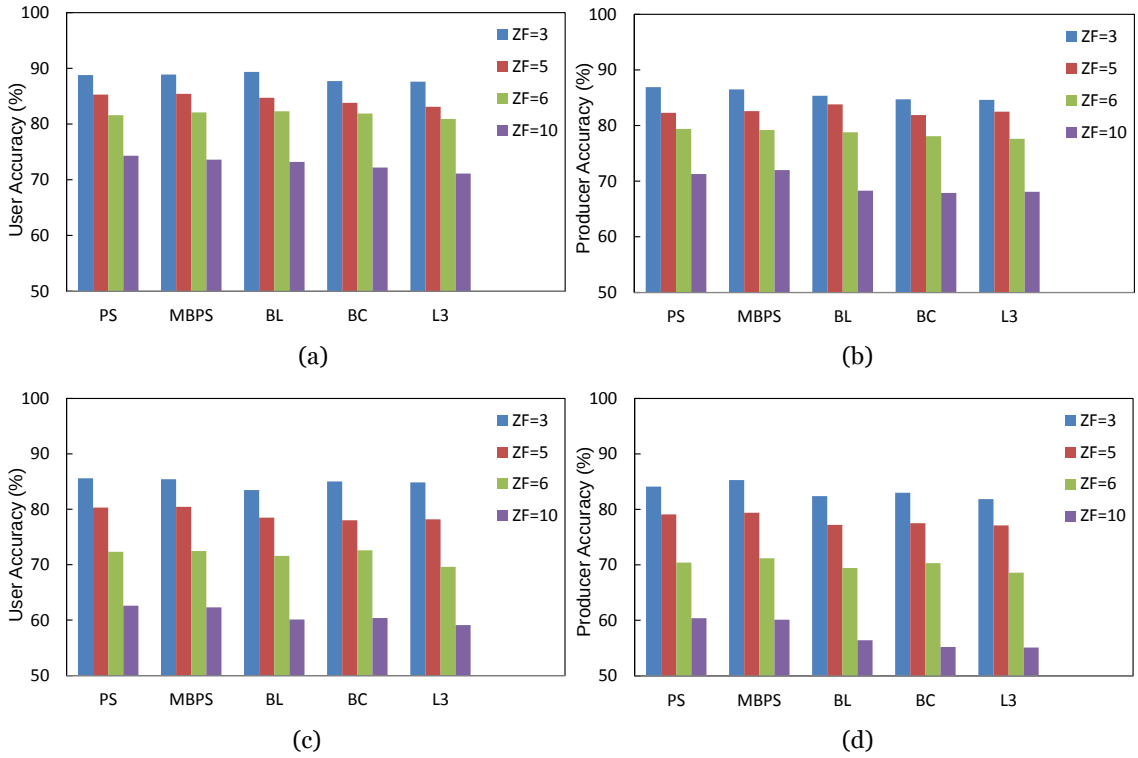

Figure 2.22 User and producer accuracies of SRM algorithms using real water fractions of: (a, b) the SPU algorithm, and (c, d) the OBA-NDWI algorithm across a range of *ZF* for Noce River; (PS: pixel swapping, MBPS: modified binary PS, BL: bilinear, BC: bicubic, L3: lanczos3).

Obviously, the accuracies of sub-pixel maps are decreased in the presence of uncertainties related to unmixing. However, the sub-pixel maps are accurate up to 90% with $ZF \leq 5$. The accuracies of sub-pixel maps associated with water fractions derived from the proposed OBA-NDWI are comparable with those obtained from the SPU. This is while the proposed method is simpler and easy to be numerically implemented and applied for water mapping issues.

Regarding the computational cost of SRM techniques, interpolation-based techniques and the MBPS algorithm are on average 20 times and 3 times faster than the original PS algorithm, respectively. This is because the interpolation-based and MBPS algorithms allocate sub-pixels in a non-iterative process and also the calculation of attractiveness for sub-pixel locations is not required for interpolation-based SRM.

Chapter 3: River Bathymetry

3.1 Introduction

Bathymetry is one of the key applications of remote sensing to fluvial systems that facilitates understanding the river form, process and function (Shintani and Fonstad, 2017). Information on water depth can play a decisive role in, for instance, mapping in-stream habitats (Bergeron and Carbonneau, 2012; Carbonneau et al., 2012; Hugue et al., 2016), parameterization and analysis of hydro-morphological processes (Bryant and Gilvear, 1999; Flener et al., 2012; Demarchi et al., 2016) as well as river management (Legleiter et al., 2002; Bizzi et al., 2016; Rinaldi et al., 2017).

Optical sensors onboard aerial and satellite platforms have long been used for studying shallow coastal environments (Lyzenga, 1978; Lyzenga, 1981, Philpot, 1988; Dierssen et al., 2003; Louchard et al., 2003; Lesser and Mobley, 2007). Because of their smaller spatial scales, fluvial systems have mostly utilized aerial imagery (Winterbottom and Gilvear, 1997; Jordan and Fonstad 2005; Walther et al., 2011; Legleiter, 2013). With the recent enhancements in spatial resolution of satellite imagery, river bathymetry from space is receiving more interest due to larger spatial coverage and higher temporal resolution of satellite sensors than those onboard aerial platforms. Legleiter and Overstreet (2012) performed a feasibility assessment on mapping bathymetry of gravel-bed rivers for the first time from space and in particular using WorldView-2 (WV-2) imagery. The theoretical basis of bathymetric models in the context of riverine environments is built upon the research conducted in coastal settings (Legleiter et al., 2004; Legleiter et al., 2009). The primary work of Lyzenga (1978, 1981) provides a backbone for physics-based retrieval of water depths from optical imagery. Lyzenga's model assumes a linear relation

between an image-derived quantity (X) and the water depth (d) where X is a predictor obtained from log-transformation of image values in a given spectral band. Multiple regression (Lyzenga, 1985; Lyzenga et al., 2006) and ratio methods (Stumpf et al., 2003) enhance the robustness of bathymetry retrievals with respect to substrate variability and water quality heterogeneity. The first employs multiple spectral bands to perform a multiple linear regression between image-derived predictors (X) and water depths (d) while the latter model considers a log-transformed band ratio as a predictor of the water depth. Each type of predictor is reported as an efficient one in different case studies (Legleiter et al., 2012; Bramante et al., 2013; Jawak and Luis, 2016). More recently, an enhanced ratio model called optimal band ratio analysis (OBRA) has been developed to identify a pair of bands among all the possible pairs for which the ratio model yield the strongest correlation with water depths (Legleiter et al., 2009). Three main objectives are followed in this study: (1) developing a new approach called multiple optimal depth predictors analysis (MODPA) for bathymetry retrieval by identifying and incorporating optimal depth predictors: the initial predictors space is expanded by considering all the possible Lyzenga and ratio predictors as well as some extra predictors from color space transformation. Then a set of optimal predictors are selected among the others to estimate the parameters of a linear model. The selection of optimal predictors is performed based on several feature selection methods including partial least square (PLS), stepwise and principal component (PC) regressions; (2) assessing the robustness of proposed MODPA compared to currently available models with respect to changes in substrate types, inherent optical properties (IOPs) and atmospheric effects: bathymetry models are comprehensively examined using spectroscopic experiments, simulations from radiative transfer modeling as well as WV-2 imagery. The Spectroscopic experiments are conducted in controlled condition of a hydraulic laboratory to collect a set of spectra in a range of water depths with variable substrates. The effects of IOPs including chlorophyll-a (Chl-a), total suspended solids (TSS) and colored dissolved organic matter (CDOM) are isolated using simulations from radiative transfer modeling. Moreover, an optically complex testing scenario is considered where bottom type and IOPs are all assumed as variables. Further, the proposed technique is examined on bathymetry mapping of Sarca River, a shallow and narrow alpine river in Italy, using WV-2 imagery. This reflects the performance of MODPA compared to other models in a spectrally complex environment of a real river. Moreover, the effect of atmospheric correction

is examined on bathymetry models due to remarkable contribution of atmosphere in the total at sensor radiance over water bodies (Gitelson and Kondratyev, 1991; Pahlevan et al., 2017b; Mouw et al., 2015). The newly released surface reflectance product of DigitalGlobe (2016) called atmospheric compensation (AComp) is assessed to understand the effect of atmospheric corrections on retrieving the river bathymetry from WV-2 imagery; (3) assessing the efficacy of WV-2 sensor's additional spectral bands compared to traditional 4-band high resolution satellite imagery (HRSI) such as GeoEy: to investigate this issue, the spectral data are matched with WV-2 and GeoEye bands using spectral convolution when needed.

The following Section outlines the theoretical background concerned with bathymetry from optical imagery. Section 3.3 introduces the proposed MODPA for bathymetry retrieval. The spectroscopic experiments conducted in the hydraulic laboratory, simulations from radiative transfer modeling and also in-situ measurements of water depths associated with HRSI of the study area are described in Section 3.4. Section 3.5 presents the results of implementations.

3.2 Bathymetry from Optical Imagery

Regarding optical remote sensing of water bodies, the total radiance reaching to the sensor at a given wavelength, $L_T(\lambda)$, consists of four main components upwelling from bottom, $L_b(\lambda)$, column, $L_c(\lambda)$, and surface, $L_s(\lambda)$, of the water body as well as the atmospheric effects, $L_p(\lambda)$, which are summarized in the following equation (Legleiter et al., 2004; Legleiter et al., 2009):

$$L_T(\lambda) = L_b(\lambda) + L_c(\lambda) + L_s(\lambda) + L_p(\lambda) \tag{3.1}$$

Aside $L_p(\lambda)$, each of the above-mentioned radiance components can be associated to a specific property of the water body. For instance, surface component of the radiance can be linked to the roughness of the water surface which in turn is a function of local hydraulics in riverine environments and can potentially reveal information about the flow velocity (Overstreet and Legleiter, 2017). The bathymetry information is embedded in the bottom component of radiance

which is affected not only by water depth but also the bottom type (Lee et al., 1998; Stumpf et al., 2003; Legleiter et al., 2009). Thus, it is essential to isolate the radiance component of interest or to reduce the effect of other undesirable components to retrieve a desired parameter which is the water depth in this study.

Lyzenga's model (1978, 1981) permits bathymetry retrieval from optical imagery, the model is built upon Beer-Lambert law to describe the exponential attenuation of light through travelling the water column. This model (see Equation 3.2) considers a deep-water correction to account for the undesirable radiance components upwelling from water column, water surface and atmospheric path radiance. The contribution of bottom reflected radiance can be considered negligible for radiances observed over optically deep water ($L_w(\lambda)$). Therefore, subtraction of $L_w(\lambda)$ from all water pixels leaves out the bottom component of radiance which is desirable for bathymetry mapping. Lyzenga's model hence reads:

$$X = \ln(L_T(\lambda) - L_w(\lambda)), \qquad L_w(\lambda) = L_c(\lambda) + L_s(\lambda) + L_p(\lambda) \tag{3.2}$$

According to Lyzenga's model, the water depth (d) depends linearly on the single predictor (X) derived from the image values at a given spectral band:

$$d = aX + b \tag{3.3}$$

The unknown parameters of the linear model (a, b) can be estimated by means of a simple regression between the values of single predictor (X) and in-situ depths (d). The deep-water correction accounts for the undesirable radiance components in order to isolate the signal upwelling from bottom. However, this correction approach would be subject to some uncertainties regarding the local/pixel based variations in inherent optical properties (IOPs) of the water column, water surface roughness and the atmospheric effects (Legleiter et al., 2009). In addition, the reflectance properties of the bottom material are not accounted for in the Lyzenga's single predictor which can suppress the robustness of the model. To deal with these problems, multiple regression is suggested to make use of all predictors derived from different spectral bands in order to enhance the robustness of the linear depth predictor model (Lyzenga 1985;

Lyzenga 2006). Equation 3.4 indicates the multiple regression of predictors derived from an *n*-band image with in-situ depths in order to establish a linear bathymetry model.

$$D = \sum_{i=1}^{n} a_i X_i + b \tag{3.4}$$

Stumpf et al. (2003) proposed to use a ratio model for depth retrievals to mitigate the undesirable effect of variations in bottom reflectance (Equation 3.5). Their model relies on the fact that different substrates at the same depth have approximately equal values of the ratio between total radiances at two different wavelengths.

$$X = \ln\left[\frac{L_T(\lambda_1)}{L_T(\lambda_2)}\right] \tag{3.5}$$

Such a ratio can be used as a single and to some extent robust depth predictor with respect to substrate variability (Stumpf et al., 2003; Flener, 2013). Legleiter et al. (2009) extended the idea of ratio model in the form of optimal band ratio analysis (OBRA) in order to choose the optimal pair of bands for which the ratio predictor provides the highest correlation with depths. The OBRA examines all the possible pair of bands through the ratio model to identify the optimal pair by comparing the coefficient of determination of the regression model.

The bathymetric models known in literature are originally developed for coastal environments and they are just recently being translated to the fluvial systems particularly using HRSI (Legleiter and Overstreet, 2012). The key distinctive feature of the riverine environments would be the thinner water column compared to the coastal settings. Therefore, a relatively high contribution from river substrate and a relatively low contribution from the water column can be expected particularly for shallow and clearly flowing streams. Although this is a promising point for depth retrievals due to having strong desired signal (i.e. bottom radiance), the pronounced effect of the substrate variability can make the depth retrieval complicated. Note that the deep-water correction required for Lyzenga's model demonstrated to be negligible for shallow rivers (Mumby and Edwards, 2000; Flener et al., 2012; Flener, 2013). This is mainly because the bottom signal is the dominant component of radiance reaching to the sensor particularly for the atmospherically corrected imagery. Therefore, it is less likely to approach to the deep-water signal in shallow and clear rivers (Legleiter et al., 2009).

3.3 Multiple Optimal Depth Predictors Analysis (MODPA)

The existing bathymetric models individually employ single/multiple Lyzenga predictors or a single ratio predictor. Although OBRA identifies the optimal ratio predictor, the model is based on a sole ratio predictor. The selection between predictor types (Lyzenga or ratio) can be challenging in practice as the results of previous studies indicate that each type of predictors can possibly lead to more accurate results than the other depending on the case study. For instance, Jawak and Luis (2016) reported that the Lyzenga model derived the bathymetry of a shallow lake more precisely (with 15% higher R^2 and 0.98 m lower RMSE) than the ratio model using WV-2 imagery. On the other hand, the regression type (simple or multiple) defines the number of predictors in the linear regression model. The bathymetry models relied on simple regression (e.g. OBRA) explain the dependent variable (i.e. depth) by only one predictor where other informative predictors can potentially be neglected.

This research aims at extending the initial depth predictors by considering all of the possible Lyzenga and ratio predictors rather than relying upon one of predictor types. In addition, some extra predictors can be considered from the RGB to HSI color space transformation. In this regard, the intensity component of the HSI space is added to the original image feature space and the associated Lyzenga and ratio predictors are included in the predictors. Note that the color space transformation can be applied to each combination of three spectral bands so that several intensity bands can be added to the feature space (e.g. four intensity bands can be derived for a 4-band GeoEye image). A multiple regression approach is then considered to keep most of the variability of predictors. However, making use of all the predictors may lead to over-parameterization of the model due to possibility of high correlation among the predictors. For example, 36 initial predictors can be derived from 8-band WV-2 imagery (8 Lyzenga predictors and 28 ratio predictors) while this number can be even increased by considering extra predictors. Therefore, performing a dimensionality reduction on all the possible predictors is necessary. This study suggests to select the optimal predictors by using three different regression methods of partial least square (PLS), stepwise and principal component (PC). The resultant optimal predictors can then be a combination of Lyzenga, ratio and the extra predictors.

Stepwise regression is a systematic method for adding and removing terms (predictors) from a linear model based on their statistical significance in explaining the response variable. The stepwise regression uses the p-value of an F-statistic to test models with and without a potential term at each step. PC and PLS are both regression methods that construct new predictors called components as linear combination of the original predictors. Then a subset of components can be selected as optimal predictors in such a way to keep most of the variability of the original predictors. The number of components can be chosen by looking at the percent of variance explained in the response variable as a function of the number of components. However, PC creates the components without considering the response variable (i.e. depth) while PLS takes the response variable into account (Haenlein, M., Kaplan, A.M., 2004; Matlab, 2016). These methods provide powerful modeling tools to deal with large number of predictors when the collinearity among the variables is strong (Abdi, 2003; Li et al., 2014).

The proposed bathymetry model, MODPA, selects the optimal (statistically significant) depth predictors from all the possible Lyzenga and ratio predictors as well as extra predictors derived from the color space transformation. Once the linear model is created, it can be used to predict the bathymetry of all image pixels within the river channel. The proposed method is validated and compared with Lyzenga's model and OBRA using independent known/in-situ check points.

3.4 Theoretical Calibration of Bathymetric Models

The calibration is critical for all of discussed bathymetric models to form linear relation between image derived values (X) and water depths (d). Empirical calibration is the widely used approach for estimation of unknown parameters of the linear relation (i.e. a and b). In this regard, field measurements of water depths are required for a limited number of points inside the river channel. Unknown parameters of the linear model can be then estimated by assigning the corresponding image values to the measured depths. However, this calibration approach is subject to couple of limitations and drawbacks (Fonstad and Marcus, 2005; Legleiter et al., 2009):

- Field measurements are usually time and cost consuming.

- Field surveys are needed to be carried out as simultaneous as possible with the imaging time that hinders the applicability of empirical methods for inaccessible rivers. Moreover, the usage of archive imagery would be limited only to the scenes with available in-situ data.
- Precise coregistration of field data and imagery is critical to preserve the accuracy of calibration. As coregistration of points inside the river is very challenging either by visual interpretation or using automatic matching techniques, few ground control points outside the channel are required for coregistration. Accurate positioning devices (e.g. RTK GPS) should be used for collection of field data.
- The usage of advanced tools of depth measurement (e.g. sonar devices) is limited in shallow rivers. Common measurement tools such as graduated poles provide point-wise depth information while an image value is corresponding to a pixel location (a few square meters for HRSI). Therefore, the number and horizontal distance of sampling points should be sufficient regarding the spatial resolution of imagery.

Regarding the inescapable limitations of empirical approach for calibration of bathymetry models, theoretical approaches have recently received attention. In this way, some researches (Legleiter, 2015; Fonstad and Marcus, 2005;) have tried to integrate the principles of open channel flow in calibration of the bathymetric models. In this study, Hydraulically Assisted Bathymetry (HAB) model developed by Fonstad and Marcus (2005) is investigated for theoretical calibration of bathymetry models and a simple modification is applied to the original model.

The HAB model starts with flow resistance equation of Manning (Equation 3.6) to estimate the mean water depth in a cross-section.

$$V = R^{2/3} S^{1/2} / n \tag{3.6}$$

where V denotes the cross-sectional average velocity. R is the hydraulic radius which can be replaced with the average depth ($\bar{d}$) and S represents the average energy gradient (channel slope) which can be extracted from digital elevation model or counter maps (Fonstad and Marcus, 2005). An estimation of n (hydraulic resistance) is required depending on the type of river.

Fonstad and Marcus (2005) have used Jarrett's (1984) equation to estimate *n* for mountain streams which is also used in this study (Equation 3.7).

$$n = 0.32 S^{0.38} R^{-0.16} \tag{3.7}$$

Combining the Manning's equation with the basic formula of discharge (Equation 3.8), mean depth for the i^{th} cross-section ($\bar{d}_i$) can be estimated which is a function of width (W_i), slope (S) and the discharge (Q):

$$Q = AV = W_i \bar{d}_i \bar{V}_i \tag{3.8}$$

$$Q = W_i \bar{d}_i^{1.83} S^{0.12} / 0.32$$
$$\bar{d}_i = (Q / 3.12 W_i S^{0.12})^{0.55} \tag{3.9}$$

In addition, HAB model approximates the maximum depth of each cross-section ($d^{\max}_i$) based on Robison and Beschta's (1989) assumption (Equation 3.10). Also minimum depth ($d^{\min}_i$) is considered as a small value (e.g. 5 cm).

$$d^{\max}_i = 2\bar{d}_i \tag{3.10}$$

Following the estimation of average, maximum and minimum depth for a cross-section, they can be linked to the average, maximum and minimum image values (X) of that cross-section in order to estimate the calibration parameters. However, HAB model considers some assumptions about minimum and maximum depth in each cross-section. More specifically, considering a small value (e.g. 5 cm) for minimum depth and finding the corresponding image value may lead to significant uncertainties. This is because image value of minimum depth is usually influenced with the surrounding land covers due to mixed pixels problem particularly in the river boundary. To deal with this problem, this research proposes a modification of HAB model. In this regard, the assumption on minimum depth (i.e. 5 cm) is suggested to be removed. Mean and max depths are estimated for multiple cross-sections based on the same models described for HAB model. Then the unknown parameters of the model are estimated based on least square estimation with high degree of freedom considering a sufficient number of cross-sections.

3.5 Dataset

The effectiveness of MODPA compared to the Lyzenga's model and OBRA is examined using three different approaches and a wide range of analysis: (a) spectroscopic experiments are performed at a hydraulic laboratory to acquire controlled measurements of spectral and bathymetric data. As substrate variability would be the key challenge for bathymetry retrieval in shallow and clearly flowing streams, robustness of the models is examined considering two bottom types for the experiments. Suspended sediment is considered as the main parameter defining the water column properties due to the fact that sediment load is the primary control on IOPs of clear rivers (Legleiter and Overstreet, 2012; Legleiter et al., 2016). The details of spectroscopic experiments are described in section 3.4.1; (b) radiative transfer modeling is used to produce synthetic data representative for most of alpine rivers in Italy (e.g. Sarca River). The ranges of IOPs used for simulations are associated with long-term (some decades) field observations of the parameters reported by environmental agencies (Giardino et al., 2007). This provides the possibility of analyzing the performance of depth retrieval methods also in extreme conditions of IOPs (relatively turbid waters) in the study area (see Section 3.4.2 for more details); (c) WV-2 image is used to map the bathymetry of Sarca River from space. In-situ depths are gathered using a RTK GPS to calibrate and assess the models (see Section 3.4.3). Moreover, the surface reflectance product of DigitalGlobe (i.e. AComp) is examined for the first time for the bathymetry of rivers using WV-2 imagery. In this regard, the accuracies of bathymetry retrievals are compared for top of atmosphere (TOA) and AComp reflectances.

3.5.1 Laboratory Measurements

Spectroscopic measurements are performed on a water flume as part of facilities available at hydraulic laboratory of University of Trento. Hydraulic flumes are widely used for simulation and investigation of flow field in riverine systems. However, to our knowledge, this is the first time that spectroscopic and hydraulic measurements are integrated in an indoor laboratory environment particularly for characterizing bathymetry and bottom properties from spectral data.

A set of spectral measurements is performed to test bathymetry models under controlled conditions of illumination, water level, IOPs and bottom properties. Two water flumes with different bottom properties are used to examine depth retrieval from spectral measurements. Flume-1 is an 18 m long, 1 m wide and 0.7 m high channel and its bottom is covered by a layer of uniform fine sand. Flume-2 is a 6 m long, 0.4 m wide, and up to 0.4 m deep with a gravel bed composed of semi-natural material. The substrate of flume-2 characterized by natural sands in the background combined with larger (3 cm diameter) ball-shape gravels with plastic material. The channels are equipped with flowmeter to measure the discharge and an adjustable tailgate weir located at the end of flume to ensure a uniform flow condition and to control the water level. Experiments are focused on a spot in the longitudinal and cross-sectional middle of each channel to ensure a well-developed flow and also to mitigate as much as possible the reflections and shadows from the sides. The water depths are measured using a point-gage along the test spot. The spectra are collected by installing a fiber optic jumper cable over the test spot connected to an Analytical Spectral Devices (ASD) HandHeld 2 spectroradiometer in the 325–1075 nm spectral range with 1 nm resolution. The unstable sources of lights from surrounding environment are eliminated by covering the experiment spot on the flume-1 while the flume-2 is entirely located in a darkroom. A standard ASD illuminator is used to produce highly stable light across the full visible/NIR spectral range (350 – 2500 nm). The illumination geometry is modified in such a way to remove the self-shadings of the instrument over the flume (Gordon and Ding, 1992). The spectra are collected over the two flumes by changing the water level with one cm increments. Three spectra are recorded for each flow condition that each of which is an average of 25 individual samples. Dark current and white reference measurements are taken and updated for each spectral recording in order to calibrate the spectra into the reflectances. The spectra observed over two flumes are supplied to the bathymetry models to investigate their robustness mainly with respect to substrate variability. Also a little degree of water column heterogeneity can be assumed which is imposed by slightly different suspended sediment concentrations of two flumes. Figure 3.1 shows the experiments setup over the two flumes.

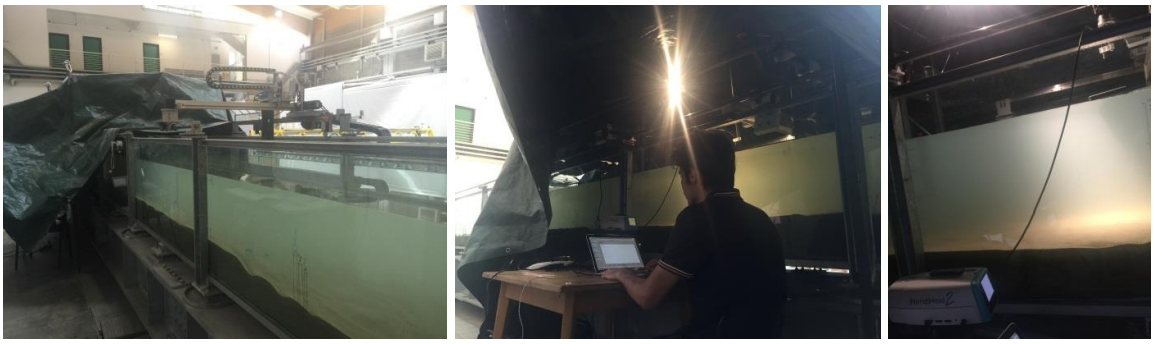

(a) Flume-1

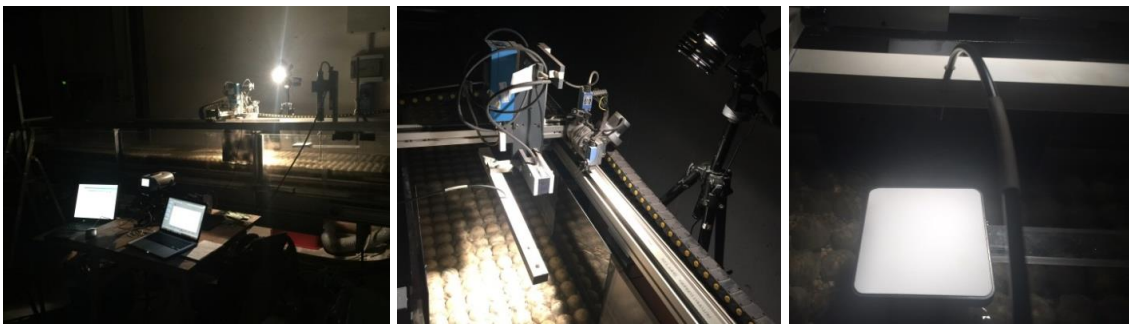

(a) Flume-2

Figure 3.1 Spectroscopic experiments in a range of water depths on (a) flume-1 with a sand bed and (b) flume-2 with a gravel bed composed of semi-natural material.

3.5.2 Synthetic Data

Radiative transfer modeling provides a unique means of understanding the interactions of light through its traveling path from atmosphere reaching to water surface, water column and the bottom and then upwelling back to the sensor (Mobley, 1994). This type of simulations is previously used in few researches to elaborate the efficiency of OBRA with isolating the effect of substrate type as well as TSS concentration in shallow rivers (Legleiter et al., 2009; Legleiter and Roberts, 2009). This research benefits from simulations using Hydrolight radiative transfer modeling (Mobley and Sundman, 2008) to examine the proposed MODPA compared to the other bathymetry models by isolating the effect of IOPs including Chl-a, TSS and CDOM. Although the main focus of this study is on clearly flowing streams, the simulations are considered in a wider range of IOPs to be representative for extreme conditions for the rivers of interest. A long-term (some decades) in-situ measurements of water quality parameters reported by environmental agencies are considered to define the range of IOPs for alpine rivers in Italy which can be

characteristic for similar rivers as well. The effect of each IOP is isolated by considering constant values for the other IOPs (Table 3.1). Note that a dolomite bottom type is considered for these simulations and the water depth varies from 2 cm to 2 m with 2 cm intervals. The CDOM absorption at 440 nm (aCDOM @ 440 nm) is chosen to quantify the concentrations of this IOP (Kirk, 1996).

Table 3.1 The range of IOPs considered for radiative transfer modeling. In each simulation scenario, the effect of variations in one of IOPs is isolated by considering constant values for the other IOPs.

Isolated IOP (variable)	Other IOPs (constant)
Chl-a (mg/m^3) = {1, 3, 5}	TSS= 3 g/m^3, CDOM= 0.22 m^{-1}
TSS (g/m^3) = {0, 3, 6}	Chl-a= 3 mg/m^3, CDOM= 0.22 m^{-1}
aCDOM@ 440 nm (m^{-1}) = {0.07, 0.22, 0.36}	Chl-a= 3 mg/m^3, TSS= 3 g/m^3

In addition, an optically complex condition is also considered to explore the effectiveness of bathymetry models by assuming all the IOPs as variable parameters and also considering variable bottom types. The range of IOPs and water depths are as same as previous simulations and three different bottom types are considered including sediment, macrophyte and dolomite.

3.5.3 HRSI and In-Situ Measurements

HRSI including an 8-band WV-2 image and its convolution to the 4-band GeoEye image are used to map the bathymetry of Sarca River located in northeast Italy. It is a mountain-piedmont gravel bed river flowing from the Adamello glaciers down to the Garda lake. Sarca is a shallow (depth < 1 m), narrow (mean width < 30 m) and clearly flowing stream which is regulated by an upstream dam that retains the water level very consistent during a long period over several years. A WV-2 image is used for which both TOA and AComp reflectances are available. Moreover, convolution of WV-2 to GeoEye bands is used to gain more insights into the additional spectral bands of the WV-2 imagery with respect to traditional 4-band (RGB-NIR) HRSI in terms of mapping river bathymetry. The WV-2 sensor provides four additional bands located at coastal blue (400-450 nm), yellow (585-625 nm), red-edge (705-745 nm) and long-wavelength NIR (860-1040 nm) which are denoted respectively as CB, Y, RE and NIR-2 hereafter.

The field survey is carried out in three reaches well-distributed along the river (Figure 3.2). The in-situ depths are recorded with precise coordinates using a RTK GPS at dense points along cross-

sections (Figure 3.3). An ordinary kriging is used to interpolate the measured depths at the pixel level that enables a pixel-to-pixel comparison of in-situ depths with the image-derived estimates (Legleiter and Overstreet, 2012). One-half of the data is used for calibration of models and the remaining half as check-points for accuracy assessment.

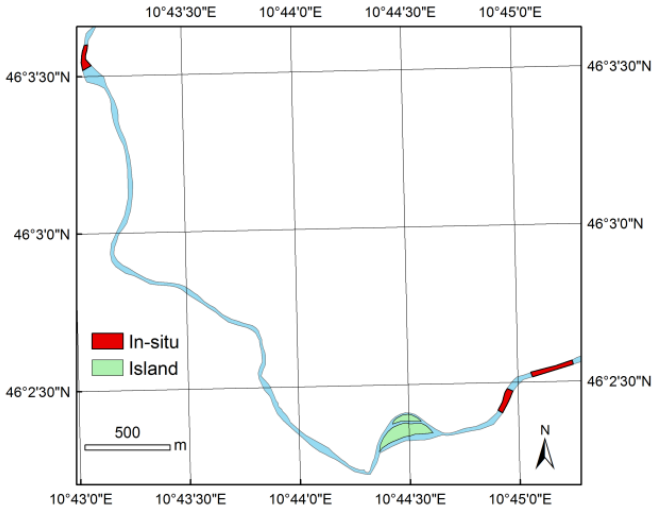

Figure 3.2 In-situ reaches surveyed for calibration and validation of the bathymetry models in Sarca River.

Figure 3.3 In-situ measurements of water depths in Sarca River using a RTK GPS along the cross-sections.

3.6 Results

The bathymetry models are applied to spectroscopic data collected in the laboratory, synthetic data from radiative transfer modeling and HRSI. Findings are presented and discussed in the following sections.

3.6.1 Laboratory Experiments

The spectra observed over the two flumes are convolved with spectral responses of WV-2 and GeoEye sensors. The parameters of the bathymetric models are then estimated using random half of the spectra observed over both flumes to get insights into the robustness of models with respect to substrate variations between the flumes. The depth retrieval models are validated using second half of the spectra and associated bathymetry information as of independent check points. Figure 3.4 shows predicted vs. observed depths as well as the residuals of the predicted depths based on discussed bathymetry models applied on the laboratory spectra convolved to WV-2 bands.

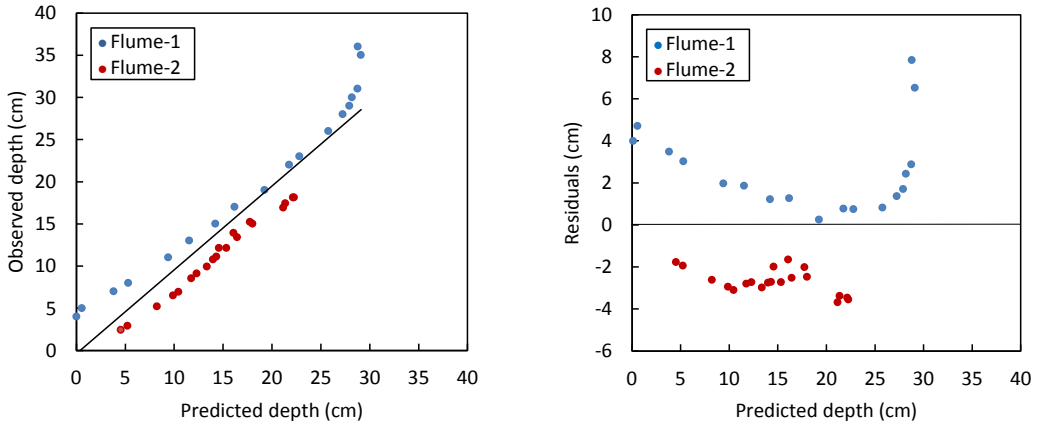

(a) Single Lyzenga predictor derived from NIR-1 band

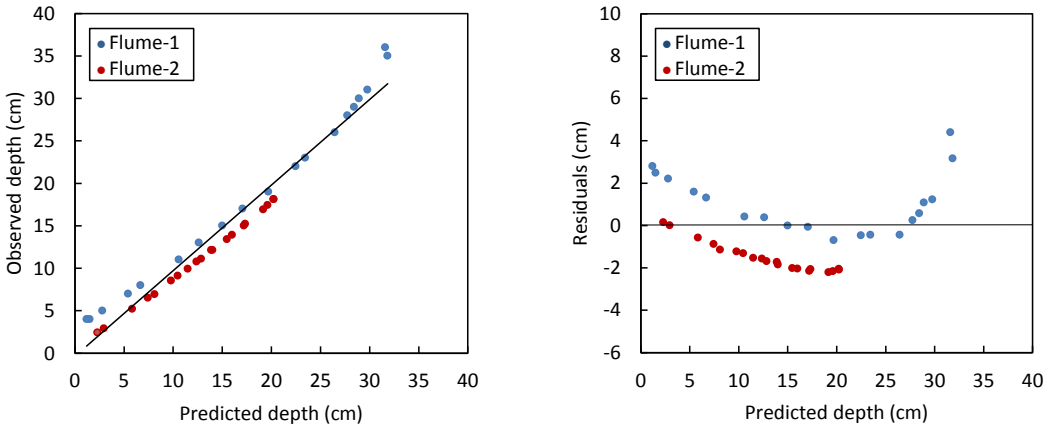

(b) OBRA identified Y/RE ratio as optimal predictor

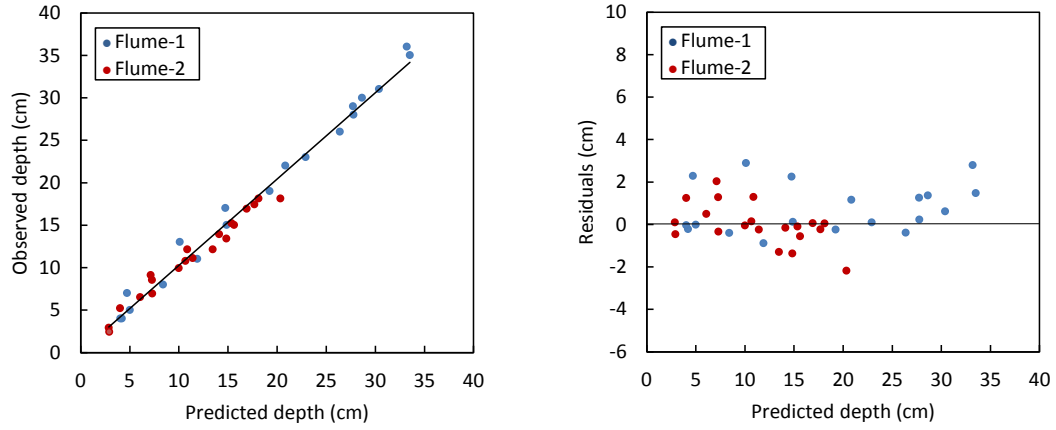

(c) Multiple Lyzenga

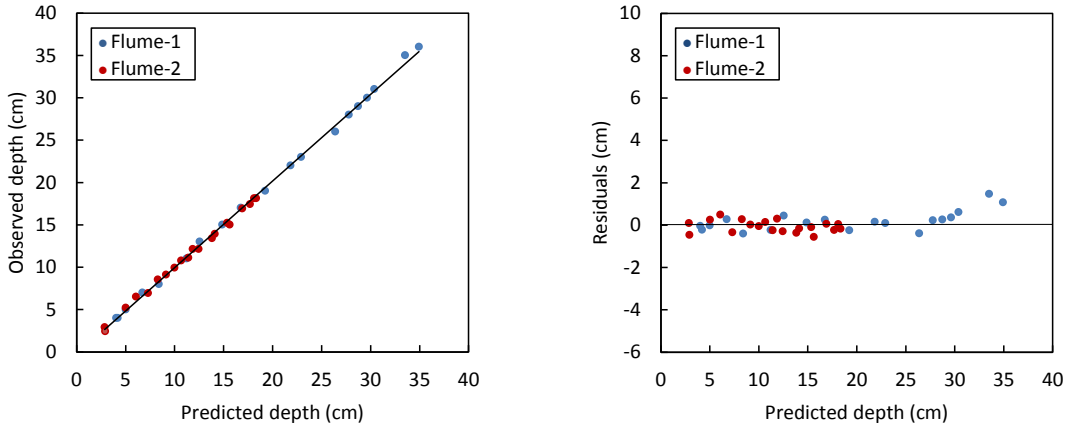

(d) MODPA

Figure 3.4 Validation of depth retrieval from laboratory spectra convolved to the WV-2 bands based on (a) single Lyzenga predictor, (b) OBRA, (c) multiple Lyzenga predictors and (d) MODPA based on PLS regression.

In Figure 4, the validation of single Lyzenga predictor is presented for the NIR-1 band that yielded the strongest linear relation among the other bands. OBRA matrix is illustrated in Figure 3.5 which shows the R^2 and RMSE of the ratio model for all the possible combination of spectral bands where the highest regression R^2 occurred for the ratio between the yellow and the red-edge bands (Y/RE).

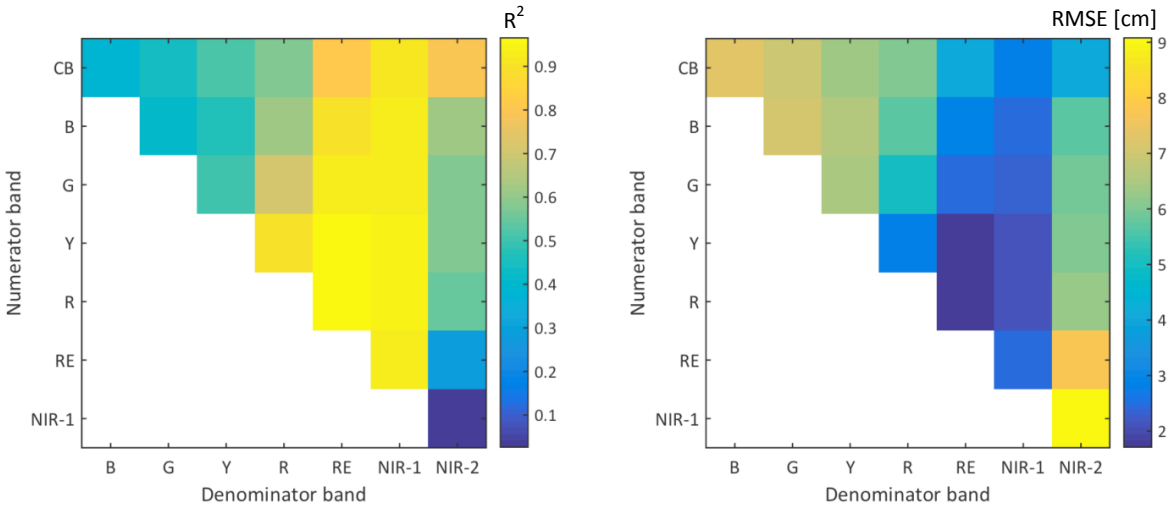

Figure 3.5 Optimal band ratio analysis (OBRA) of laboratory spectra convolved to the WV-2 bands representing R^2 and RMSE of the ratio bathymetry model for all the possible combination of spectral bands.

As illustrated in Figure 3.4, the residuals from Lyzenga single predictor can be clearly distinguished into two separate patterns that indicate the high sensitivity of this model to the substrate types of the two flumes. This would be interpreted as relatively bright substrate of the flume-1 which is confused with shallower depths while the darker bottom type of the flume-2 caused to an overestimation of depths. The OBRA shows some improvements but still suffering from the same drawback. Multiple Lyzenga model and MODPA are both robust with respect to substrate variability. However, the residuals from MODPA are lower than those of multiple Lyzenga (0.35 cm and 1.2 cm RMSEs, respectively).

The accuracy statistics of bathymetry models with and without extra predictors derived from the intensity component of the HSI color space are compared for the laboratory spectra convolved to both WV-2 and GeoEye bands (Figure 3.6). The three different regression approaches (i.e. PLS, stepwise and PC) provided high accuracies through the proposed MODPA. However, MODPA based on PLS regression is slightly more accurate than others, which is composed of one Lyzenga predictor derived from RE band and three ratio predictors derived from G/NIR-1, Y/RE and R/RE ratios for the laboratory spectra convolved to the WV-2 bands. The extra predictors improve the accuracies of bathymetry retrievals. The improvements are more pronounced for the spectra convolved with lower number of bands (i.e 4-band GeoEye). It can be also inferred that the enhanced spectral resolution of WV-2 leads to more accurate depth retrievals than GeoEye.

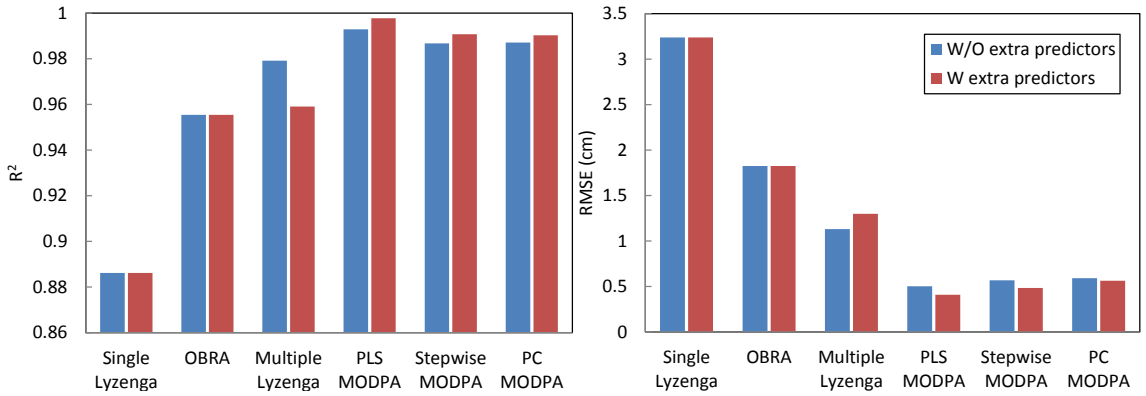

(a) Laboratory spectra convolved to WV-2 bands

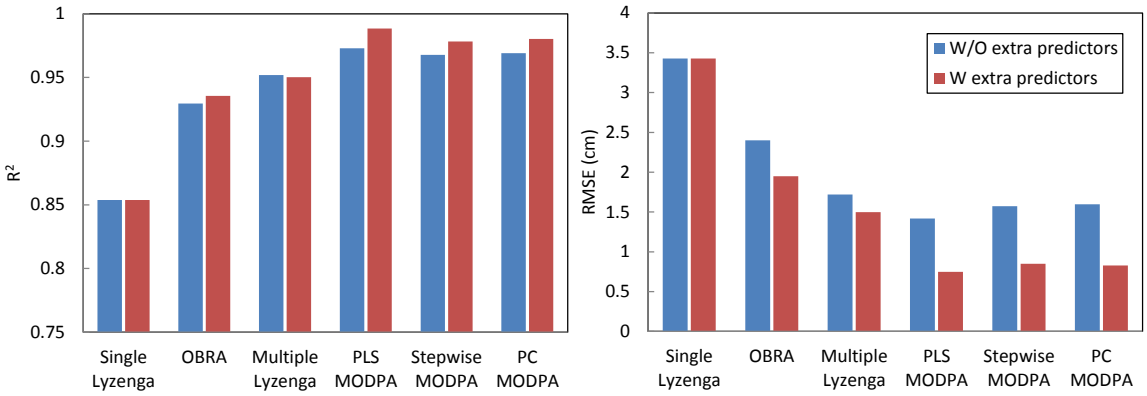

(b) Laboratory spectra convolved to GeoEye bands

Figure 3.6 Accuracy statistics (R^2 and RMSE) of bathymetry models with (W) and without (W/O) extra predictors applied on laboratory spectra convolved to match (a) WV-2 and (b) GeoEye bands.

3.6.2 Synthetic Data Analysis

The effect of each IOP including TSS, Chl-a and CDOM is explored on depth retrievals by changing the desired IOP and keeping the two other IOPs as constant parameters (see Table 1). Moreover, the performances of bathymetric models are evaluated regarding the optically complex testing scenario described in Section 3.4.2. Note that the bathymetry models are applied without extra predictors for isolating the effect of each IOP. This is because the MODPA yielded very high accuracies without extra predictors so that no further improvement was required. However, the depth retrievals are improved for the optically complex example by considering extra predictors (see Section 3.5.2.4).

3.6.2.1 Isolating the Effect of TSS

The effect of variations in TSS is evaluated on bathymetry of up to 2 m deep waters. Figure 3.7 indicates the match-up validations for different bathymetry models using independent check-points.

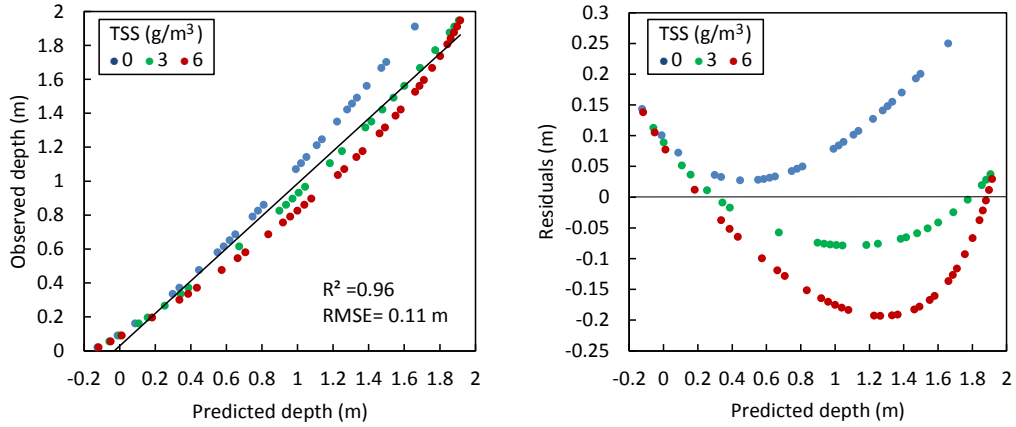

(a) Simple Lyzenga derived from R band

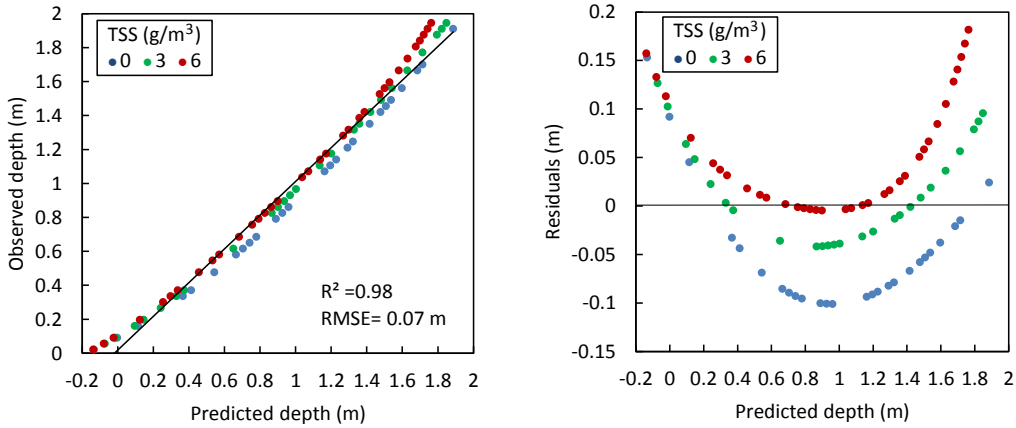

(b) OBRA identified B/Y ratio as optimal predictor

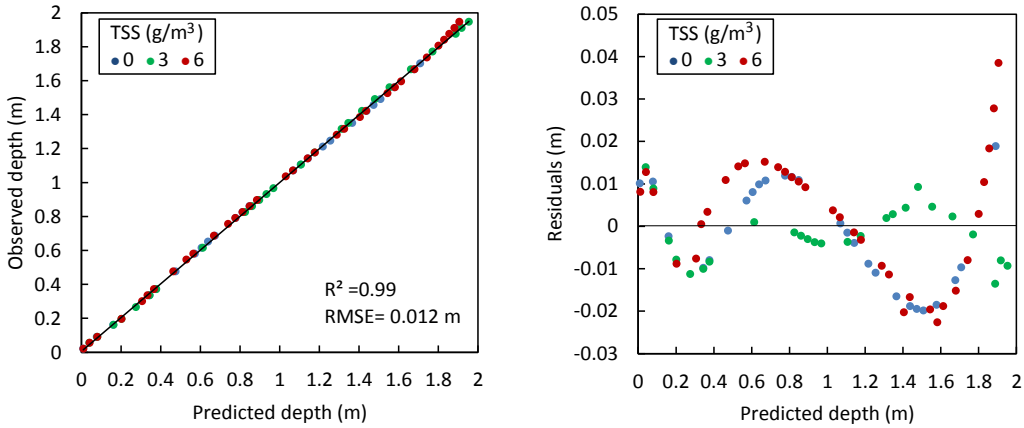

(c) Multiple Lyzenga

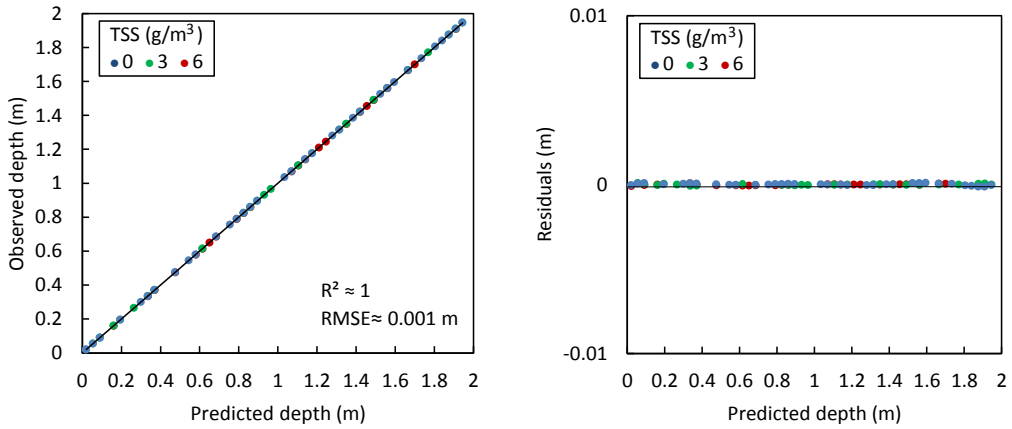

(d) MODPA

Figure 3.7 Match-up validation of depth retrievals by isolating the effect of TSS.

As evident in Figures 7a and 7b, simple Lyzenga's model and OBRA are sensitive to changes in TSS concentrations. The multiple Lyzenga model shows better performance though there are still some patterns in the residuals. The proposed MODPA yields a robust retrievals and with a very good match-up (RMSE of 1 mm).

3.6.2.2 Isolating the Effect of Chl-a

Figure 3.8 illustrates the match-up analysis for the bathymetry models by isolating the effect of Chl-a. The MODPA provides robust and perfect depth retrievals (Figure 3.8d).

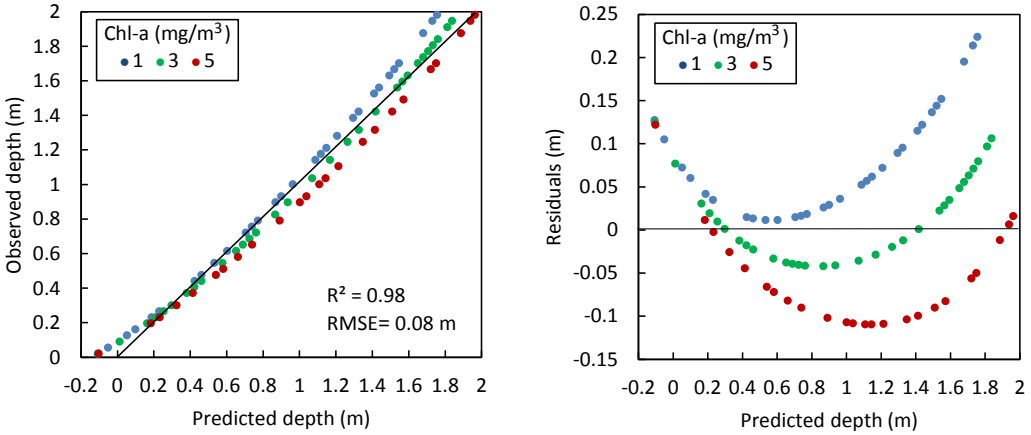

(a) Simple Lyzenga derived from R band

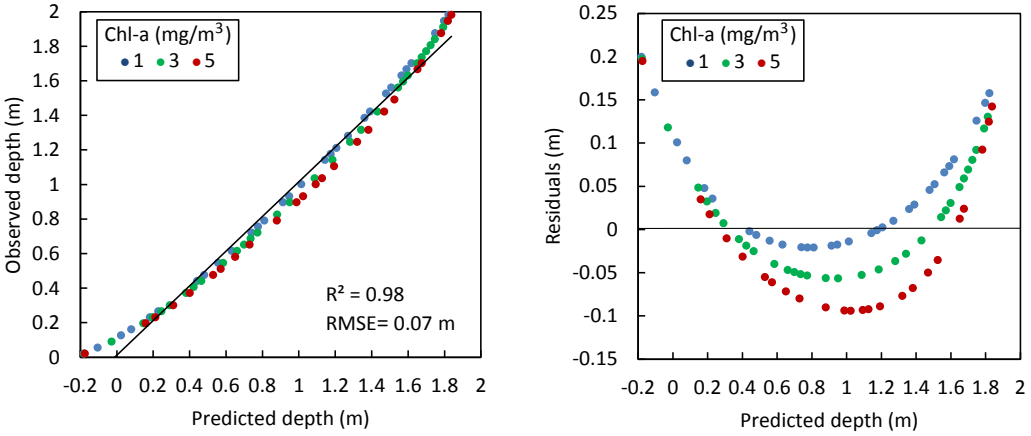

(b) OBRA identified Y/R ratio as optimal predictor.

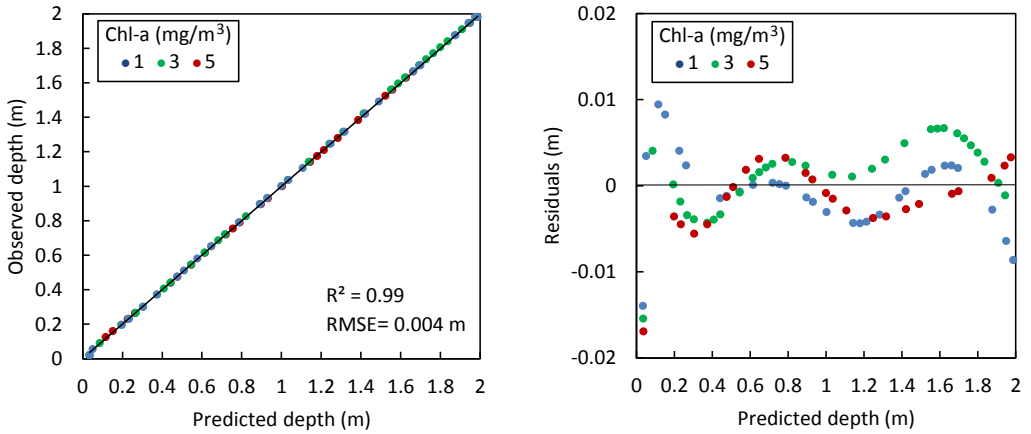

(c) Multiple Lyzenga

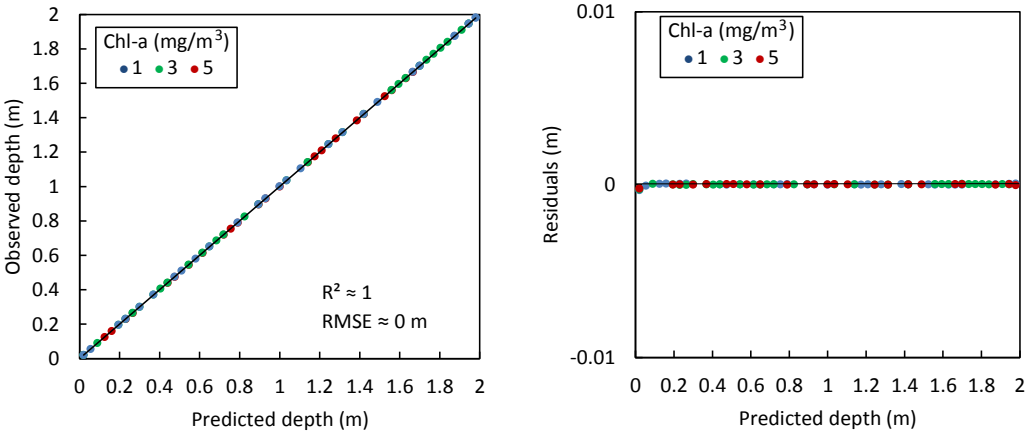

(d) MODPA

Figure 3.8 Match-up validation of depth retrievals by isolating the effect of Chl-a.

3.6.2.3 Isolating the Effect of CDOM

The results concerned with the effect of changes in CDOM indicate the better performance and robustness of the MODPA compared to the others (Figure 3.9).

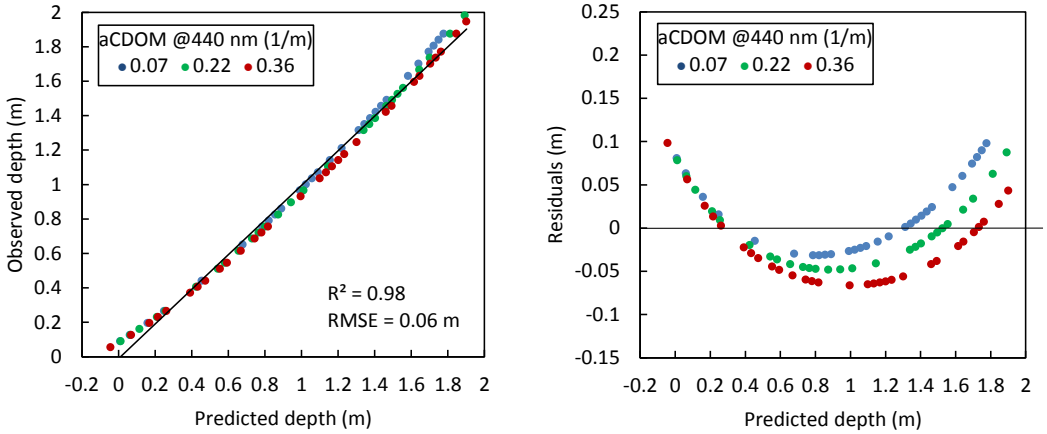

(a) Simple Lyzenga derived from R band

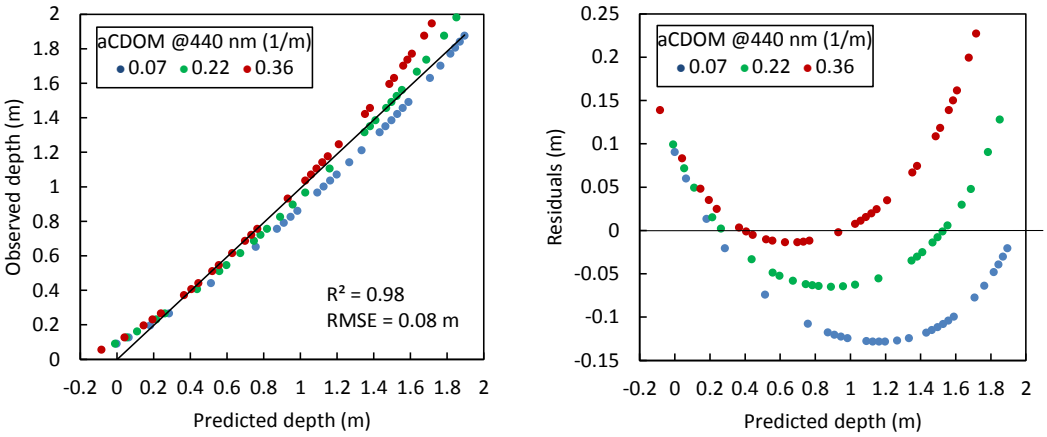

(b) OBRA identified Y/R ratio as optimal predictor

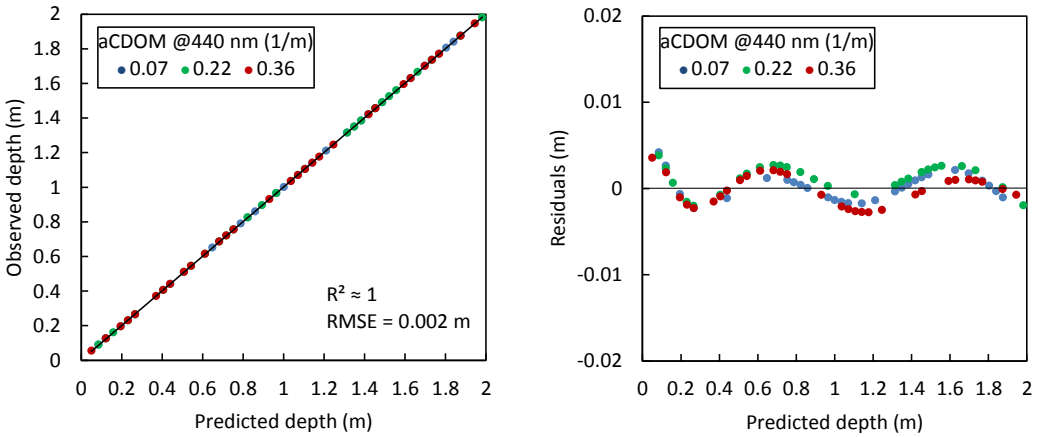

(c) Multiple Lyzenga

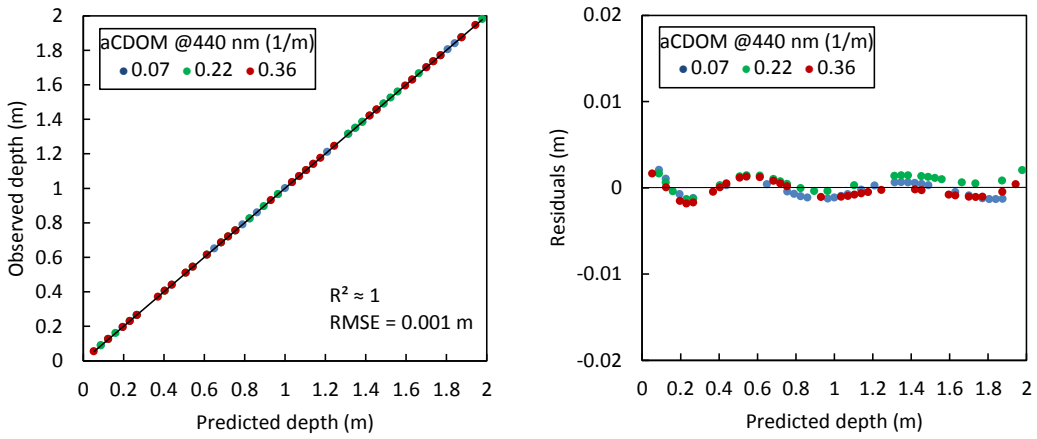

(d) MODPA

Figure 3.9 Match-up validation of depth retrievals by isolating the effect of CDOM.

3.6.2.4 The Optically Complex Example

To get more insights into performance of the bathymetry models, a set of simulated spectra representative of an optically complex river in the study area is taken into account. This testing strategy considers the bottom type and all IOPs as variable parameters (see Section 3.4.2). The vertical patterns on the graphs associated with simple Lyzenga model (Figure 10a) indicate saturation of the single band predictor for depths above ~1 m. Note that in this analysis, the NIR-1 band providing the highest correlation has been selected as the optimal single predictor which is highly affected by absorption of pure water. Therefore, the saturation for relatively deep waters could be expected using this spectral band. Figure 3.10 shows the match-up validations where MODPA leads to the highest correlation with known depths (R^2 = 0.98 and RMSE= 6 cm without considering extra predictors). Including the extra predictors enhances further the depth retrievals using MODPA (RMSE= 3 cm, i.e. 3 cm further improvement). This demonstrates the effectiveness of extra predictors for improving the robustness of bathymetry models in optically complex waters.

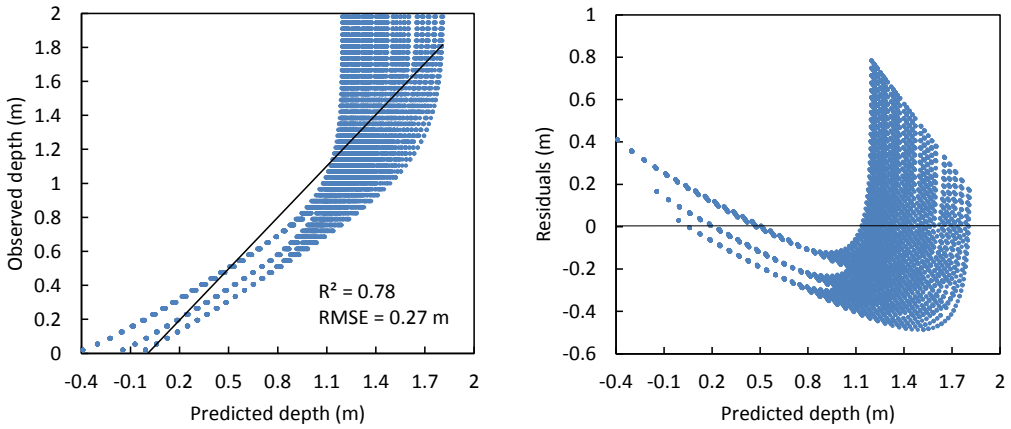

(a) Simple Lyzenga derived from NIR-1 band

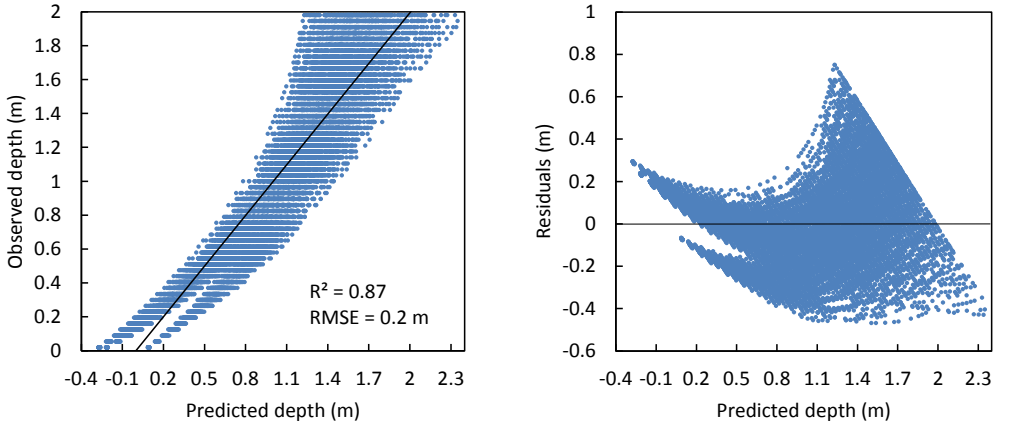

(b) OBRA identified G/R ratio as optimal predictor

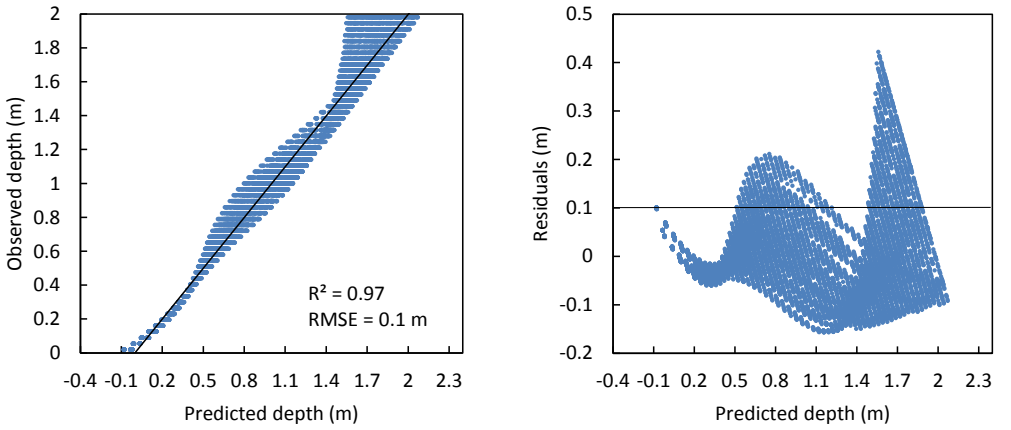

(c) Multiple Lyzenga

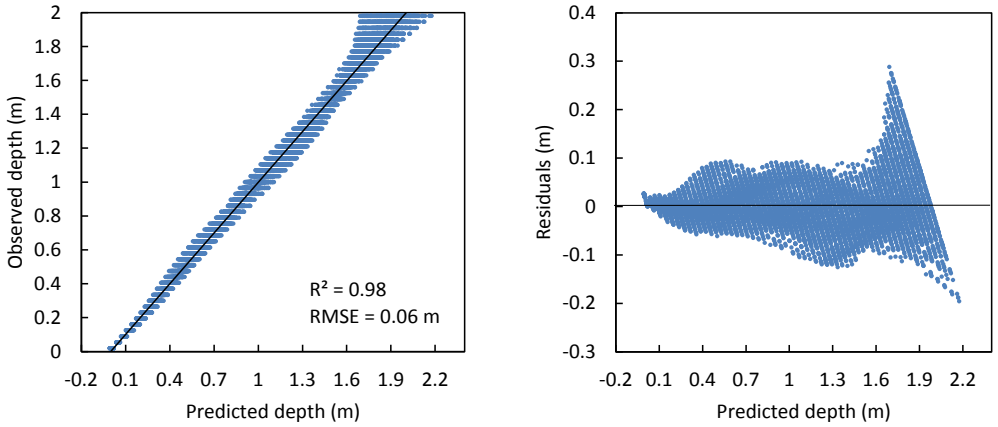

(d) MODPA

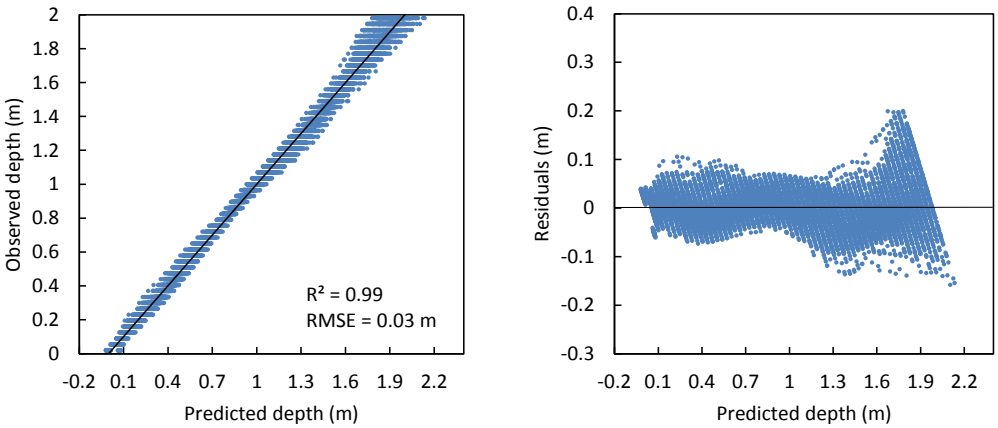

(e) MODPA with Extra predictors

Figure 3.10 Match-up validation of depth retrievals for optically complex spectra with variable IOPs and bottom types.

3.6.3 High Resolution Satellite Imagery

The atmospheric effects can contribute remarkably at TOA radiance due to low level of reflectivity from water bodies (Gordon, 1990; Pahlevan et al., 2017b). The AComp reflectances (i.e. surface reflectances) are compared with the TOA reflectances in a range of water depths along the Sarca River for the WV-2 image (Figure 3.11). For each water level, the average of image-derived reflectances is estimated for the pixels with the depth of interest known from the field survey. As evident in Figure 11, atmospheric effects are significant at short wavelengths where the Rayleigh scattering is dominant (Gordon 1990; Pahlevan et al., 2017b). The AComp spectra show a higher distinction among different water depths rather than those of TOA spectra. Moreover, a transition crossover can be identified between scattering- and absorption-dominated regions at around 550

nm. This is mainly because the suspended sediment is the primary control on the IOPs of the water column in clear-flowing rivers that cause to an increase in reflectance at short wavelengths by increasing the water depth (Legleiter et al., 2009; Legleiter et al., 2016). However, the spectra are dominated by absorption by pure water at long wavelengths where reflectance decreases with water depth. AComp and TOA reflectances of the WV-2 image are supplied to the bathymetry models to investigate the performance and robustness of the models with respect to the atmospheric effects.

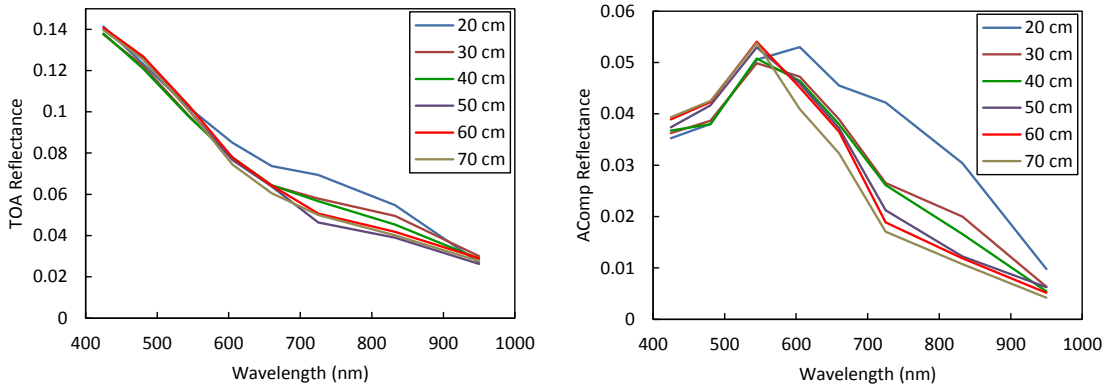

Figure 3.11 Comparison of AComp and TOA reflectances of WV-2 image in a range of water depths along the Sarca River.

According to the analysis performed on laboratory and simulated spectra, bathymetry model based on a single Lyzenga predictor is highly dependent to the substrate and IOP variability. This model is then eliminated from the studied models for mapping the river bathymetry from HRSI. Figure 3.12 illustrates the validation of bathymetry models using the TOA reflectances of WV-2 image.

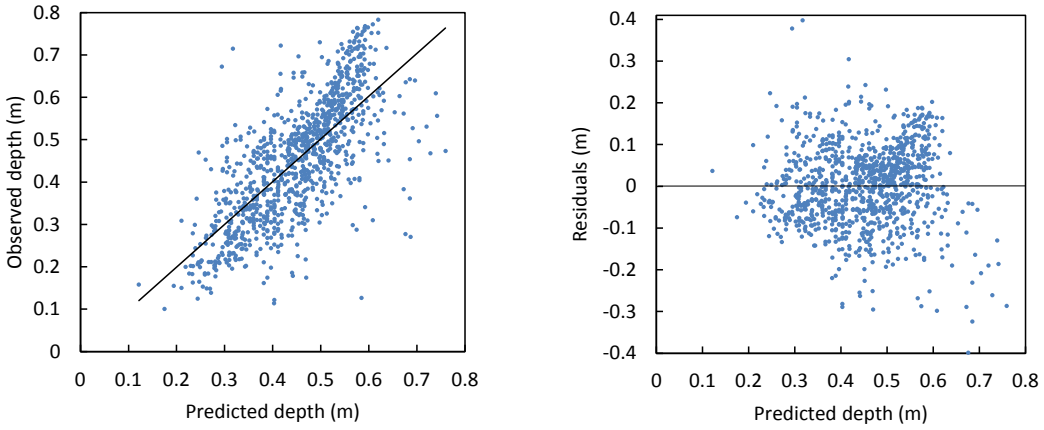

(a) OBRA

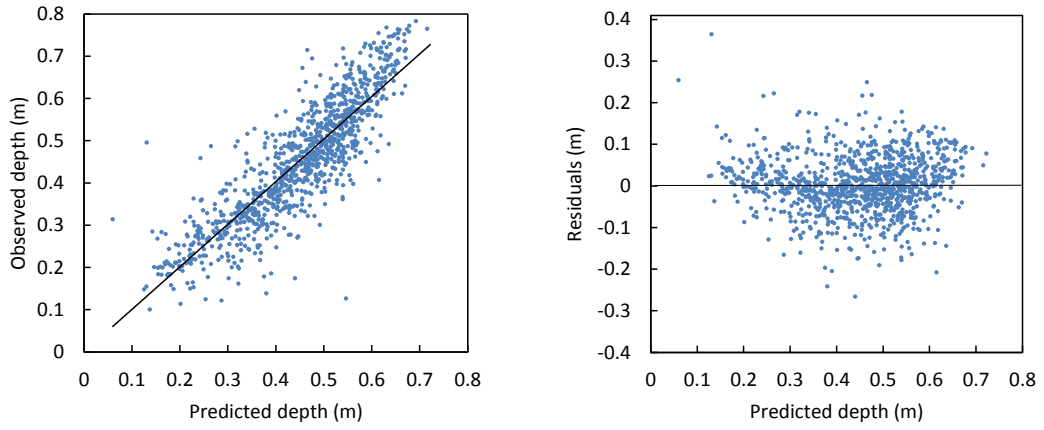

(b) Multiple Lyzenga

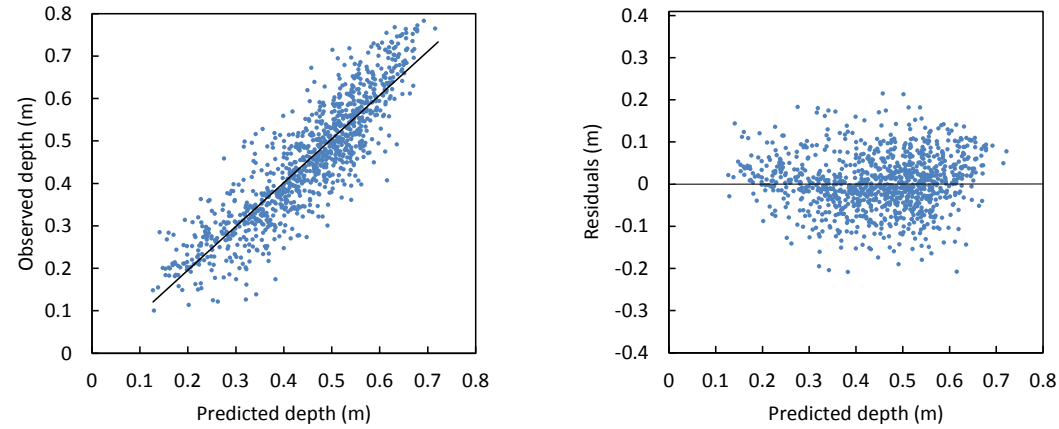

(c) MODPA

Figure 3.12 Validation of depth retrieval from TOA reflectances for WV-2 image based on (a) OBRA, (b) Multiple Lyzenga and (c) MODPA based on PLS regression.

Figure 3.13 represents the OBRA matrix obtained from TOA reflectances of WV-2 image for which G/R ratio yielded the highest observed vs. predicted R^2 (0.53) with an RMSE of 9 cm. The matrix

indicates that band ratios with a B or G numerator and a RE or NIR-1 denominator as well as Y/RE ratio also provide comparable results with the optimal band ratio (i.e. G/R). This demonstrates the potential of long wavelengths across the near-infrared spectrum in retrieving the bathymetry in shallow and clear waters as the water column depth and IOPs are not in a range to fully absorb the signal.

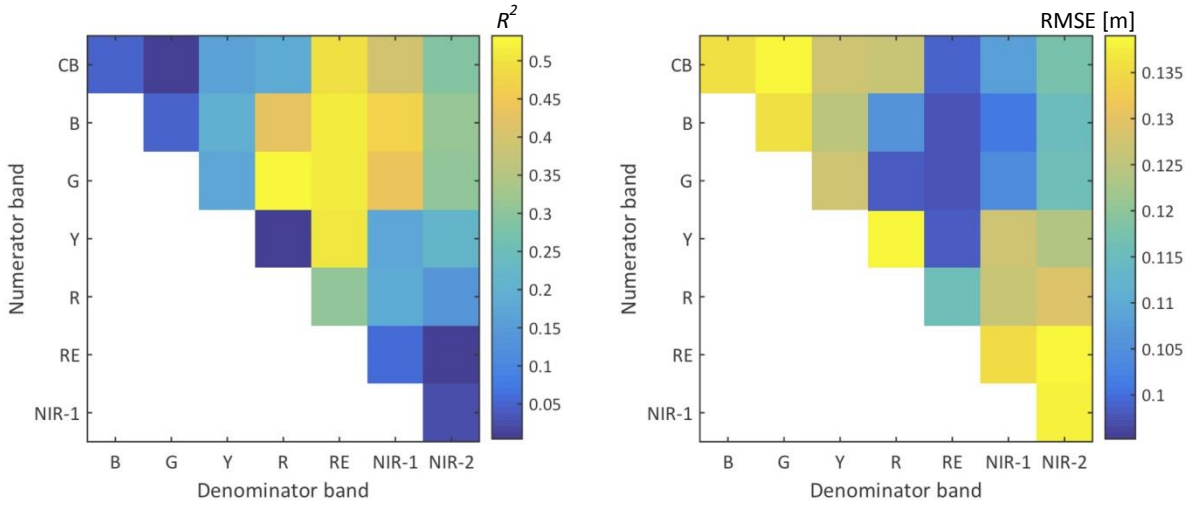

Figure 3.13 Optimal band ratio analysis (OBRA) of TOA reflectances for WV-2 image representing R^2 and RMSE of the ratio model for all the possible combination of spectral bands.

The bathymetry maps obtained from TOA reflectances of WV-2 image are compared with the in-situ depths along the three reaches (Figure 3.14).

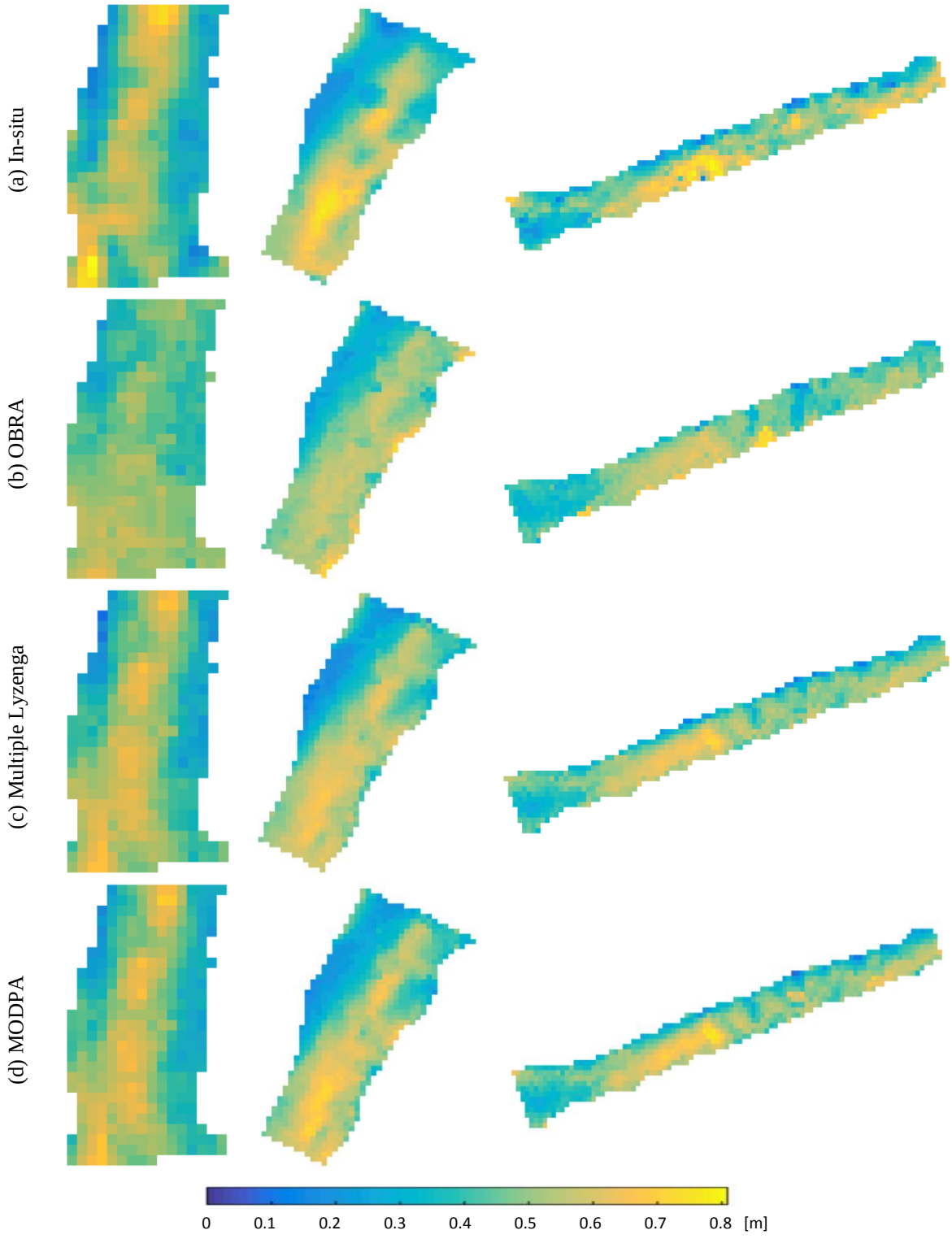

Figure 3.14 Comparison of (a) in-situ depths with bathymetry maps derived from (b) OBRA, (c) Multiple Lyzenga model and (d) MODPA.

The accuracy statistics of bathymetry models with and without extra predictors are compared for WV-2 image and its convolution to GeoEye bands. In addition, AComp reflectances are examined against the TOA reflectances using the WV-2 image (Figure 3.15). In general, the AComp reflectances yielded higher accuracies than TOA reflectances. However, the accuracy enhancement is more pronounced for OBRA while the MODPA is less affected by atmospheric effects. Again, the three approaches for selection of optimal predictors provided comparable results whereas the method based on PLS regression is to some extent more accurate than others. This model applied on WV-2 image is composed of three Lyzenga predictors derived from CB, G and RE bands and two ratio predictors derived from G/R and G/NIR-1 ratios.

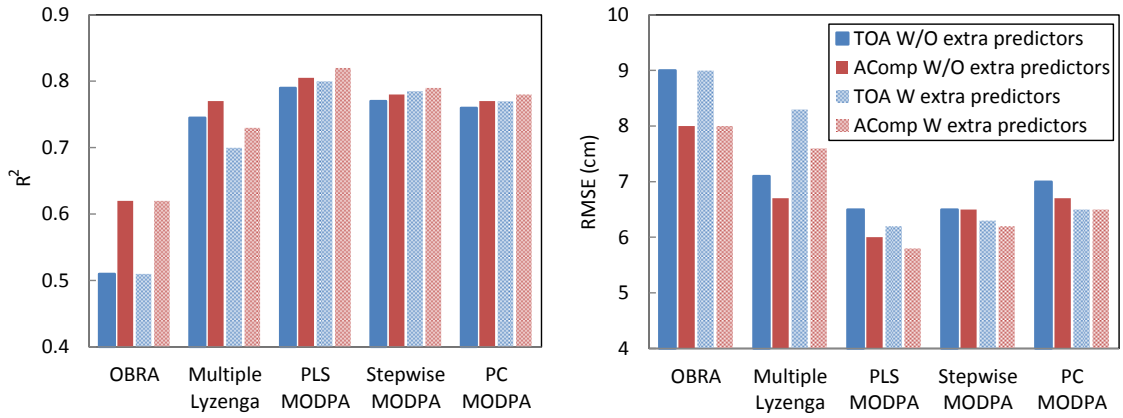

(a) WV-2 image

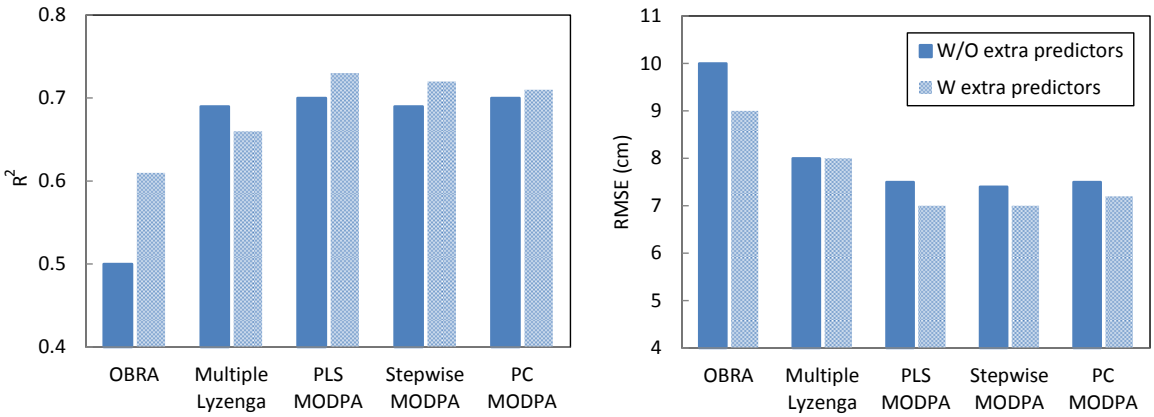

(b) GeoEye image

Figure 3.15 Accuracy statistics (R^2 and RMSE) of bathymetry models with (W) and without (W/O) extra predictors applied on (a) WV-2 and (b) GeoEye images. The comparison also performed for the TOA and AComp reflectances of the WV-2 image.

As it can be inferred from Figure 15, the extra predictors in general lead to an increase of R^2 for all the models except for the Lyzenga's multiple regression model. This is mainly because making use of all the Lyzenga predictors derived from RGB and HSI color spaces increase the chance of having correlated predictors and then over-parameterization problem. As an interesting point, extra predictors for the GeoEye image increase remarkably the accuracy of OBRA (about 0.1 enhancement of R^2). This is shown in Figure 3.16 where the optimal ratio model is derived from intensity (I) bands (extra predictors).

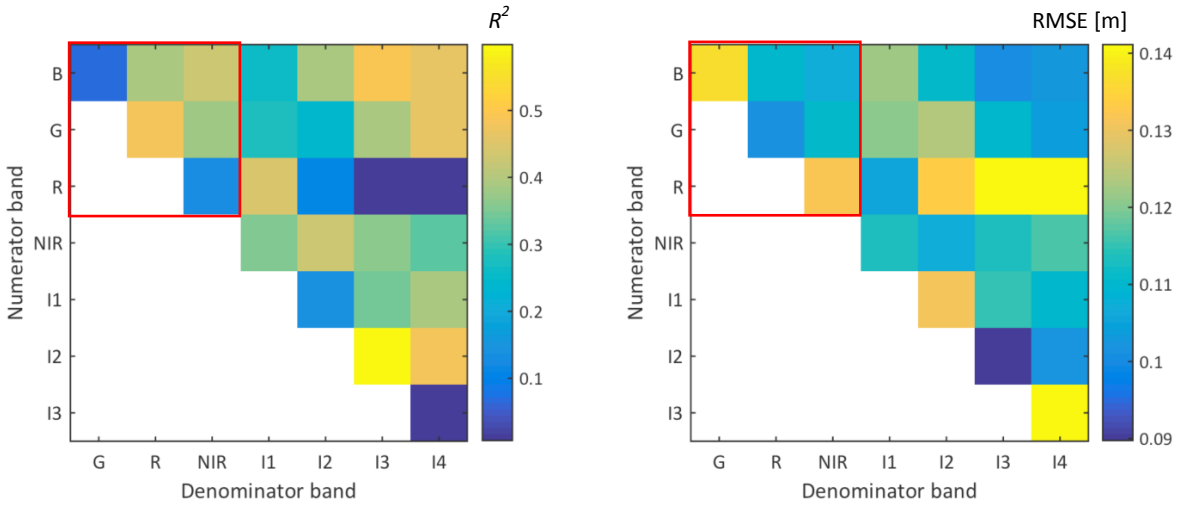

Figure 3.16 Optimal band ratio analysis (OBRA) of GeoEye image where the OBRA matrix derived from the original image bands (RGB color space) is highlighted with a red box. The optimal band ratio model is derived from extra predictors.

Figure 3.17 illustrates the bathymetry retrievals along some randomly selected cross-sections compared to the in-situ depths using WV-2 image.

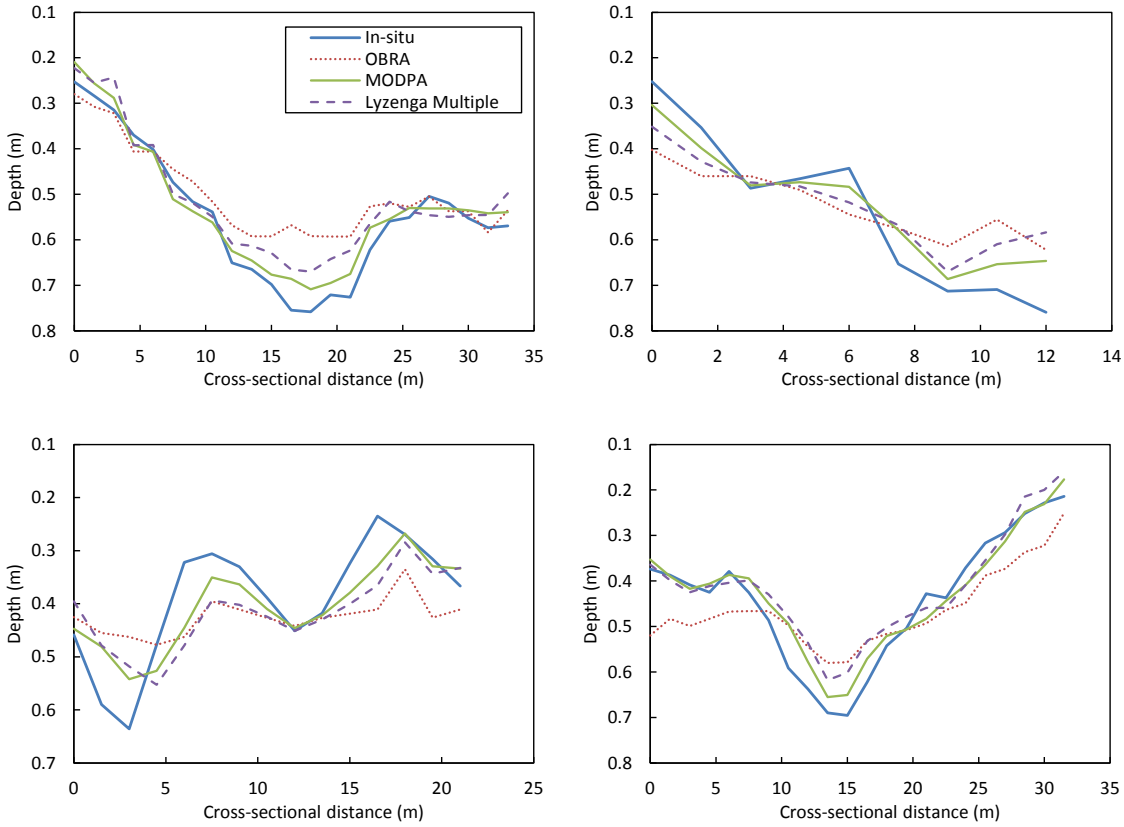

Figure 3.17 Comparing the results of bathymetry models considering extra predictors with field observations along a cross-section of Sarca River using WV-2 image.

Figure 3.18 illustrates the bathymetry map retrieved from WV-2 image for about five km long reach using the proposed MODPA and based on PLS regression.

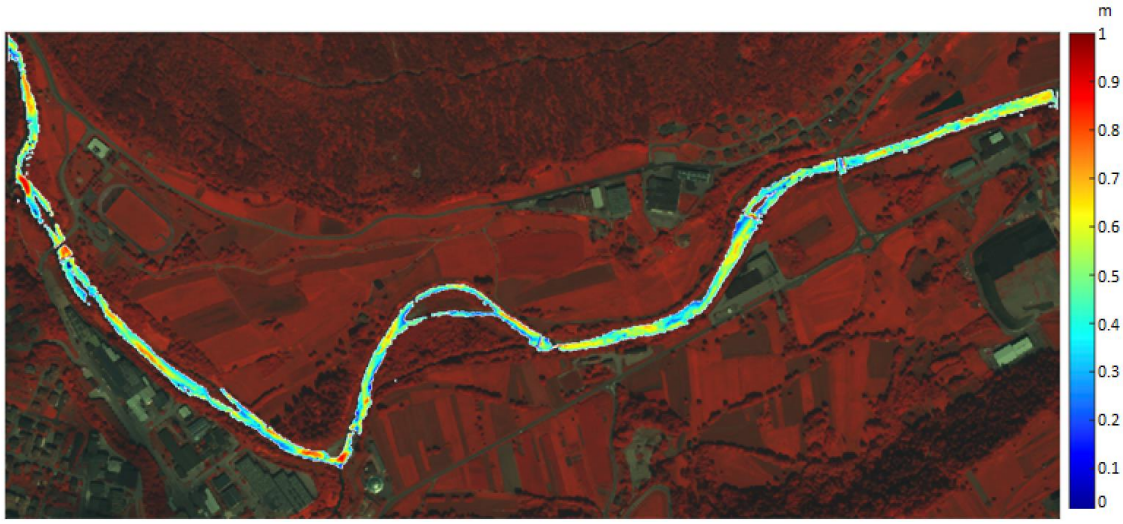

Figure 3.18 Bathymetry map derived from the proposed MODPA based on PLS regression using WV-2 image.

3.6.4 Theoretical Calibration of MODPA

Figure 3.19 illustrates the results of theoretical calibration of MODPA based on original and modified HAB models compared to the in-situ map of bathymetry. The match-up validation of HAB model shows 0.61 R^2 with an RMSE of 0.08 m. Modified HAB model improves R^2 on the order of 5% and RMSE on the order of 2 cm compared to original HAB model. This demonstrates that the theoretical calibration of bathymetric models and particularly using modified HAB model can provide comparable results with the empirical approaches.

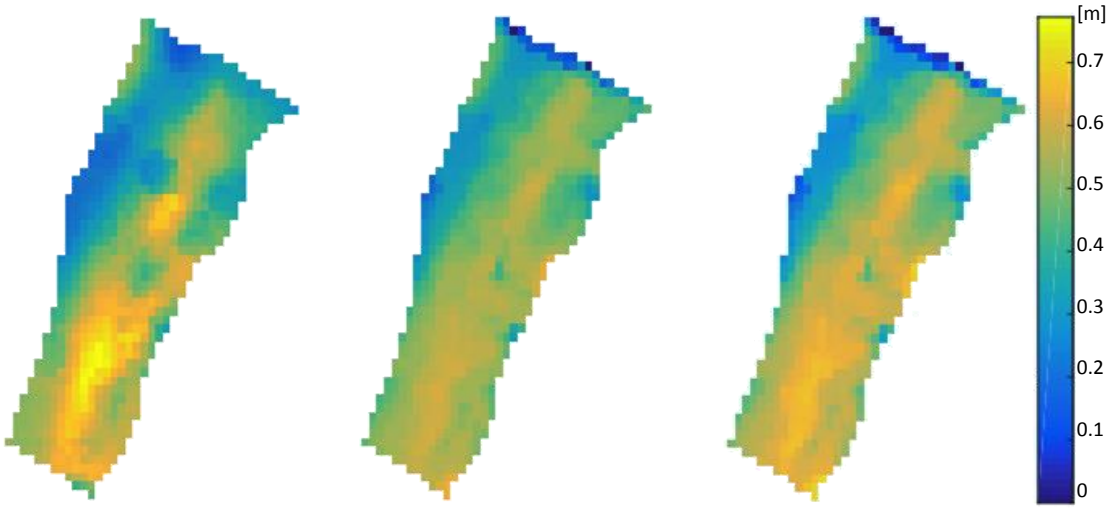

(a) in-situ (b) HAB (c) Modified HAB

Figure 3.19 Theoretical calibration of MODPA using (b) HAB and (c) modified HAB models compare to in-situ data.

Chapter 4: Riverbed Mapping

4.1 Introduction

Information on riverbed has been always an area of interest for a wide range of science and management applications in fluvial systems (Ashworth and Ferguson, 1986; Westaway et al., 2001; Woodget et al., 2014). Bottom type/composition along with the topography of riverbed defines morphology, controls flow and sediment transport and provides physical habitat (Newson and Newson, 2000; Lane et al., 2010; Legleiter et al., 2016b). For instance, submerged aquatic vegetation (SAV) plays a critical role in structuring ecological, morphological and hydraulic conditions of riverine environments. SAV provides habitat for a wide range of aquatic fauna such as fish, waterfowl, shellfish and invertebrates (Carpenter and Lodge, 1986; Strayer and Malcom, 2007) and can be considered as an indicator of water quality and general stream health (Dennison et al., 1993; Legleiter et al., 2016b). Moreover, accounting for the presence of SAV is of particular importance in hydraulic and morphodynamic modeling (Ghisalberti and Nepf, 2004; Vargas-Luna et al., 2015).

Conventional methods of field observations for collecting information about riverbed are costly, time consuming, and spatially and temporally sparse (Flynn et al. 2002; Visser et al., 2013; Villa et al., 2014). Remote sensing approaches provide an efficient means of characterizing fluvial systems across large spatial and temporal extents (Legleiter et al., 2009; Woodget et al., 2014). From a remote sensing point of view, a riverbed can be characterized based on its geometrical and spectral features. The analysis of geometry or topography of riverbed has long used aerial or close-range through-water photogrammetry techniques (Westaway et al., 2001) and recently

incorporates innovate approaches including bathymetric light detection and ranging, LiDAR (Bailly et al., 2010; Mandlburger et al., 2015) and structure-from-motion (SfM) photogrammetry using unmanned aerial vehicles, UAVs (Javernick et al., 2014; Woodget et al., 2014). However, in-stream spectral analysis has been mostly limited to bathymetry so that characterization of bottom types and compositions is still less explored in riverine environments (Legleiter et al., 2016b).

In spite of sound background in remote sensing of coastal waters, remote sensing of bottom properties in the context of riverine systems still requires significant amount of research (Visser et al., 2013; Legleiter et al., 2016b). Flynn and Chapra (2014) used supervised classification of RGB images acquired by a UAV to map nuisance green algae. Object based analysis is used to discriminate submerged macrophyte species from terrestrial and UAV images with very high spatial resolution (Visser et al., 2013). Anker et al. (2014) identified spatial resolution more influential than spectral resolution for mapping macrophyte cover in a small stream by comparing the results obtained from aerial digital photography and hyperspectral imagery (4 cm vs. 1 m spatial resolution, respectively). The key point is that most of the previous research is based upon above-water reflectance data for mapping bottom properties which is also reported by Legleiter et al. (2016b). However, above-water reflectances/radiances are influenced by attenuation of light in water column that can be a limiting factor for characterization and classification of substrate types from optical imagery (Visser et al., 2013). More recently, Legleiter et al. (2016b) examined the possibility of retrieving bottom reflectance by accounting for depth and inherent optical properties (IOPs) of water column in order to map the riverbed composition. They measured diffuse attenuation coefficient (k_d) directly in the field and then retrieved the bottom reflectances to classify sediment facies and algal density of Snake River (Wyoming, USA) from field spectra and also airborne hyperspectral imagery. In spite of their preliminary results indicating the failure of bottom reflectance retrieval in enhancing the accuracy of riverbed classification compared to that of above-water reflectance, more investigations are still needed (Legleiter et al., 2016b).

This research addresses the applicability and potentials of retrieving bottom reflectance in shallow rivers by pursuing the following objectives: (1) examining a bottom reflectance retrieval method built upon estimations of diffuse attenuation coefficient (k_d); (2) using radiative transfer

modeling and lab spectroradiometry to investigate k_d and bottom reflectance retrieval methodologies in a very controlled condition of spectral measurements and determination of submergence depths, IOPs and bottom compositions associated with fluvial environments; (3) testing the impact of deep-water correction in the process of retrieving k_d and bottom reflectances; (4) assessing the effectiveness of retrieved bottom reflectances rather than above-water reflectances in mapping the bottom types and also in extraction of SAV using vegetation indices (VIs); (5) assessing the effectiveness of enhanced spectral resolution of 8-band WV-3 imagery with respect to conventional 4-band (RGB-NIR) high resolution satellite imagery such as GeoEye in terms of streambed mapping and SAV detection; and (6) retrieving the bottom reflectances with a focus on SAV detection for the first time from space and using WV-3 imagery in riverine environments.

The spectral characteristic of riverbed is influenced not only by the type but also the roughness of substrates. Motivated by this assumption, potential of optical imagery for mapping grain size of shallow rivers is also examined in this research. Mapping of grain sizes in riverine systems can enhance the understanding from fluvial processes particularly in terms of sediment transportation (Hoey and Ferguson, 1994; Rice and Church, 1996) morphology and habitat suitability (Legleiter et al., 2016b). However, retrieval of grain sizes from optical imagery and in general remote sensing techniques has been less explored yet. The previous works on grain size mapping are all built upon texture analysis on very high spatial resolution (i.e. cm resolution) imagery collected over exposed bed materials. Arif et al. (2016) used 1 cm resolution imagery acquired by a UAV to map grain sizes based on texture parameters. Local image textures and semivariances are also used as predictors for estimation of grain sizes using cm resolution imagery (Carbonneau et al., 2004). The texture-based approach, however, is subject to some limitations and drawbacks: access to imagery with the spatial resolution suitable for texture analysis is not feasible in most of cases and more importantly, the areas with exposed substrates would be very limited along the river channel so that the extracted grain sizes would be representative only for small reaches. Therefore, developing a framework is essential to extract grain sizes information from submerged areas and based on spectral responses rather than texture features. However, this issue has not been yet addressed (Legleiter et al., 2016b) and this

study attempts to assess, for the first time, the feasibility of inferring grain sizes from spectral reflectances. The main assumption of the study is that the spectral responses of a streambed are not only affected by substrate types but also with the roughness/sizes of the bottom. To investigate this assumption, spectroscopic experiments are conducted in the hydraulic flume considering different grain sizes. The effect of changes in grain sizes are investigated on the spectra observed over substrates with same materials. The spectra observed for different grain sizes are introduced as bottom spectra for simulations through radiative transfer modeling. Then the effectiveness of bottom reflectance retrieval method is investigated for classifying the grain sizes using simulated spectra.

The following section outlines the theoretical background and the methodology of research. Section 4.3 represents the study area as well as description of spectral data including spectroscopic experiments, simulated spectra derived from radiative transfer modeling, and a satellite image. The results of implementations are presented in Section 4.4.

4.2 Methods

Bottom reflectance retrieval and mapping of underwater features have a sound background in coastal research. The early work of Lyzenga (1978, 1981) provides a physical basis for water column correction and estimation of depth-invariance indices to map bottom properties in coastal settings. A review of bottom mapping techniques developed for remote sensing of coral reef, algae and seagrass is provided by Zoffoli et al. (2014). However, relatively coarse spatial resolution of satellite imagery and difficulties in dealing with the strong water column attenuation are reported as long-standing barriers in fluvial studies (Marcus and Fonstad 2008; Visser et al., 2013). With the increasing availability of HRSI, applications of remote sensing have recently been expanded to fluvial systems as well (Legleiter and Overstreet, 2012; Hugue et al., 2016; Legleiter et al., 2016b).

Bottom mapping is poorly studied in the context of fluvial systems and has been mostly based on above-water reflectances which neglect the attenuation effects of water column. The first attempt to apply existing water column correction techniques in a riverine environment is the very recent work by Legleiter et al. (2016b) wherein limited field and spectral measurements have been

applied. Their results demonstrated that sediment facies and algal densities can be characterized based on spectral information while retrievals of bottom reflectances were unnecessary. However, they indicated that the results would be subjective so that more systematic studies including radiative transfer modeling are necessary to explore the potentials of bottom reflectance retrieval. This research attempts to employ similar physics-based approach to map bottom types using spectral data. Here, the bottom reflectance retrieval is assisted by inferring the diffuse attenuation coefficient (k_d) from image values and using some known water depths to eliminate field spectroradiometry. Then the objectives of research are followed using different source of spectral data including lab spectroscopy, radiative transfer modeling and WV-3 imagery.

The remote sensing reflectance (R_{rs}) is an apparent optical property needed essentially for interpretation of optical imagery over water bodies (Mobley, 1999; Mobley et al., 2005; Pahlevan et al., 2017a). The R_{rs} is defined as ratio of water-leaving radiance to the total downwelling irradiance just above water (Pahlevan et al., 2017a). A radiometric calibration and atmospheric correction is required to derive R_{rs} above the water surface ($R_{rs,A}$) from top of atmosphere (TOA) radiance values. Then, R_{rs} just beneath the water surface ($R_{rs,W}$) can be estimated to account for transmission and refraction at the air-water interface (Lee et al., 2002; Legleiter et al., 2016b):

$$R_{rs,W}(\lambda) = \frac{R_{rs,A}(\lambda)}{[0.52 + 1.7R_{rs,A}(\lambda)]} \tag{4.1}$$

Thereafter, the remote sensing reflectance of bottom ($R_{rs,B}$) can be estimated according to the following equation (Maritorena et al. 1994; O'Neill et al., 2011; Legleiter et al. 2016b):

$$R_{rs,B}(\lambda) = \frac{R_{rs,W}(\lambda) - R_{rs,D}(\lambda)[1 - e^{-2k_d(\lambda)d}]}{e^{-2k_d(\lambda)d}} \tag{4.2}$$

where $R_{rs,B}$ and $R_{rs,D}$ denote remote sensing reflectance of bottom and optically deep water, respectively. Note that k_d is wavelength dependent (λ), however, we drop λ for brevity in the

notations. The parameter k_d is the spectral diffuse attenuation coefficient that characterizes the propagation of light through the water column (Lee et al., 2005; Mishra et al., 2005). Legleiter et al. (2016b) estimated k_d by directly measuring the vertical profile of downwelling irradiance within water column using a spectroradiometer with waterproof accessories. In this study, we solve for k_d using water-leaving reflectances observed for different known depths and a homogenous bottom type adapted from (Mumby and Edwards, 2000; Kabiri et al., 2013). This would eliminate the field efforts for underwater spectroradiometry. Considering a small reach of river with homogenous bottom type, the changes in the bottom reflectance can be assumed negligible for a given pair of pixels ($R_{rs,B1}(\lambda) = R_{rs,B2}(\lambda)$). Then, k_d can be estimated by rearranging Equation 4.2 for each pair of pixels with different water depths (d_1, d_2):

$$k_d(\lambda) = \frac{\ln\left(\frac{R_{rs,W2}(\lambda) - R_{rs,D}(\lambda)}{R_{rs,W1}(\lambda) - R_{rs,D}(\lambda)}\right)}{2(d_1 - d_2)} \tag{4.3}$$

This approach requires reflectance values coupled with corresponding depth information. Water depth can be measured in the field or inferred from the image using bathymetry models discussed in Chapter 3 such as proposed MODPA. Some in-situ depths are required for calibration of aforementioned bathymetry techniques through forming a regression model between spectral (image-derived) quantities and water depths. This study estimates the depths of image pixels within the river channel using proposed MODPA which provides robust bathymetry retrievals with respect to substrate variability and water column heterogeneity.

Note that deep-water correction ($R_{rs,\,D}$ in Equations 4.2 and 4.3) is challenging in fluvial systems due to lack of optically deep pixels. However, the effect of the deep-water correction is most important when the signal approaches the deep water signal (i.e. the bottom-reflected signal goes to zero). In the case of shallow and clear rivers that the bottom reflectance is the dominant component of TOA radiance, deep-water correction can be dispensed particularly when the image is atmospherically corrected (Mumby and Edwards, 2000; Flener et al., 2012; Flener, 2013). That is why in most of the research in riverine environments, deep-water correction is considered negligible (Flener 2013; Niroumand-Jadidi and Vitti, 2016). However, Flener (2013) proposed an iterative procedure to estimate deep-water radiance in the absence of deep water in shallow

rivers. The deep-water radiance (L_w) can be estimated by starting with an initial value for L_w and then its modification in an iterative process in such a way to maximize the correlation between image derived quantities (X) and the water depths. Legleiter et al. (2016b) collected the spectra over the deepest part of channel (about 2 m deep) as the remote sensing reflectance of optically deep water ($R_{rs,D}$) needed for bottom reflectance retrieval (Equation 4.2). However, this assumption is subject to uncertainties and not feasible in very shallow streams. In this research, the deep-water correction is performed by Flener's method (2013) and its impact is examined on retrieving k_d and bottom reflectances in shallow rivers.

Figure 4.1 illustrates the overall workflow for mapping of bottom types using two different data sources: (A) above-water reflectances and (B) bottom reflectances. Then the bottom information extracted from both approaches are assessed with respect to the reference data to compare the potentials of above-water and retrieved bottom reflectances for characterizing substrate types and compositions of shallow rivers.

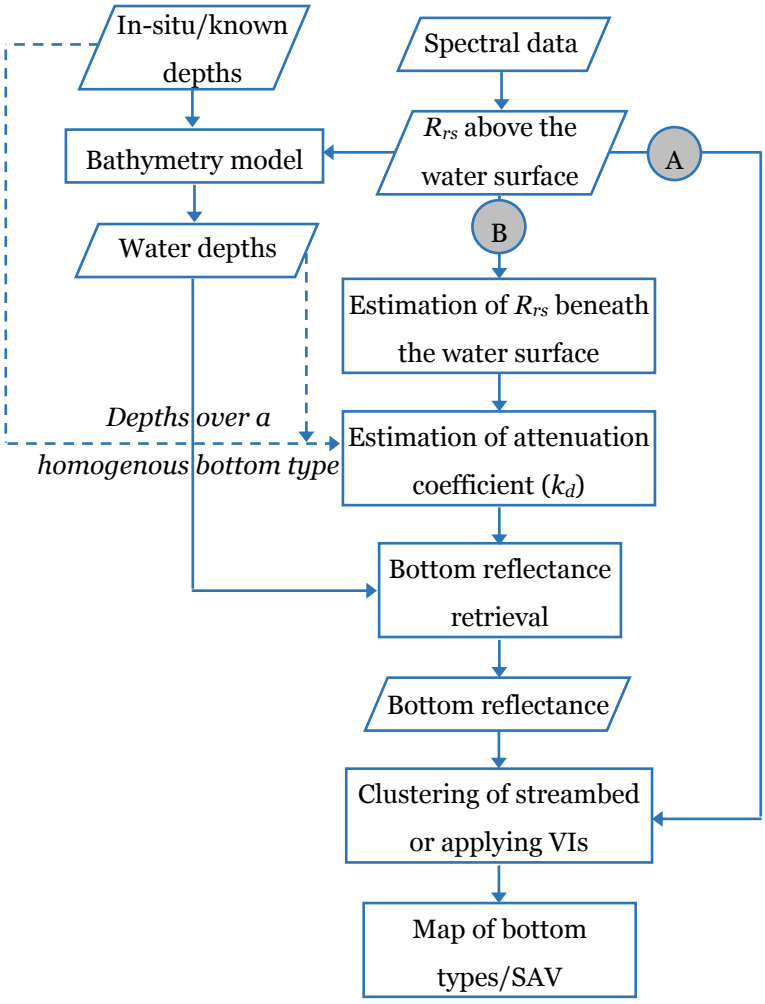

Figure 4.1 Flowchart for the mapping of streambed and delineation of SAV via (A) retrieving bottom reflectance and (B) above-water reflectance. The depth information required for k_d estimation can be collected either in the field or derived from image/spectra (shown by dashed lines).

In this research, extraction of SAV is focused as a prominent bottom property in riverine environments. In this regard, VIs with different band combinations are used to identify the SAV based on both above-water and retrieved bottom reflectances. The normalized difference vegetation index (NDVI) is very common for extraction and monitoring of terrestrial vegetation (Table 4.1). This index is developed based on characteristic feature of vegetation for which there is a sharp increase of reflectance in the transmission region from red to NIR spectrum (Jensen, 2000; Cho et al., 2012). In spite of similarities among the spectral signatures of terrestrial and aquatic vegetation, the water column characteristics such as depth and IOPs can influence substantially the spectral response observed above the water surface (Silva et al., 2008; Wolf et

al., 2013; Villa et al., 2014). More specifically, the distinctive vegetation feature becomes attenuated due to strong pure water absorption in the NIR region. Recently, a water adjusted vegetation index called WAVI (Table 4.1) is developed to account for the background water response (Villa et al., 2014). However, this index is developed and tested only in lake environments. This research investigates the effectiveness of main terrestrial and aquatic VIs for detection of SAVs in shallow rivers. The visible and NIR bands of WV-3 sensor provides 8 bands equivalent to those of WV-2 with enhanced spectral resolution compared to the traditional 4-band (RGB-NIR) sensors with high spatial resolution (e.g. GeoEye and Quickbird). More specifically, an additional spectral band located in the red to NIR transition spectrum called red-edge (RE) and also two bands over the NIR region (NIR1 and NIR2) provide more options to compute VIs. In this study, reflectance values associated with RE and NIR-2 bands are employed in the structure of NDVI and WAVI by replacing them with the traditional NIR band used in original indices. All the band combinations considered for computation of VIs using the WV-3 sensor are listed in Table 4.1.

Table 4.1 Vegetation indices (VIs) used to study SAV.

VIs	Original formula	Band combinations for WV-3 sensor
Terrestrial	$NDVI = \frac{R_{NIR} - R_R}{R_{NIR} + R_R}$	(NIR1, R) (NIR2, R) (RE, R)
Aquatic	$WAVI = (1+L)\frac{R_{NIR} - R_B}{R_{NIR} + R_B + L}, \quad L = 0.5$	(NIR1, B) (RE, B)

The VIs such as NDVI are widely used as indicators for fractional vegetation coverage where a strong correlation among VIs values and vegetation fractions has been demonstrated (Hurcom and Harrison, 1998; Elmore et al., 2000; Xiao and Moody, 2005). A regression among VIs values and known SAV fractions is used to evaluate the effectiveness of these indices for detection and mapping the density of SAV by using either above-water or retrieved bottom reflectances.

4.3 Datasets

This study applies three different spectral radiometric datasets, measured in laboratory, simulated using radiative transfer modeling, and collected by satellite sensors to perform a comprehensive assessment of the bottom reflectance retrieval methodology described above. As the main focus of research is on narrow rivers which require high spatial resolution imagery, the spectra collected in the laboratory and also simulated data are convolved with spectral responses of WV-3 and GeoEye sensors. The IOPs of water column are characterized by concentrations of TSS, Chl-a and absorption of CDOM at 440 nm wavelength. Summary and brief descriptions of the datasets are provided in Table 4.2 while more details can be found in the following subsections.

Table 4.2 Datasets used in this study and their attributes.

Datasets	Spectral characteristics	Bottom types	Water depths	IOPs
Laboratory	Spectroradiometry with 1 nm resolution convolved to WV-3 and GeoEye bands	Gravel with different sizes, SAV with different densities	0 to 0.4 m with 1 cm intervals	Clear water with low TSS (~ 2 g/m^3)
Synthetic	Hydrolight simulations with 10 nm resolution convolved to WV-3 and GeoEye bands	Sediment, Macrophyte and Dolomite, laboratory measured spectra for different grain sizes	0 to 1 m with 2 cm intervals	TSS= 2-6 g/m^3 Chl-a=1-5 g/m^3 aCDOM @ 440 nm= 0.07-0.22 m^{-1}
Satellite	WV-3 image	SAV with different densities	0 to 0.8 m	TSS ~ 3 g/m^3 Chl-a ~ 2 g/m^3 aCDOM @ 440 nm~ 0.09 m^{-1}

4.3.1 Laboratory Measurements

Spectroscopic measurements are performed on the flume-2 described in Section 3.5.1. These facilities provide the possibility of defining bottom composition and controlled measurements of both hydraulic and spectral data. The spectral data are recorded by pointing a fiber optic jumper cable in a near-nadir viewing angles from 30-cm above water surface. Similar to the experiments associated with bathymetry analysis in Chapter 3, field of view of the sensor is focused on a cell in the middle of channel to observe the spectral response of the target flow avoiding any probable adjacency effects. Three spectra are recorded for each flow condition each of which is an average of 25 individual samples. Radiometric calibrations including white reference and dark current

observations are updated for recording each spectral data in order to obtain the reflectance values.

Four sets of data are collected considering different bottom types including non-vegetated gravel bed and three submerged vegetation fractions. The latter includes high-, medium-, and low-density SAVs. For each set of data, first the reflectance of dry bottom (representing exposed material) is measured as reference bottom reflectance and then measurements are continued with 1 cm increments of water level up to maximum 40 cm (Figure 4.2).

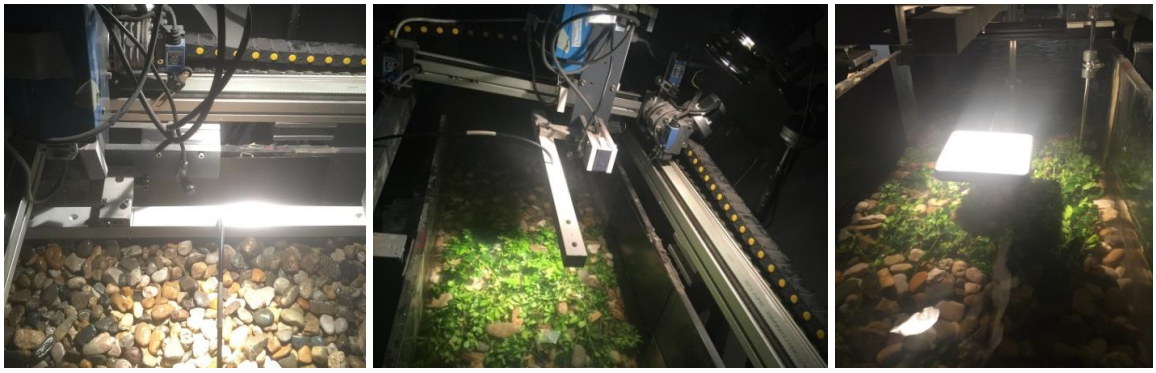

(a) (b) (c)

Figure 4.2 Spectroscopic experiments on a hydraulic flume representing spectral measurements over (a) non-vegetated gravel bed, (b) SAV and (c) white reference.

In addition, the spectra of substrates with same materiel but different grain sizes (fine, medium and coarse) are measured to investigate the effect of substrate roughness on the spectral signature (Figure 4.3).

(a) Fine (b) Medium (c) Coarse

Figure 4.3 Substrates with the same material types and different grain sizes

4.3.2 Synthetic Data

Simulated spectra from radiative transfer modeling have been used previously for bathymetry retrieval in shallow rivers (Legleiter and Roberts, 2009; Legleiter et al., 2009). However, this study would benefit for the first time from simulated spectra to gain more insights on streambed mapping in shallow submerged areas of riverine environments. These spectral data can provide a unique means of development and assessment of k_d and bottom reflectance retrieval models by having under control the main affecting parameters (i.e. bottom types, water depths and IOPs).

The remote sensing reflectances above the water surface ($R_{rs,A}$) as well as the associated k_d values across the spectrum are simulated using widely used Hydrolight radiative transfer model (Mobley, 1994; Mobley and Sundman, 2008) for three different bottom types (macrophyte, dark sediment and dolomite) and a range of IOPs representative of Sarca River and other alpine rivers. Maximum and minimum values of the IOPs are selected based on long-term (some decades) observations of water quality indicators documented by local environmental agencies and reported also in the literature (Giardino et al., 2007). A database of simulations including more than 20,000 individual spectra was produced. As most of the previous modeling studies on simulations, an analysis is performed on the spectra without allocating them spatially to pixel locations.

In addition, an image-derived bathymetry map representing a reach of Sarca River is used to spatially allocate the simulated spectra to individual pixels. This provides almost a realistic frequency of water depths and also a better visual perception. The channel is divided into three segments with different IOPs from clear to turbid water. Also each segment has one dominant bottom type but mixed up to 50% with two other bottom types. A linear mixture model is used to mix the spectra with different bottoms fractions. Figure 4.4 shows the inputs for simulating the spectra over the river channel.

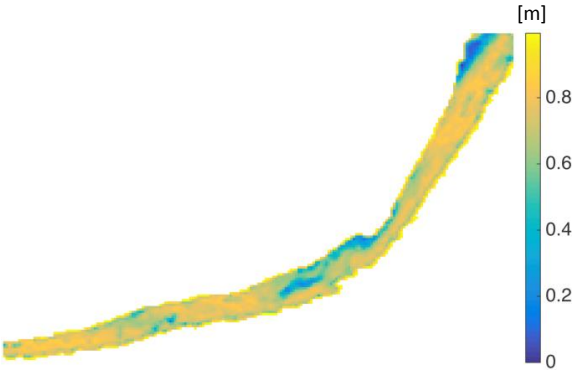

(a) Water depth

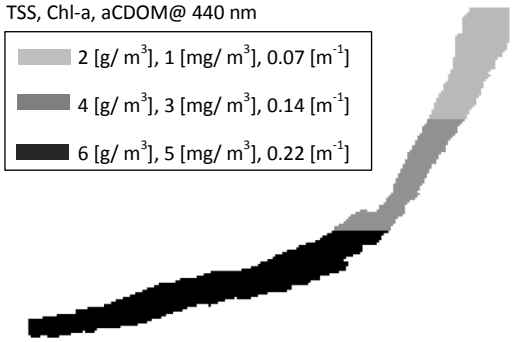

(b) Inherent optical properties (IOPs)

(c) Fractions of sediment bottom

(d) Fractions of macrophyte bottom

(e) Fractions of dolomite bottom

Figure 4.4 Inputs for simulation of river spectra.

The spectra observed over dry bottoms with different grain sizes suggest that reflectances increase with increasing the grain sizes (Figure 4.5). Note that the shapes of the spectra are identical and only the reflectance magnitudes are scaled across the spectrum depending on the grain sizes.

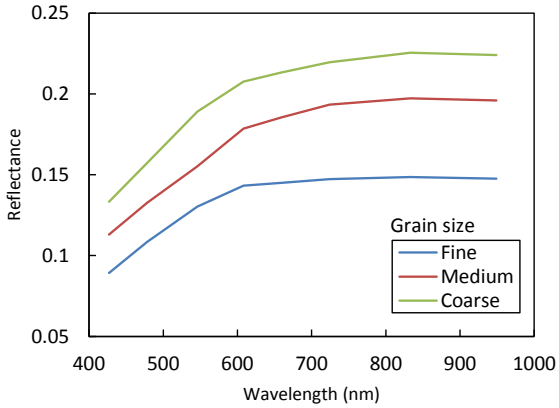

Figure 4.5 Spectral reflectances observed over dry bottoms with same materials and different grain sizes.

Similar to the simulations for studying bottom types, another set of spectra are simulated for studying grain size mapping. The spectra observed in the laboratory for different grain sizes (see Figure 4.5) are introduced to radiative transfer modeling as bottom types. Again, the simulated spectra are allocated to individual pixel locations using bathymetry map of a reach of Sarca River (Figure 4.6). The channel is divided into three segments with three levels of turbidity (IOPs). The bottom spectra for each segment are associated with one of the grain sizes. Figure 4.6 illustrates the bathymetry map and the three segments with different IOPs and grain sizes.

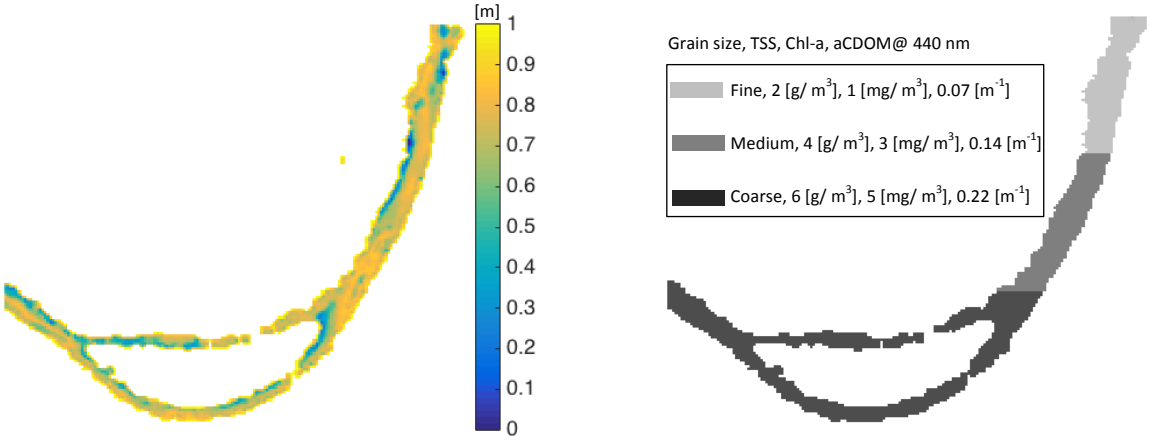

(a) (b)

Figure 4.6 Inputs for radiative transfer modeling: (a) bathymetry (b) IOPs and grain sizes. Substrates are associated with different grain sizes.

The spectra are simulated for the channel and convolved with the band passes of desired sensors (i.e. WV-3 and GeoEye). Figure 4.7 shows true color composites for the bottom (riverbed) and the above-water reflectances derived from the testing scenario associated with different bottom types.

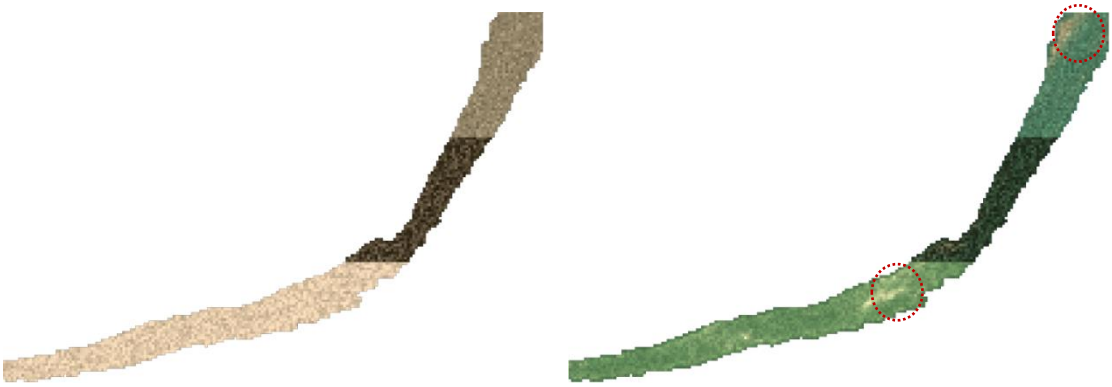

(a) Riverbed, WV-3 (b) Above-water, WV-3

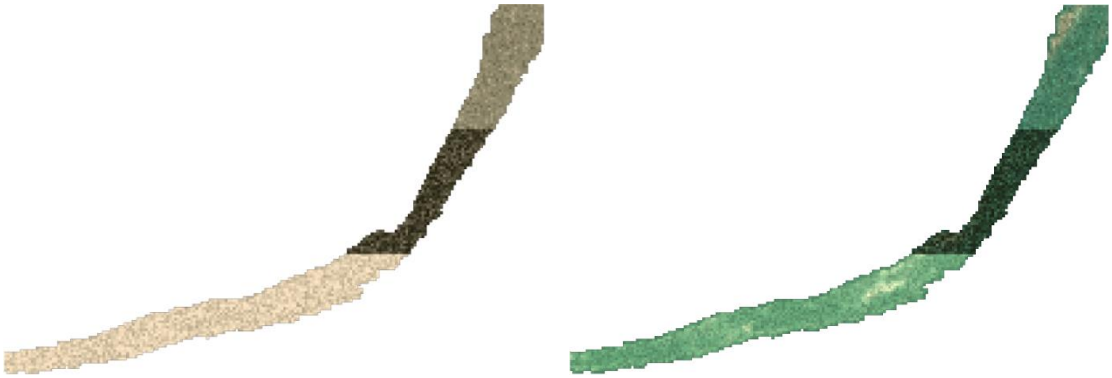

(a) Riverbed, GeoEye (b) Above-water, GeoEye

Figure 4.7 True color composite of simulated spectra associated with different bottom types coevolved with band passes of WV-3 and GeoEye.

As it is clear from true color images of above-water reflectances shown in Figure 4.7, the colors of upstream (with dominant sediment bottom) are similar to downstream colors (with dominant dolomite bottom). However, midstream (with dominant macrophyte bottom) shows relatively distinctive colors. Also two spots are highlighted by red circles on above-water reflectances of WV-3 image for which the bottom reflectances are dominant so that can be observed from above the water. This is mainly because the water is very shallow (< 20 cm) in these spots (see Figure 4.4a). The similar patterns can also be identified on above-water reflectances of the GeoEye image.

The simulated spectra associated with different grain sizes are shown in Figure 4.8.

(a) (b)

Figure 4.8 True color composite of simulated spectra associated with different grain sizes coevolved with band passes of WV-3.

4.3.3 High Resolution Satellite Imagery

An 8-band image of WV-3 sensor (equivalent to WV-2 bands) over Sarca River acquired on 1 September 2015 is also used to examine the bottom reflectance retrieval methodology for mapping SAV densities. Sarca is a shallow river in Italian Alps fed by melting from the Adamello glaciers and flowing down to the Garda Lake (Figure 4.9). In-situ water depths and also information on SAV densities are recorded using a RTK GPS rover (Figure 4.10). The in-situ depth measurements are conducted at dense points along cross-sections in three reaches. The image was georeferenced, however, some control points are collected outside the river channel for coregistration of the in-situ data with the satellite coordinates. To link the field depths to the image pixels, an ordinary kriging is used to interpolate the measured depths at the pixel level (Legleiter and Overstreet, 2012). One-half of the data is used for calibration of the proposed bathymetry model in Chapter 3 (i.e. MODPA) and the second half as check-points for accuracy assessment. The riverbed in the study area is composed of gravels (dolomite as the dominant material) with patches of SAV (Figure 4.10b). For each patch of SAV, approximate areal coverage is documented to further measure the performance of SAV mapping.

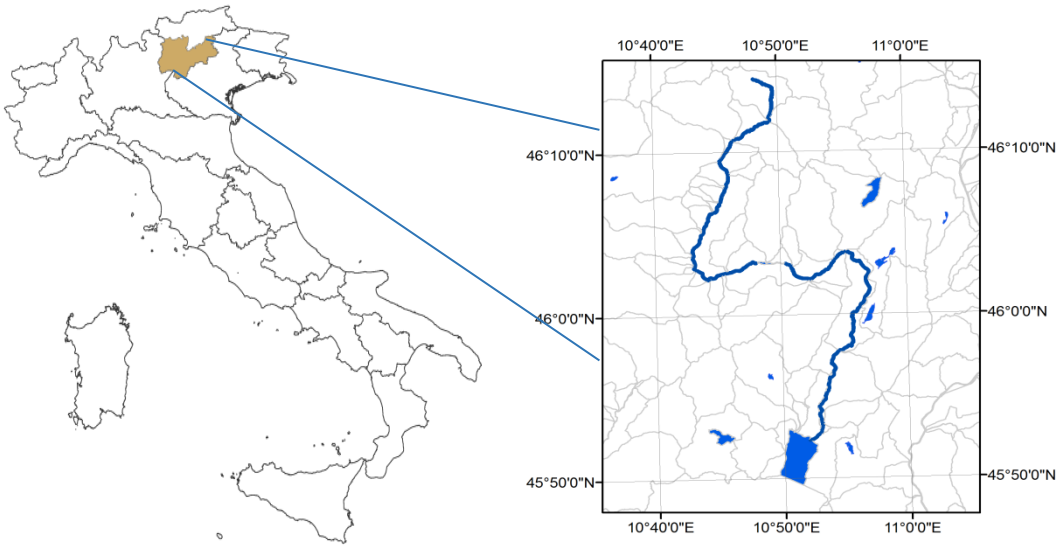

Figure 4.9 Sarca River located in Italian Alps is the main inflow of Garda Lake (shown in downstream of the river).

(a) GPS coordinates of depths and SAV (b) Sample of SAV (c) Cross-sectional depth records

Figure 4.10 Field observations of water depths and SAV using a precise RTK GPS in Sarca River.

4.4 Implementations and Results

The k_d and bottom reflectance retrieval methods are applied to the spectral data and a wide range of analysis is performed to investigate the objectives of research. In the following, the results are presented for each type of data source which provide complementary insights into benthic mapping in shallow rivers.

4.4.1 Laboratory Experiments

The above-water reflectances along with the bathymetry data collected over non-vegetated gravel bed are used to estimate k_d. Figure 4.11 shows k_d retrievals with and without applying deep-water correction which are used for estimation of the bottom reflectances. As it is clear, the impact of deep-water correction is not significant so that comparing k_d retrievals with and without applying deep-water correction, root mean square difference (RMSD) equals 0.05 1/m across the spectral channels. Direct measurement of the k_d was not possible due to not having access to water-proof spectroscopy accessories. However, measurements of substrate reflectances provide the possibility of assessing the accuracies of bottom reflectance retrievals. Though, retrieved k_d shows a reasonable trend across the spectrum so that the relatively high attenuation over coastal blue and blue bands (λ< 480 nm) can be interpreted as the impact of scattering by suspended sediment. Moreover, long wavelengths (NIR bands) show a significant increase in k_d due to the absorption by pure water.

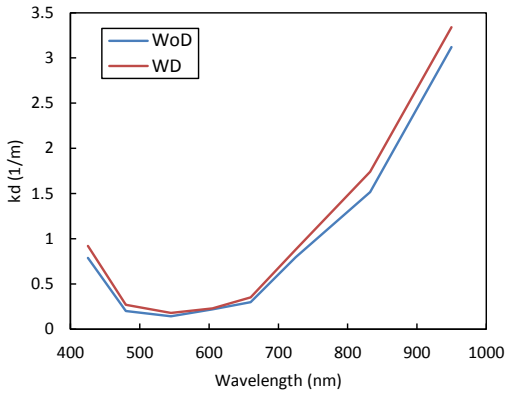

Figure 4.11 Estimated diffuse attenuation coefficient using reflectance measurements over the hydraulic flume with and without applying deep-water correction (WD, WoD).

The bottom reflectances are then retrieved from above-water reflectances using the estimated k_d. For instance, the average retrieved bottom reflectances are presented for the changing water level of the flume with non-vegetated gravel and high-density SAV substrates compared to the measured reflectances over the corresponding dry bottoms (Figure 4.12). Note that reflectances (R) are calculated from Rrs considering a Lambertian surface assumption ($R = \pi \times R_{rs}$).

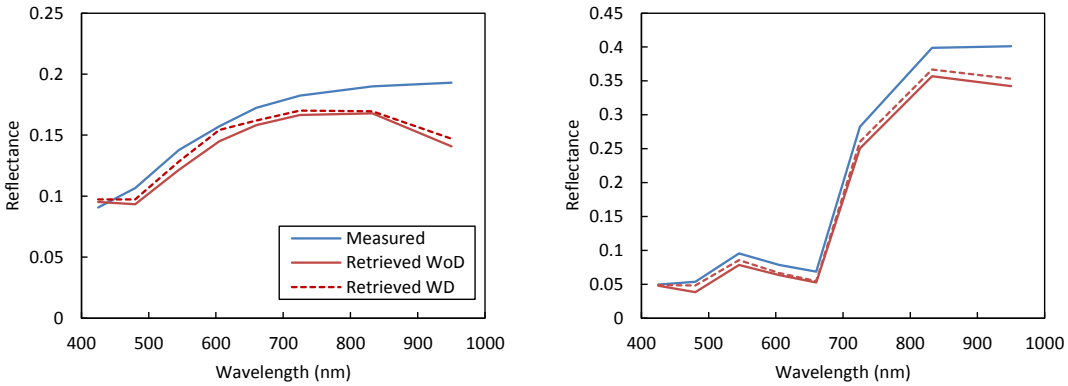

(a) Gravel (b) High-density SAV

Figure 4.12 Comparison of measured bottom reflectances with average bottom reflectances retrieved over a range of water depths in hydraulic flume for (a) non-vegetated gravel bed and (b) high density SAV using the spectra convolved to WV-3 bands.

The root mean square errors (RMSEs) are calculated to assess the performance of bottom reflectance retrievals (Equation 4.4).

$$RMSE = \sqrt{\sum_{i=1}^{N} (R_{measured}(i) - R_{retrieved}(i))^2 / N} \tag{4.4}$$

The reflectance for band i is denoted by $R(i)$ with a subscript referring to measured or retrieved spectra. N is the number of bands for which visible and NIR (λ > 700 nm) bands are analyzed separately. The retrievals of bottom reflectances show good agreements with the measured reflectances particularly across the visible spectrum and the deep-water correction slightly improves the results (Figure 4.13). The retrievals from spectra convolved with GeoEye spectral responses led to lower RMSEs over NIR spectrum compared to those of WV-3 which would be because of the extra band of WV-3 spanning over longer wavelength (NIR-2). The error bars shown on Figure 4.13 denote the effect of changing water level so that their small values demonstrates the effectiveness of water column correction over the range of water level considered in the experiments.

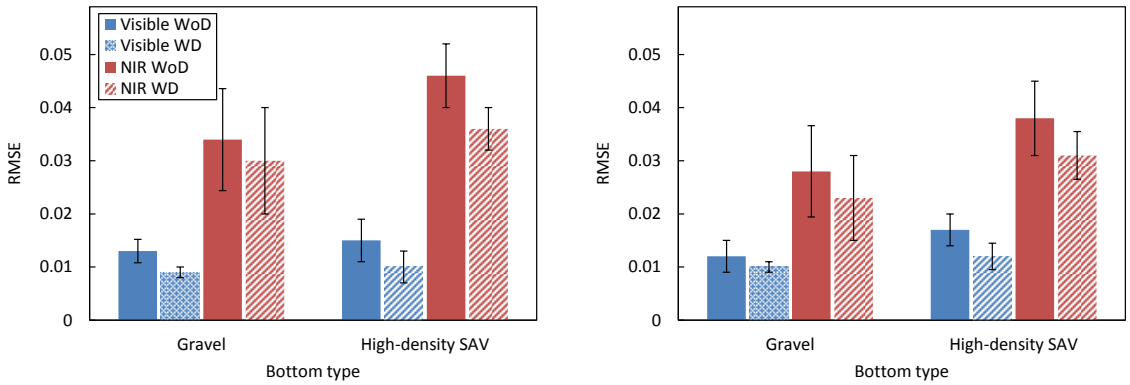

(a) WV-3 (b) GeoEye

Figure 4.13 RMSEs of retrieved bottom reflectances with and without applying deep-water correction (WD, WoD) across visible and NIR bands using the lab spectra convolved to (a) WV-3 and (b) GeoEye bands. Error bars show the effect of variable water depth.

One of the key objectives of the research is to examine the effectiveness of bottom reflectance retrieval (i.e. water column correction) for identification of substrate properties compared to simply using above-water reflectances. In Figure 4.14, the above-water reflectances are compared with the corresponding retrieved bottom reflectances for 40 cm deep water considering low, medium and high densities of SAV. As it is clear the characteristic feature of vegetation (i.e. high spectral response in NIR) is very strong and detectable on retrievals of bottom reflectances. This is while this feature tends to fade for above-water reflectances where it totally disappears for the low-density SAV.

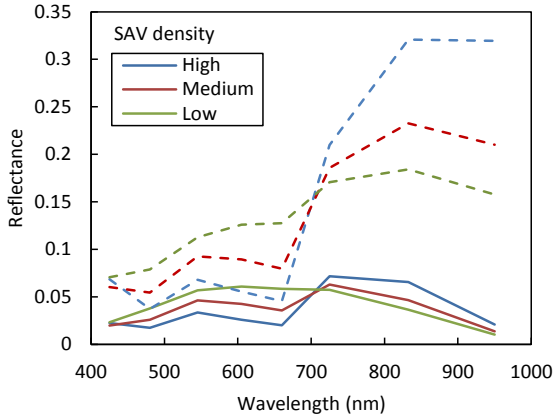

Figure 4.14 Comparison of reflectances before and after water column correction (solid- and dash-lines, respectively) above 40 cm deep water with different SAV densities in the hydraulic flume.

The terrestrial and aquatic VIs are applied to both above-water reflectances and retrievals of bottom reflectances for SAV with different densities. The VIs derived from each of band combinations lead to clusters which are associated with the four SAV densities (see Figure 4.15, zero density denotes non-vegetated gravel bed). The clusters of VIs derived from above-water reflectances show considerable overlaps which mitigates the separability among different SAV densities. To elaborate more on this, k-means algorithm is applied to VIs to cluster them into four classes. The overall accuracies and the kappa coefficients are presented for VIs with different band combinations (Figure 4.15). The VIs built upon RE band demonstrated better performance compared to the other band combinations using above-water reflectances. More specifically, the (RE, R) band combination yields the highest accuracy with 92 % overall accuracy and kappa coefficient of 89 %. Aquatic VIs provide no further benefit for clustering SAV densities using above-water reflectances. The clusters obtained from retrieved bottom reflectances show perfect distinction among SAV densities for all the band combinations. As it is shown on Figure 4.15b, the clusters are much separated which provides a perfect distinction among different SAV densities. On the other hand, they are very compact that reveals the little effect of changing water depth on VI values for each cluster which confirms the successful correction of the water column effect. However, it should be considered that the results are based on observations which are limited to a maximum 40 cm deep and clearly flowing water. The results are shown only for the case without applying deep-water correction as it provides the perfect clusters and no more enhancements are required.

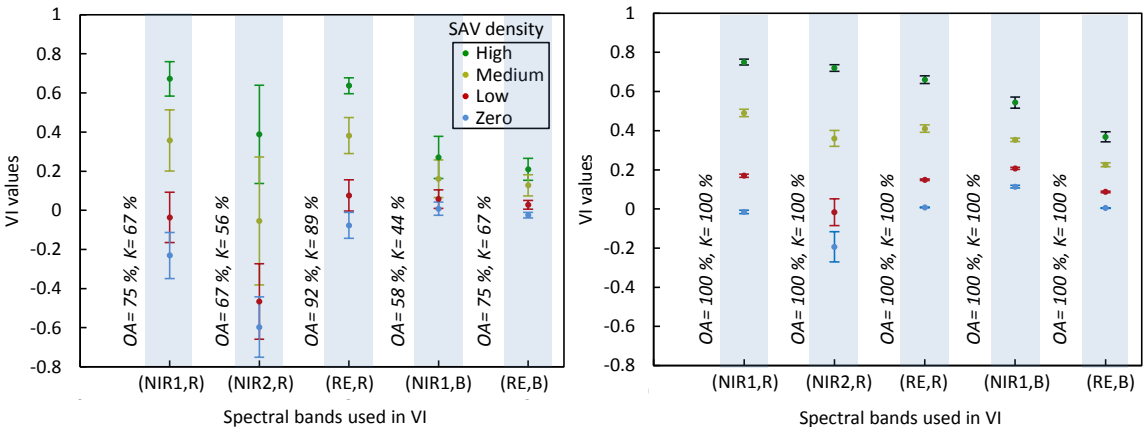

(a) Before water column correction

(b) After water column correction

Figure 4.15 Evaluating the effectiveness of VIs in distinguishing among SAV with different densities using (a) above water reflectances and (b) retrieved bottom reflectances without deep-water correction over the hydraulic flume. Error bars indicate the effect of variable water depth.

4.4.2 Synthetic Data Analysis

Here, using simulated data, we examine the performance of k_d retrievals in various water-column conditions across the river channel. This provides an investigation on a wide range of water column properties (IOPs and water depth) and bottom compositions. The k_d parameter is estimated using the above-water reflectances for the simulated river channel presented in Section 4.3.2. In this regard, two retrievals are considered: (a) upstream composed of dominant substrate type of sediment and clear water and (b) downstream including dominant substrate type of dolomite and relatively turbid water. The estimations with and without applying deep-water correction are compared with the average simulated k_d for entire channel using WV-3 bands (Figure 4.16). This is to investigate the effectiveness of k_d retrieval in the case of variable IOPs across the river channel. A limited number of pixels (~ 20) are taken as samples for each k_d retrieval.

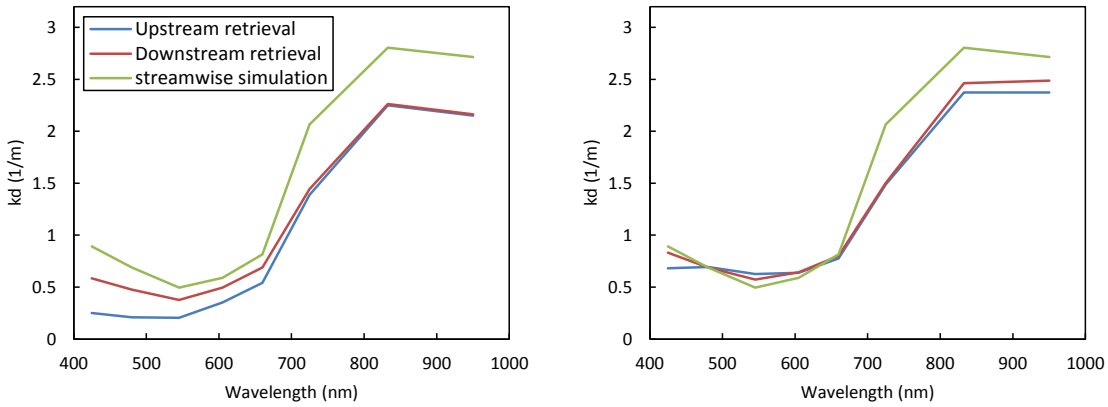

(a) WV-3, without deep water correction (b) WV-3, with deep water correction

Figure 4.16 Diffuse attenuation coefficient (k_d) retrievals for the simulated river channel compared to known values from Hydrolight simulations.

Figure 4.17 shows the RMSEs of upstream and downstream k_d retrievals with and without applying deep-water correction. Downstream estimations of k_d are more accurate than upstream retrievals particularly for the visible bands. This was expected because downstream IOPs are more representative for entire stream rather than upstream (downstream is a larger segment with more pixels). Deep-water correction also leads to improvements of k_d retrievals. Similar to the results of lab experiments, simulated GeoEye spectra provide slightly lower RMSEs of k_d retrievals in NIR spectrum.

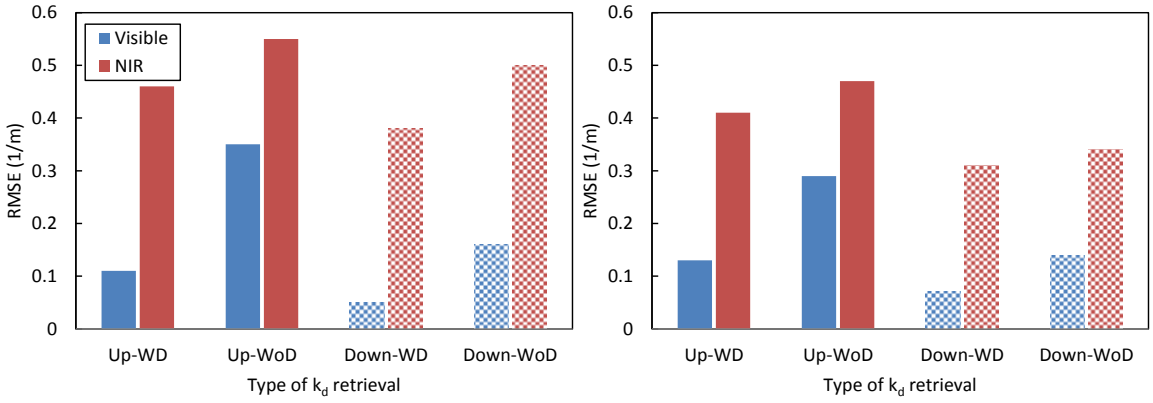

(a) WV-3 (b) GeoEye

Figure 4.17 Performance of k_d retrievals for upstream (Up) and downstream (Down) of the simulated channel with and without deep water correction (WD, WoD) expressed in terms of RMSE (1/m). Hatched bars are used for downstream to make them distinctive from upstream data.

Following by estimation of k_d, bathymetry map of the simulated channel is also retrieved which is required for inferring the bottom reflectance of each individual pixel. To calibrate the bathymetry model only 1% of the channel depths are selected randomly. Then MODPA is applied between spectra-derived quantities and the associated water depths. The spectra-derived depth map is illustrated in Figure 4.18a for WV-3 bands. The validation is performed by matching up the retrieved depths against the known values for the entire channel. The resultant R^2 of 0.99 and RMSE of 0.01 m indicate the high performance of MODPA in a variable IOPs and substrate types (Figure 4.18b).

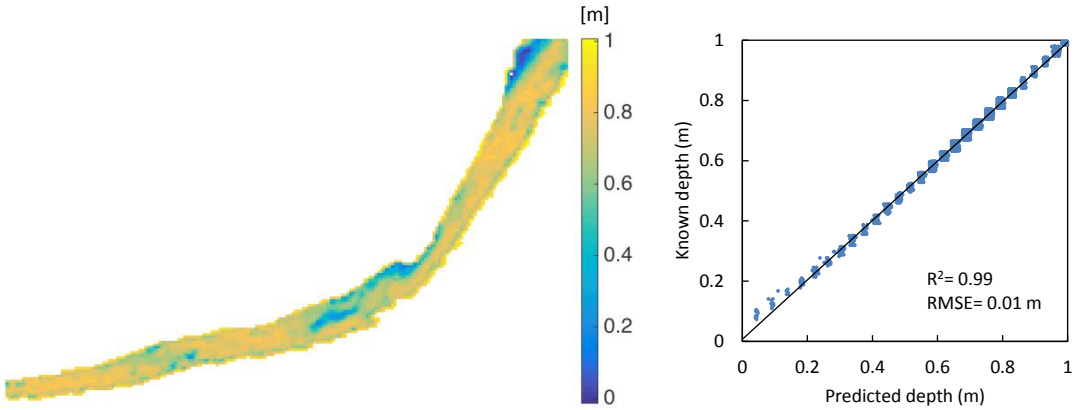

(a) Bathymetry derived from synthetic data (b) Match-up validation

Figure 4.18 (a) Bathymetry map retrieved for the simulated channel based on the spectra convolved to band passes of WV-3 and (b) match-up validation of retrieved depths versus known values.

Figure 4.19 shows the true color composite of bottom reflectance retrievals considering upstream and downstream k_d estimations of the simulated river channel without applying deep-water correction.

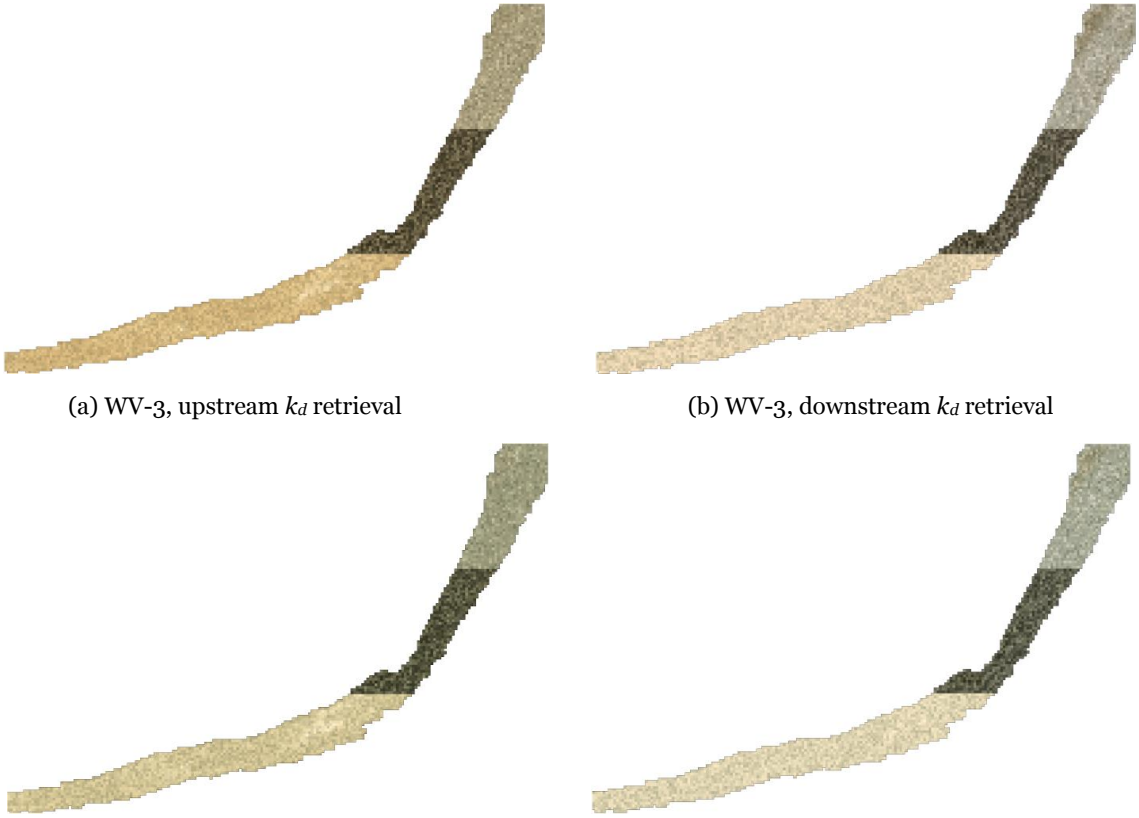

(a) WV-3, upstream k_d retrieval

(b) WV-3, downstream k_d retrieval

(c) GeoEye, upstream k_d retrieval

(d) GeoEye, downstream k_d retrieval

Figure 4.19 True color composite of retrieved riverbed without deep water correction based on upstream and downstream k_d retrievals of the simulated channel.

The performance of the bottom reflectance retrievals is assessed using a clustering method. The k-means (Hartigan and Wong, 1979) algorithm, a frequently used unsupervised classifier, is applied to above-water and the retrieved bottom reflectances to map the riverbed classes. As a reference map for accuracy assessment, each segment of the river channel is labeled with the bottom type dominant in that segment. As evident in Figure 4.20, above-water reflectances lead to considerable number of misclassified pixels particularly with a confusion between the bottom types of the upstream (dominant sediment) and downstream (dominant dolomite) segments. This was expected to some extent by the existing visual similarities between true color composites of above-water reflectances for these two segments (Figures 4.7b and 4.7d).

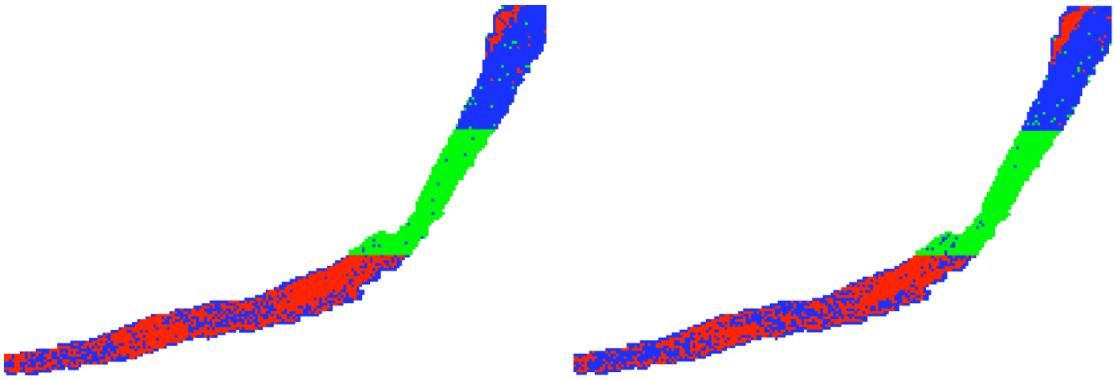

(a) WV-3 (b) GeoEye

Figure 4.20 Clustering of riverbed using above-water reflectances of the simulated channel.

Figure 4.21 demonstrates the substrate clusters derived from bottom reflectance retrievals without applying deep-water correction which shows considerably less misclassified pixels compared to those of obtained from above-water reflectances.

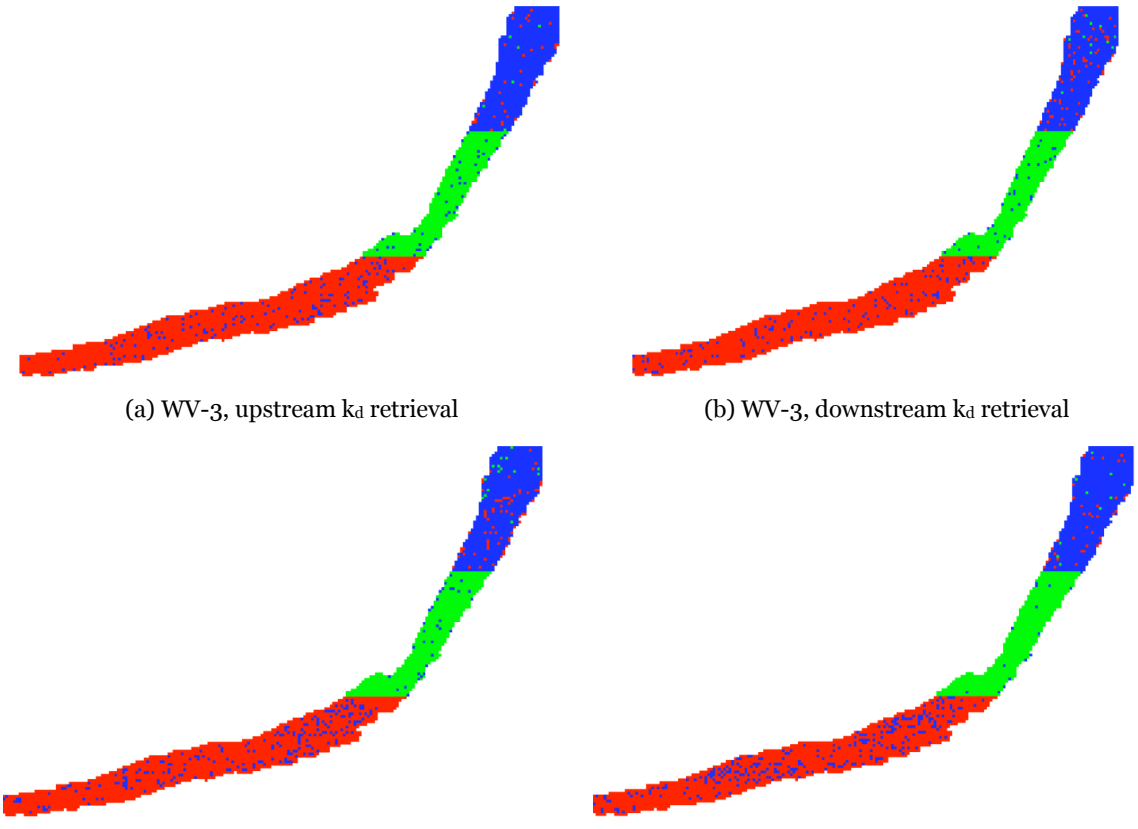

(a) WV-3, upstream k_d retrieval (b) WV-3, downstream k_d retrieval

(c) GeoEye, upstream k_d retrieval (d) GeoEye, downstream k_d retrieval

Figure 4.21 Clustering of riverbed using retrieved bottom reflectances without deep-water correction based on upstream and downstream k_d retrievals of the simulated channel.

The quality of bottom maps is assessed quantitatively by calculating the overall accuracies and kappa coefficients. In the reference map needed for building the confusion matrix, obviously, each pixel is assigned to the bottom type with the most abundance which yields to three distinct clusters corresponding to the before-mentioned three river segments. The retrievals of bottom reflectances yield significant improvements (about 20% overall accuracy and 30% kappa coefficient) in mapping bottom types with respect to above-water reflectances either using WV-3 or GeoEye bands (Figure 4.22). Deep-water correction improves slightly the bottom mapping (about 2-3%). Further, downstream k_d retrievals yield slight improvements compared to upstream retrievals (about 2-3%) which shows insignificant impact of IOPs variability on the substrate mapping process in the range of parameters discussed in this study. However, this probably would have considerable effects when detailed spectral information is required for mapping the substrate properties (e.g. bottom types with very similar spectral responses such as different types of SAV) or in the case of high level of variability in IOPs which requires more investigations.

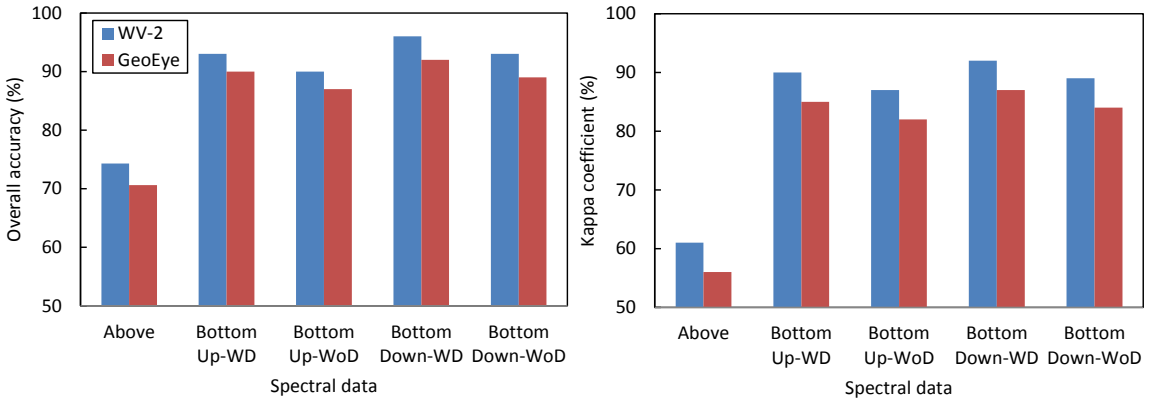

Figure 4.22 Overall accuracies and kappa coefficients of the bottom maps obtained from above-water and retrieved bottom reflectances (denoted by Above and Bottom, respectively). The statistics are presented for upstream (Up) and downstream (Down) k_d retrievals with and without deep-water correction (WD, WoD) for the spectral convolution to WV-3 and GeoEye bands.

To evaluate the effectiveness of VIs for detection of SAV densities, a regression of VIs versus the known SAV (macrophyte) fractions is performed. The coefficient of determination (R^2) and RMSE of regressions indicate the significantly stronger correlation between VI values and SAV densities for inferred bottom reflectances than for above-water spectra based on all of band combinations (Figure 4.23). The strongest correlation is for (RE, R) band combination for both above-water

reflectances (R^2 = 0.48 and RMSE = 0.2) and inferred bottom spectra (R^2 = 0.85 and RMSE = 0.07). This demonstrates the significance of the RE band of WV-3 for mapping benthic vegetation in shallow rivers which is missing for the GeoEye sensor. There are also some evidences from studies in wetlands demonstrating usefulness of the RE band for mapping benthic vegetation and without applying any water column correction (Lane et al., 2014; Whiteside and Bartolo, 2015). Deep-water correction also slightly improves the regression statistics.

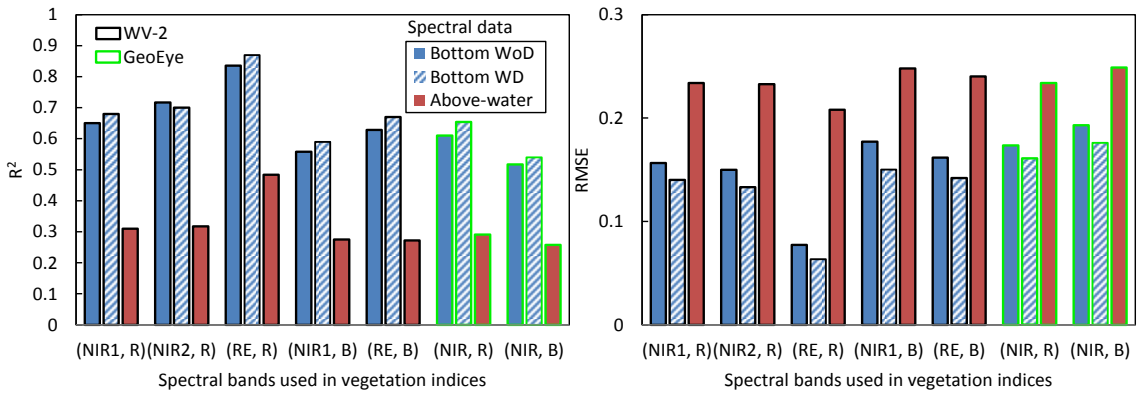

Figure 4.23 R^2 and RMSE of regressions between VI values and macrophyte fractions for above-water and inferred bottom (Bottom) reflectances.

Additional analyses are performed on the database of simulated spectra to elaborate the performance of bottom reflectance retrievals in different levels of water depths and IOPs. Figure 4.24 indicates the RMSEs of inferred bottom reflectances across a range of water depths considering constant IOPs and using the spectra convolved to the band passes of WV-3. In general, visible bands are retrieved with high accuracies and the water depth has less of an effect on RMSEs of these bands. The RMSEs of NIR bands increases sharply by water depth particularly without applying deep-water correction. The effect of deep-water correction is pronounced for relatively deep water (depth > 0.5 m) where improves the bottom reflectance retrievals particularly in NIR spectrum.

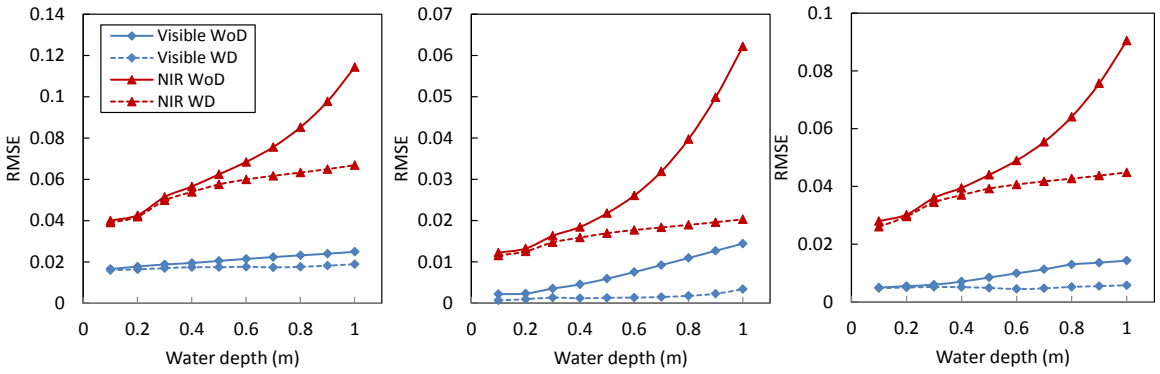

(a) Dolomite (b) Macrophyte (c) Sediment

Figure 4.24 RMSEs of bottom reflectance retrievals across a range of water depths and three bottom types with and without deep water correction (WD, WoD) using simulated spectra convolved to WV-3 spectral bands. IOPs are constant (TSS = 4 g/m^3, Chl-a = 3mg/m^3, CDOM= 0.14 m^{-1}).

Further, three levels of turbidity are assumed associated with the range of IOPs for Sarca River and similar Alpine rivers: low (TSS= 2 g/m^3, Chl-a= 1 mg/m^3, CDOM= 0.07 m^{-1}), medium (TSS= 4 g/m^3, Chl-a= 3 mg/m^3, CDOM= 0.14 m^{-1}) and high (TSS= 6 g/m^3, Chl-a= 5 mg/m^3, CDOM= 0.22 m^{-1}). The efficacy of bottom reflectance retrievals is then evaluated in constant and thick water column (1 m). The RMSE of bottom reflectance retrievals in NIR bands increases by increasing the turbidity while the retrievals in visible bands are less affected. Deep-water correction improves the retrievals of bottom reflectances particularly for NIR bands (Figure 4.25).

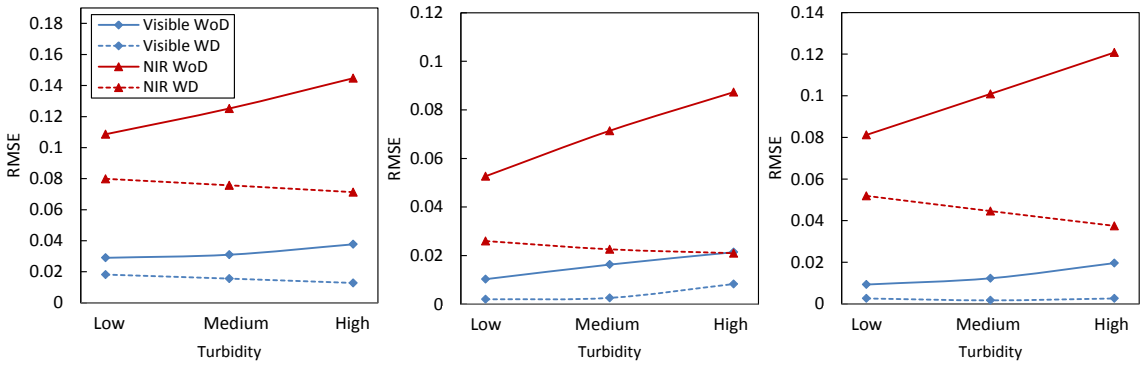

(a) Dolomite (b) Macrophyte (c) Sediment

Figure 4.25 RMSEs of bottom reflectance retrievals across a range of IOPs and three bottom types with and without deep water correction (WD, WoD) using simulated spectra convolved to WV-3 spectral bands. Water is constantly 1 m deep.

The effectiveness of bottom reflectance retrieval method is also examined for making distinction among grain sizes. The bottom reflectances are retrieved for the simulated channel with different

grain sizes (Figure 4.26a). Then, k-means algorithm is applied on the retrieved bottom reflectances to cluster the streambed into three grain size classes (Figure 4.26b). The resultant overall accuracy of 92% and kappa coefficient of 0.88 indicate high potentials of bottom reflectance retrieval for mapping grain sizes in shallow rivers and in the range of IOPs discussed in this study.

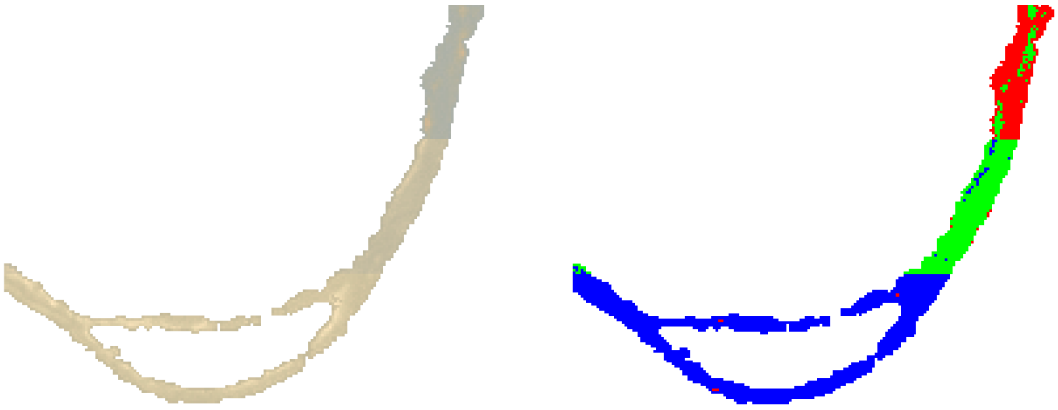

(a) (b)

Figure 4.26 (a) true color composite of retrieved bottom reflectances and (b) grain size clusters.

4.4.3 High Resolution Satellite Image

The 8-band WV-3 image of the study area is first atmospherically corrected using the MODTRAN model. Then the k_d parameter is estimated using in-situ depths and associated above-water remote sensing reflectances over a segment of Sarca River with homogenous bottom type with and without deep-water correction. The bathymetry map of the channel is estimated by calibrating the MODPA with random half of the in-situ measured depths. The image-derived depth map is shown in Figure 4.27b for a reach of the river interested for SAV mapping compared to the field observation for the same area (Figure 4.27a). The validation of depth retrievals is performed based on the remaining half of the in-situ depths as independent check points (Figure 4.27c).

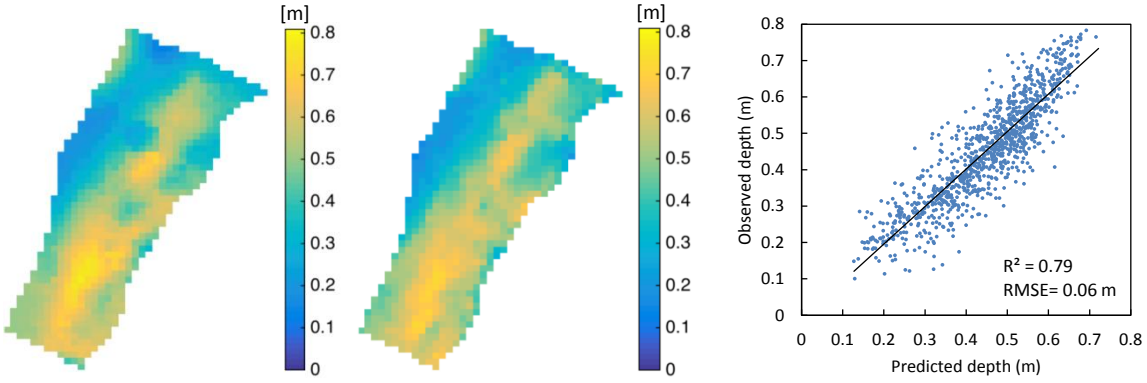

(a) in-situ depths (b) image-derived depths (c) validation of depth retrievals

Figure 4.27 Image-derived bathymetric map of Sarca River compared to the in-situ depths and match-up validations using independent check points.

Samples of retrieved bottom reflectances compared to corresponding above-water reflectances are illustrated in Figure 4.28 for different SAV densities observed in Sarca River. The characteristic feature of vegetation becomes sharply detectable on retrievals of bottom reflectances and deep-water correction slightly impacts the spectra (Figure 4.28b).

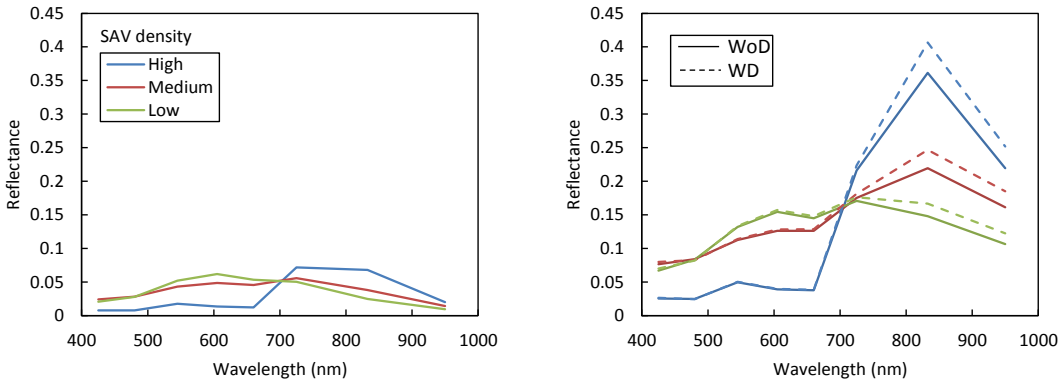

(a) above-water (b) retrieved bottom

Figure 4.28 Samples of (a) above-water reflectances of SAV with different densities observed by the WV-3 sensor over Sarca River and (b) associated retrieved bottom reflectances with and without deep-water correction (WD, WoD). The spectra are selected in 30-40 cm water depths.

The areal coverage data of SAV patches gathered in the field are converted to a density index by dividing the observed area of a patch by the sensor's pixel coverage (1.6 m ×1.6 m for the WV-3 data used in this study). Then the index values are clustered using k-means algorithm to three density classes to be used as reference map (Figure 4.29a). The effectiveness of VIs is examined in terms of making distinction among SAV densities by using both above-water and inferred bottom reflectances. The VIs derived from spectral data are clustered using k-means algorithm and

compared with the in-situ reference map. The best results are achieved based on the (RE, R) band combination for both above-water and retrieved bottom spectra (Figures 4.29b and 4.29c).

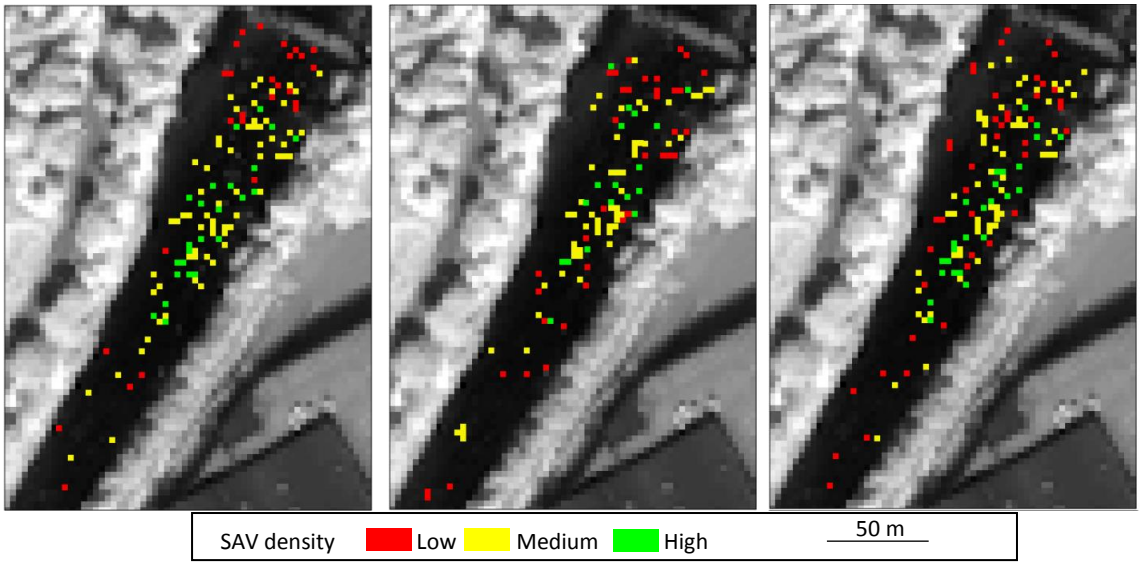

(a) In-situ reference map (b) Above-water (c) Retrieved bottom

Figure 4.29 Clustering of SAV densities using the VI values derived from (RE, R) band combination for (b) above-water and (c) retrieved bottom reflectances compared to the (a) in-situ reference map.

The user and producer accuracies of SAV density clusters indicate that the retrieved bottom reflectances yield remarkable higher accuracies than above-water spectra for all the SAV densities. However, the accuracies of clustering from above-water spectra increase by increasing the density of SAV (45% user accuracy and 57% producer accuracy for high density SAV). This is also valid for clustering from retrieved bottom reflectances with a lower magnitude (Figure 4.30).

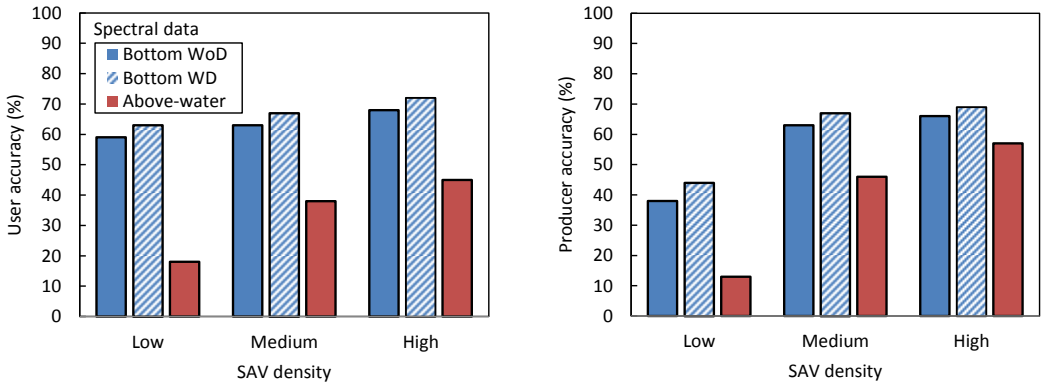

Figure 4.30 User and producer accuracies of SAV density clusters derived from (RE, R) band combination for the VI using above-water and retrieved bottom reflectances.

Chapter 5: Discussion and Conclusions

This final chapter provides a summary and discussion about key findings of the three main research elements. Overall conclusions and suggestions are then provided in the last section of chapter.

5.1 Delineation of River Boundaries

Addressing the problem of mixed boundary pixels can enhance the accuracy of remote sensing applications in the river science. Unmixing and SRM are considered as key tools respectively to spectral and spatial decomposition of the mixture in river boundaries. The former estimates the water fractions and the latter allocates the fractions in proper sub-pixel locations. Both of these steps have been the focus of this study in order to examine and develop the techniques for mapping of river boundaries at the sub-pixel resolution. Two different testing approaches are considered to survey the efficiency of SRM algorithms, while accounting for absence and presence of uncertainty in the input data (i.e. fractions obtained from unmixing). Semi-simulated fractions are used as a contrived input with known fractions which provide a unique means of assessing the performance of the spatial allocation of sub-pixels. Moreover, the comparison between hard classification and SRM algorithms can be facilitated. This is because the hard labeling of pixels also can be applied on semi-simulated fractions without any uncertainty by deciding on the most abundant class (water/non-water) within the pixels. In the second testing approach, real water fractions are estimated based on a proposed method, namely OBA-NDWI, as well as using the fully constrained algorithm of SPU. The rationality behind the proposed OBA-NDWI is to take advantages from the ease of use of water indices in order to estimate water fractions. The OBA-

NDWI performs the NDWI with all the possible combinations of spectral bands to identify the pair of bands for which the NDWI values yield the highest correlation with water fractions. To analyze the relation of NDWI values and water fractions through OBA-NDWI, a linear mixture of image-derived spectra is used to simulate all the possible mixing fractions of selected endmembers. The proposed OBA-NDWI method permits a systematic approach to find the optimal combination of bands for calculation of NDWI which can also be instrumental for images with high spectral resolution. This benefits both hard and soft classification of water features where the highly correlated NDWI to water fractions can enhance the accuracy of the extraction of water features either at the pixel or sub-pixel level. The semi-simulated and real fractions are employed for SRM based on the PS algorithm as well as interpolation-based techniques. Moreover, the MBPS algorithm is developed to provide a non-iterative alternative to the traditional PS. The accuracy and computational proficiency of the techniques are explored on two case studies using HRSI.

Results obtained from SRM of semi-simulated fractions demonstrate that hard classification is suffering remarkably from the mixture in boundary pixels where the extracted border lines are very rough and are missing the detailed proximity with riparian zone. In this regard, the user and producer accuracies of the hard classified river map would be lower over than 10% compared to the SRM techniques. In general, interpolation-based techniques, as well as the proposed MBPS algorithm, produce comparable results with the PS algorithm. However, it seems that the producer accuracy of interpolation-based techniques decreases much faster than PS/MBPS from an increase in *ZF*. As another key point, increasing the *ZF* leads to a higher degree of uncertainty in allocating the fractions in sub-pixel locations. So, a trade-off between the accuracy of SRM algorithms and *ZF* should be taken into account.

The resultant real water fractions from the proposed OBA-NDWI are coherent and very close to the results of SPU method and show promising outputs especially for $ZF \leq 5$. However, the computational complexity of estimating water fractions based on the OBA-NDWI method is significantly less than that of the SPU algorithm. Comparing the two testing approaches reveals that the spatial allocation process of sub-pixels using SRM techniques is very accurate in the context of mapping river boundaries (above 95% user/producer accuracy for $ZF \leq 6$). This is

while, considering the entire sub-pixel mapping process, the importance of the estimating water fractions (unmixing) seems to be more crucial than spatial allocation of the sub-pixels. The PS and MBPS algorithms preserve the input water fractions while the fraction values can be not respected through interpolation-based SRM. In the discussed case studies, some isolated non-water sub-pixels appear on the PS and MBPS maps that applying a majority filter (mainly with a kernel size corresponding to the *ZF*) reduced this effect properly. The main advantage of interpolation-based and MBPS algorithms is their high computational efficiency which are, respectively, 20 times and 3 times faster than the PS algorithm.

The common thresholding methods, including Otsu's method and simple zero-thresholding, are applied through OBA-NDWI to investigate their effectiveness in hard classification of water features. According to the results, Otsu's threshold value and corresponding cut-off water fraction significantly depend on the spectral bands used for the calculation of the NDWI. The minimum water fraction in Otsu's water mask is, in general, observed higher than adequate amount (50%) for binary hard classification. The zero-thresholding suffers from both underestimation and overestimation of water pixels. This shortcoming of thresholding methods can suppress the labeling of boundary mixed pixels. The proposed OBA-NDWI method has the potential for selecting the proper threshold for hard classification using NDWI values and requires more investigation.

5.2 River Bathymetry

Thin and less complex water column of shallow and clearly flowing rivers permits the bottom component of radiance to reach sufficiently to the sensor. Although this radiance component is desired for bathymetry retrieval, it is affected not only by water depth but also by substrate types and compositions. Development of methods robust to the substrate variability is then essential to retrieve the bathymetry of shallow and clear rivers from optical imagery. Mapping of river bathymetry from satellite imagery is relatively new and the techniques are being adapted from conventional coastal studies. The existing empirical models employ one type of Lyzenga or ratio predictors through a linear regression to build the depth prediction model. Simple regression

models use only one predictor either Lyzenga or ratio where OBRA identifies the optimal single ratio predictor among all the possible ratio predictors. There is also a multiple regression model which is based on Lyzenga predictors in order to enhance the robustness of model with respect to substrate variability and water quality heterogeneity. This research introduced MODPA to take the advantages of both Lyzenga and ratio predictors and also to integrate extra predictors obtained from the intensity component of HSI color space. In this regard, all the possible Lyzenga and ratio predictors derived from original image as well as the intensity bands of HSI color space are considered as initial predictors. A set of optimal predictors can be then selected based on one of PLS, PC or stepwise regressions.

To support the objectives of research, spectroscopic experiments are performed in the hydraulic laboratory that allowed controlled conditions for measuring reflectances with associated water depths as well as defining the bed compositions. The spectra are convolved with WV-2 and GeoEye spectral responses for further analysis. Further, simulated spectra derived from radiative transfer modeling are used to extend the bathymetry analysis to a wider range of water depths and IOPs and also to consider more variability in bottom types. A WV-2 image and its spectral convolution to GeoEye bands are used to examine the bathymetry models where the additional bands of WV-2 are also assessed for depth retrievals in Sarca River. Moreover, the newly released AComp product is evaluated for the first time to understand the robustness of MODPA and other bathymetry methods with respect to the atmospheric effects.

Lyzenga's single predictor is demonstrated to be very sensitive to substrate types so that the residuals of predicted depths showed distinct patterns for the two substrate types used in the two flumes. Although this predictor is not appropriate for depth retrieval, it might have the potential for classification of riverbed compositions. The OBRA also showed a poor robustness with respect to substrate variability existing between two flumes. Despite identification of optimal pair of bands for the ratio model, OBRA is a single predictor model and most likely neglects other explanatory variables. Multiple Lyzenga predictors enhance the robustness of model with respect to variable bottom types. However, this model does not account for any process to select optimal predictors that most likely lead to over-parameterization problem. This problem would arise more significantly when hyper-spectral imagery or extra predictors are used. As it can be inferred from

the results, the multiple Lyzenga model with extra predictors is less accurate than that of without any extra predictor using WV-2 data. This suggests making use of extra predictors when a selection process is performed on the predictors. As OBRA and proposed MODPA identify the optimal predictor/s, they yield improved results with extra predictors. More specifically, the single optimal predictor of OBRA for the GeoEye image is resultant from extra predictors. This shows the effectiveness of extra predictors for bathymetry mapping from the imagery with low spectral resolution. The results of bathymetry models applied on simulated spectra suggest the robustness of MODPA with respect to changes in each of IOPs (TSS, Chl-a and CDOM) and also in optically complex rivers where all the IOPs as well the bottom types are variable. The extra predictors improved the results of MODPA in the testing scenario associated with the optically complex rivers (3 cm improvement of RMSE for depths up to 2 m). The simulated spectra comprise high concentrations of IOPs which are representative for turbid rivers in the study area (alpine rivers such as Sarca). However, more research should be dedicated to study turbid rivers to further explore the potentials of bathymetry models.

The enhanced spectral resolution of WV-2 showed benefits for mapping the bathymetry of shallow rivers. For instance, the long-wavelength bands including RE and NIR-1 demonstrated to be useful as Lyzenga predictors or as denominator of ratio predictors. This is mainly because the attenuation of light in shallow and clear rivers does not get saturated even for long/highly-absorbing wavelengths. On the other hand, short-wavelength bands (e.g. B, CB, G and Y) performed as appropriate numerator bands for the ratio predictor. In summary, WV-2 sensor provides wealth of options for selecting either Lyzenga or ratio predictors and leads to higher accuracies than when using conventional 4-band HRSI (e.g. improvements of R^2 and RMSE respectively on the order of 9% and 1 cm using TOA reflectances without extra predictors). The first tests on DigitalGlobe AComp indicate the effectiveness of this product for mapping the bathymetry of shallow and clearly flowing rivers. Comparing the TOA and AComp reflectances over a range of field-measured depths shows reasonable correction of atmospheric effects (e.g. appropriate removal of Rayleigh scattering over short wavelengths). AComp reflectances yield relatively higher accuracies than TOA data which is more pronounced for OBRA (improvements of R^2 and RMSE on the order of 11% and 1 cm, respectively). However, multiple-predictor models

particularly MODPA showed robust bathymetry retrievals with respect to atmospheric effects. More studies should be dedicated to comprehensively analyze the quality of AComp product for in general aquatic remote sensing.

The proposed MODPA provided promising results and improvements for bathymetry retrieval in shallow and clearly flowing rivers using HRSI. The best result derived from MODPA based on PLS regression using AComp reflectances of WV-2 where the R^2 and RMSE are estimated as 0.82 and 5.8 cm, respectively. Although three investigated regression methods provided very comparable results, the PLS-based regression showed slightly accurate results.

5.3 Riverbed Mapping

Although studies on bathymetry of rivers are becoming relatively mature, little work has been done to explore other essential attributes such as streambed compositions. In this research, retrieval of bottom reflectances and mapping riverbed types and compositions are addressed comprehensively. Unlike most of previous research, a physics-based approach is pursued to map the bottom properties by retrieving the bottom reflectances rather than using the above-water spectra. The proposed methodology accounts for the attenuation of the light in water column by estimation of the k_d parameter for which some known depths are required over a homogenous bottom type. Water depth of each pixel is needed along with the k_d parameter to retrieve the bottom reflectance. The proposed MODPA is used to derive the bathymetry that provided robust depth retrievals with respect to substrate and IOPs variability. The main advantage of the proposed framework is that the bottom reflectance retrieval is followed by bathymetry. This means that the portion of in-situ depths used for calibration of the bathymetric model and/or image-derived depths over a homogenous bottom type can be used for estimation of k_d, i.e. the key parameter for bottom reflectance retrieval, so that no further in-situ efforts are required for direct measurement of the k_d parameter.

As mapping the bottom compositions is at early stages in riverine environments, the bottom reflectance retrieval and accordingly mapping of substrate types are explored using a wide range of spectral data in this research. The spectroscopic measurements in the hydraulic lab and

simulations from radiative transfer modeling provided the study with a thorough understanding of streambed mapping and impacting factors such as water depth, IOPs, deep-water correction and spectral resolution. Further, as a first attempt to map substrate properties from space, 8-band WV-3 image of a reach in Sarca River is analyzed to classify SAV densities. The results from spectroscopic measurements and simulations suggest that the k_d and bottom reflectance retrievals are more accurate in the visible bands than in long wavelengths (i.e. NIR bands) particularly for relatively deep water (> 0.5 m). This would be attributed to the rapid attenuation of the NIR wavelengths in water column particularly when it is thicker. However, deep-water correction demonstrated to be effective to enhance the retrievals in NIR spectrum when the water goes deeper. This is reasonable as the main effect of deep-water correction is when the bottom reflectance approaches to zero. However, the effect of deep-water correction is negligible for visible bands in the range of water depths discussed in this study (< 1 m) as well as for the NIR bands in very shallow depths (< 0.5 m). Moreover, the effect of IOPs variability is investigated on the bottom reflectance retrieval of the simulated channel. It is inferred that when the depth samples, required for the k_d retrieval, are chosen from the part of simulated channel which is more representative for the IOPs of entire channel (i.e. downstream), the streambed clusters would be slightly more accurate. However, the results of clustering would be subjective to the level of spectral discrepancy of the bottom types. Further analysis regarding the impact of IOPs magnitude (level of turbidity) on the bottom reflectance retrievals revealed that the level of turbidity would have less of an impact on the reflectance retrievals in the visible bands while the RMSE of retrievals showed an upward trend for NIR bands by increasing the turbidity. However, the deep-water correction again mitigates the effect of turbidity on retrievals of bottom reflectances. For instance, the RMSE of reflectance retrieval for the macrophyte bottom reduces from 0.09 to 0.02 when applying the deep-water correction in the highly turbid water (Figure 4.26b). Another key finding is that the retrieved bottom reflectances lead to significantly more accurate results in mapping the substrate types rather than above-water spectra. For instance, the retrievals of three bottom types (dolomite, macrophyte and sediment) in the simulated channel enhanced the results of riverbed clustering on the order of 20% of overall accuracy and 30% of kappa coefficient compared to those of obtained from above-water spectra. This is also demonstrated in making distinction among SAV densities based on VIs where retrievals of bottom

reflectances yielded VI values strongly correlated to the macrophyte fractions. Of all band combinations used for terrestrial and aquatic VIs, the terrestrial VI with (RE, R) band combination is found to provide the highest correlation with the SAV fractions either using inferred bottom reflectances (R^2 = 0.85 and RMSE = 0.07) or above-water spectra (R^2 = 0.48 and RMSE = 0.2). This band combination also yielded the most accurate clusters of SAV densities using the lab spectra as well as the WV-3 image. More generally, the above-water spectra showed some potentials for detection of SAV with high densities using the WV-3 image (user accuracy= 45% and producer accuracy= 57%). This indicates the effectiveness of RE band of WV-2/WV-3 sensor in mapping the SAV densities which is strategically located over the characteristic spectral feature of vegetation (705-745 nm). In addition, the aquatic VIs yielded accuracies no higher than the terrestrial indices in terms of clustering SAV densities. Moreover, enhanced spectral resolution of the 8-band WV-3/WV-2 sensor provided higher accuracies (on the order of 5%) in mapping the streambed using simulated spectra. Note that the k_d retrieval in the NIR2 band is slightly less accurate than short wavelengths in NIR region (e.g. the NIR band of GeoEye). However, the improved clustering accuracies using 8-band WV-3/WV-2 indicate the overall efficacy of enhanced spectral resolution of this sensor compared to the traditional 4-band HRSI to map bottom compositions.

This study addressed the mapping of grain sizes as a key in-stream morphological attribute through a preliminary view about the feasibility of grain sizes/roughness retrieval using spectral data. The main assumption of the research was that the spectral signature of a streambed is influenced not only by the type but also by the size/roughness of the substrate. This assumption is validated by means of spectroscopic measurements over substrates with same material and different grain sizes. The spectroscopic observations suggest that an increase in the substrate sizes makes the bottom to appear brighter. This would be because of multiple scatterings occurred in the larger/rougher grains which reflect a larger portion of the downwelling radiance back to the sensor's field of view. The experiments demonstrate that the shapes of the spectra remain identical while the reflectance magnitudes (i.e. brightness) changes by an approximately constant scale depending on the change in grain sizes. Motivated by this finding, the simulations are performed with the bottom spectra associated with the different grain sizes observed in the lab to

investigate the feasibility of bottom reflectance retrieval and then clustering of the riverbed into grain size classes. The results from spectroscopic experiments and also simulations indicate the effectiveness of the water column correction method to retrieve bottom reflectances in a sufficient accuracy for clustering the grain sizes classes. The three grain size classes (fine, medium and coarse) are clustered using the retrieved bottom spectra for the simulated channel with overall accuracy of 92 % and kappa coefficient of 0.88 that indicates the high potential of spectral data for remotely mapping of grain sizes. Note that the existing variable IOPs across the channel imposes more complexities to the bottom reflectance retrieval and accordingly grain size clustering processes. However, the water column correction method demonstrated high performance to retrieve the bottom spectra.

5.4 Overall Conclusions and Suggestions

The exploitation of remote sensing techniques is of increasing importance for studying fluvial systems. Understanding and isolating the effect of each riverine attribute on the overall spectral response of water body would unlock valuable information contributing to a wide range of applications in fluvial systems. This can provide spatiotemporal insights into hydromorphological and ecological processes and could allow effective management of fluvial systems.

This research investigated three main elements of rivers hydromorphology including river boundaries, bathymetry and riverbed types and compositions. As first main goal of the research, reconstruction of river boundaries at sub-pixel resolution is investigated based on unmixing and SRM. The proposed OBA-NDWI for estimation of water fractions (i.e. unmixing) demonstrated that additional spectral bands of WV-2 imagery provide a couple of choices for selecting the proper pair of bands to form NDWI equation. Although the (CB, RE) pair is selected as the optimal combination of bands for Sarca River, other combinations such as (CB, NIR-2), (B, RE), and a few other combinations also demonstrated a strong relation with water fractions. In this regard, making use of several NDWIs to establish a multiple regression for the prediction of water fractions can potentially lead to maximum benefit from spectral bands which can be an area of investigation for future studies. Furthermore, the number and quality of endmembers can affect

the results of unmixing methods. The assumption regarding the three aforementioned endmembers is valid for constitution of the major land cover types (Ji et al., 2009; Wetherley et al., 2017). This is mainly because each of classes is representative for a major land cover which can consists of sub-classes with similar spectral responses (e.g. different vegetation types can be grouped into only one major vegetation class). However, in case of presence of an obviously different endmember in the riparian/buffer zone of river, the number of endmembers can be increased through the unmixing process using OBA-NDWI. In this case, identification of the optimal bands would be performed locally. The OBA-NDWI method can be applied in a segment-based approach to identify the optimal bands for each desired segment of the channel.

The second main goal of the research was focused on bathymetry retrieval where the proposed MODPA provided robust retrievals with respect to changes in bottom types, IOPs and atmospheric effects. This research suggests to explore additional extra predictors that can possibly be considered as extra predictors through MODPA such as spectral water indices. This would be beneficiary particularly for low spectral resolution imagery or for studies on optically complex waters. Also further studies should be dedicated to investigate the quality of AComp product for applications in aquatic remote sensing. The HAB model by incorporating some principles of open channel flow with bathymetric models demonstrated high potentials for inferring river bathymetry from optical imagery and only with known discharge. The future research would address the possibility of addressing river discharge and flow velocity from spectral data that only very recently some researches are emerging in this area (Legleiter et al., 2017a; Legleiter et al., 2017b).

The first attempt to retrieve bottom reflectances from space with a focus on mapping SAV densities demonstrated promising results and high potentials of the HRSI for substrate mapping in riverine environments. However, further studies needs to be dedicated to investigate this potential for mapping different benthic covers. This study also presented first experiences in mapping the grain sizes from spectral data. More investigations are needed to explore in detail the potentials and shortcomings of proposed methodology in real case studies and also by considering a wide range of bottom types and sizes as well as IOPs. This research also demonstrated the effectiveness of spectroscopic experiments in an indoor environment of a

hydraulic laboratory to study the bathymetry of very shallow waters considering variable bottom types. Experiments of this kind can be extended to study further attributes of fluvial systems such as flow velocity and water quality indicators (IOPs).

References

Abdi, H., 2003. Partial Least Square Regression (PLS Regression). In *Encyclopedia of Social Science Research Methods*; SAGE: Thousand Oaks, CA, USA, pp. 792–795.

Anker, Y., Hershkovitz, Y., Ben Dor, E., Gasith, A., 2014. Application of aerial digital photography for macrophyte cover and composition survey in small rural streams. *River Research and Applications*, 30, 925–937.

Arif, M.S.M., Gülch, E., Tuhtan, J.A., Thumser, P., and Haas, C., 2016. An investigation of image processing techniques for substrate classification based on dominant grain size using RGB images from UAV, *International Journal of Remote Sensing*.

Ashworth P.J., and Ferguson, R.I., 1986. Interrelationships of channel processes, changes and sediments in a proglacial braided river. *Geografiska Annaler*, 68: 361–371.

Atkinson, P.M., 2005. Sub-pixel target mapping from soft-classified Remotely sensed imagery, *Photogrammetric Engineering and Remote Sensing*, vol. 71, no. 7, pp. 839–846.

Atkinson, P.M., 2009. Issues of uncertainty in super resolution mapping and their implications for the design of an inter-comparison study, *International Journal of Remote Sensing*, vol. 30, no. 20, pp. 5293–5308.

Bailly J.S, Le Coarer, Y., Languille, P., Stigermark, C., Allouis, T., 2010. Geostatistical estimation of bathymetric LiDAR errors on rivers. *Earth Surface Processes and Landforms*, 35: 1199–1210.

Belletti, B.; Rinaldi, M.; Bussettini, M.; Comiti, F.; Gurnell, A.M.; Mao, L.; Nardi, L.; Vezza, P., 2017. Characterising physical habitats and fluvial hydromorphology: A new system for the survey and classification of river geomorphic units. *Geomorphology*, 283, 143–147.

Belward, A.S., Skøien, J.O., 2015. Who launched what, when and why; trends in global land-cover observation capacity from civilian earth observation satellites. *ISPRS Journal of Photogrammetry and Remote Sensing*, 103, pp. 115–128.

Bergeron, N., Carbonneau, P.E., 2012. Geosalar: innovative remote sensing methods for spatially continuous mapping of fluvial habitat at riverscape scale. In Fluvial Remote Sensing for Science and Management, Carbonneau PE, Piegay H (eds). Wiley-Blackwell: Chichester. pp. 193–213.

Bertoldi, W., Gurnell, A.M., Drake, N.A., 2011. The topographic signature of vegetation development along a braided river: results of a combined analysis of airborne lidar, color air photographs, and ground measurements. *Water Resources Research*, 47,W06525.

Bioucas-Dias, J.M., Plaza, A., Dobigeon, N., Parente, M., Du, Q., Gader, P., and Chanussot, J., 2012. Hyperspectral Unmixing Overview: Geometrical, Statistical, and Sparse Regression-Based Approaches. *IEEE Journal of Selected Topics in Applied Earth Observations and Remote Sensing*, VOL. 5, NO. 2, pp. 354-379. doi:10.1109/JSTARS.2012.2194696.

Bizzi, S., Demarchi, L., Grabowski, R.C., Weissteiner, C. J., Van de Bund, W., 2016. The use of remote sensing to characterize hydromorphological properties of European rivers, *Aquatic Sciences*, 78: 57. https://doi.org/10.1007/s00027-015-0430-7

Bramante, J.F., Raju, D.K., and Sin, T.M., 2013. Multispectral derivation of bathymetry in Singapore's shallow, turbid waters, *International Journal of Remote Sensing*, 34:6, 2070-2088, DOI: 10.1080/01431161.2012.734934.

Bryant, R.G., Gilvear, D.J., 1999. Quantifying geomorphic and riparian land cover changes either side of a large flood event using airborne remote sensing: River Tay, Scotland, *Geomorphology*, 29 (3/4): 307–321.

Carbonneau, P., Fonstad, M.A., Marcus, W.A., Dugdale, S.J., 2012. Making riverscapes real, *Geomorphology*, 137 (1), 74–86.

Carbonneau, P.E., Piégay, H., 2012. Introduction: The growing use of imagery in fundamental and applied river sciences. In Fluvial Remote Sensing for Science and Management, Carbonneau PE, Piegay H (eds). Wiley-Blackwell: Chichester. pp. 1-18.

Carpenter, S.R., and Lodge, D.M., 1986. Effect of submersed macrophytes on ecosystem processes. *Aquatic Botany*, 26:341-370.

Casado, M.R., Gonzalez , R.B., Kriechbaumer , T., and Veal, A., 2015. Automated Identification of River Hydromorphological Features Using UAV High Resolution Aerial Imagery. *Sensors*, 15, 27969-27989; doi:10.3390/s151127969

Cho, J.J., Mishra, D., and Wood, J., 2012. Remote Sensing of Submerged Aquatic Vegetation, Remote Sensing - Applications, Boris Escalante (Ed.), ISBN: 978-953-51-0651-7.

Conallin, J., Boegh, E., and Jensen, J.K., 2010. Instream physical habitat modelling types: an analysis as stream hydromorphological modelling tools for EU water resource managers, *International Journal of River Basin Management*, 8:1, 93-107, DOI: 10.1080/15715121003715123

Demarchi, L, Bizzi, S., Piégay, H., 2016. Hierarchical Object-Based Mapping of Riverscape Units and in-Stream Mesohabitats Using LiDAR and VHR Imagery. *Remote Sensing*. 8(2):97.

Demarchi, L., Bizzi, S., and Piégay, H., 2017. Regional hydromorphological characterization with continuous and automated remote sensing analysis based on VHR imagery and low-resolution LiDAR data. *Earth Surface Processes and Landforms*, 42, pp. 531–551.

Dennison, W.C.; Orth, R.J.; Moore, K.A.; Stevenson, J.C.; Carter, V.; Kollar, S.; Bergstrom, P.W.; Batiuk, R.A., 1993. Assessing water quality with submersed aquatic vegetation. *BioScience*, 43, 86–94.

Dierssen, HM, Zimmerman, RC, Leathers, RA, Downes, TV, Davis, CO. 2003. Ocean color remote sensing of seagrass and bathymetry in the Bahamas Banks by high-resolution airborne imagery. *Limnology and Oceanography*, 48: 444–455.

DigitalGlobe, 2009. White Paper: the benefits of the 8 spectral bands of WorldView-2. pp. 1-10.

DigitalGlobe, 2017, The DigitalGlobe Constellation. Accessible at: https://dg-cms-uploads-production.s3.amazonaws.com/uploads/document/file/223/Constellation_Brochure_for Web.pdf

Du, Z., Li, W., Zhou, D., Tian, L., Ling, F., Wang, H., Gui, Y., and Sun, B., 2014. Analysis of Landsat-8 OLI imagery for land surface water mapping, *Remote Sensing Letters*, 5:7, 672-681, DOI: 10.1080/2150704X.2014.960606.

Du, Z., Linghu, B., Ling, F., Li, W., Tian, W., Wang, H., Gui, Y., Sun, B., and Zhang, X., 2012. Estimating Surface Water Area Changes Using Time-Series Landsat Data in the Qingjiang River Basin, China. *Journal Applied Remote Sensing*, 6: 063609. doi:10.1117/1.JRS.6.063609.

Elmore, A.J., Mustard, J.F., Manning, S.J., and Lobell, D.B., 2000. Quantifying vegetation change in semiarid environments: Precision and accuracy of spectral mixture analysis and the normalized difference vegetation index. *Remote Sensing of Environment*, 73: 87–102.

Elosegi, A., Diez, J., Mutz, M., 2010. Effects of hydromorphological integrity on biodiversity and functioning of river ecosystems, *Hydrobiologia*, 657:199–215.

Feyisa, G.L., Meilby, H., Fensholt, R., and Proud, S.R., 2014. Automated Water Extraction Index: A new technique for surface water mapping using Landsat imagery. *Remote Sensing of Environment*, 140, pp. 23–35.

Flener, C., 2013. Estimating deep water radiance in shallow water: adapting optical bathymetry modeling to shallow river environments. *Boreal Environment Research*, 18: 488–502.

Flener, C., Lotsari, E., Alho, P., Käyhkö, J., 2012. Comparison of empirical and theoretical remote sensing based bathymetry models in river environments. *River Research and Applications*, 28 (1), 118-133.

Flynn, K., Chapra, S., 2014. Remote sensing of submerged aquatic vegetation in a shallow non-turbid river using an unmanned aerial vehicle. *Remote Sensing*, 6 (12), 12815–12836.

Flynn, N.J., Snook, D.L., Wade, A.J., Jarvie, H.P., 2002. Macrophyte and periphyton dynamics in a UK Cretaceous chalk stream: the River Kenneth a tributary of the Thames, *Science of The Total Environment, 282*–283, 143–257.

Fonstad, M.A. and Marcus, W.A., 2005. Remote sensing of stream depths with hydraulically assisted bathymetry (HAB) models. *Geomorphology*, 72(1–4): 320–339.

Fonstad, M.A., Dietrich, J.T., Courville, B.C., Jensen, J.L., and Carbonneau, P.E., 2013. Topographic structure from motion: a new development in photogrammetric measurement, *Earth Surface Processes and Landforms*, 38, 421–430.

Foody, G., 2006. Sub-Pixel Methods in Remote Sensing, In: Jong, S. M. d. and Meer, F. D. v. d. (Eds.), *Remote Sensing Image Analysis*, Springer.

Foody, G.M., Muslim, A.M., and Atkinson. P.M., 2005, Super resolution mapping of the waterline from remotely sensed data, *International Journal of Remote Sensing*, 26:24, 5381-5392, DOI: 10.1080/01431160500213292.

Foody, G.M., Muslim, A.M., Atkinson, P.M., 2003. Super-resolution mapping of the shoreline through soft classification analyses, in Geoscience and Remote Sensing Symposium. IGARSS '03. Proceedings. IEEE International , vol.6, no., pp.3429-3431 vol.6, 21-25 July 2003, doi: 10.1109/IGARSS.2003.1294811.

Ghisalberti, M., and Nepf, H.M., 2004. The limited growth of vegetated shear layers, *Water Resources Research*, 40, W07502, doi: 10.1029/2003WR002776.

Giardino, C., Brando, V.E., Dekker, A.G., Strömbeck, N., Candiani, G., 2007. Assessment of water quality in Lake Garda (Italy) using Hyperion. *Remote Sensing of Environment*, 109 (2), pp. 183-195.

Gilvear, D., Bryant, R., 2003. Analysis of aerial photography and other remotely sensed data, Tools in Fluvial Geomorphology (G.M. Kondolf and H. Piégay, editors), John Wiley and Sons, Chichester, England, pp. 135–169.

Gilvear, D.J., Bryant, R., Hardy, T. 1999. Remote sensing of channel geomorphology and instream fluvial processes, *Progress in Environmental Science*, 1:257–284.

Gilvear, D.J., Davids, C., Tyler, A.N., 2004. The use of remotelysensed data to detect channel hydromorphology: RiverTummel, Scotland. *River Research and Applications*, 20:795–811.

Gilvear, D.J., Waters, T.M., Milner, A.M., 1995. Image analysis of aerial photography to quantify changes in channel morphology and instream habitat following placer mining in interior Alaska, *Freshwater Biology*, 34:389–398.

Gitelson, A.A. and Kondratyev, K.Y., 1991, Optical models of mesotrophic and eutrophic water bodies. *International Journal of Remote Sensing*, 12, pp. 373–385.

Gordon H. R., and Ding, K., 1992. Self-shading of in-water optical instruments, *Limnology and Oceanography*, 37 (10).

Gordon, H.R., 1990. Radiometric considerations for ocean color remote sensors. *Applied Optics*. 29, 3228–3236.

Güneralp, I., Filippi, A.M., Hales, B.U., 2014, Influence of river channel morphology and bank characteristics on water surface boundary delineation using high-resolution passive remote sensing and template matching, *Earth Surface Processes and Landforms*, doi: 10.1002/esp.3560.

Haenlein, M., Kaplan, A.M., 2004. A beginner's guide to partial least squares analysis. Underst. Stat, 3, 283–297.

Hartigan, J.A., and Wong, M.A., 1979. Algorithm AS 136: A k-means clustering algorithm. *Appl. Stat.*, 28, 100–108.

Heylen, R., Burazerovic, D., and Scheunders, P., 2011. Fully constrained least squares spectral unmixing by simplex projection. *IEEE Transactions on Geoscience and Remote Sensing*, vol. 49, no. 11, pp. 4112-4122.

Heylen, R., Parente, M., and Gader, P., 2014. A Review of Nonlinear Hyperspectral Unmixing Methods, *IEEE Journal Of Selected Topics In Applied Earth Observations And Remote Sensing*, VOL. 7, NO. 6, pp. 1844-1868.

Heylen, R., Scheunders, P., Rangarajan, A., and Gader, P., 2015. Nonlinear Unmixing by Using Different Metrics in a Linear Unmixing Chain. *IEEE Journal of Selected Topics in Applied Earth Observations and Remote Sensing*, vol. 8, no. 6, pp. 2655-2664.

Hirpa, F.A., Hopson, T.M., Groeve, T.D., Brakenridge, G.R., Gebremichael, M., and Restrepo, P.J., 2013. Upstream satellite remote sensing for river discharge forecasting: Application to major rivers in South Asia, *Remote Sensing of Environment*, 131, pp. 140–151.

Hoey, T. B., and Ferguson, R. I., 1994. Numerical simulation of down- stream fining by selective transport in gravel bed rivers: Model development and illustration, *Water Resources Research*, 30, 2251–2260.

Horkaew, P., and Puttinaovarat, S., 2017. Entropy-Based Fusion of Water Indices and DSM Derivatives for Automatic Water Surfaces Extraction and Flood Monitoring. *ISPRS International Journal of Geo-Information*. 2017 (6), 301.

Hugue, F., Lapointe, M., Eaton, B.C., and Lepoutre, A., 2016. Satellite-based remote sensing of running water habitats at large riverscape scales: Tools to analyze habitat heterogeneity for river ecosystem management. *Geomorphology*, 253, pp. 353–369.

Hurcom, S.J., and Harrison, A.R., 1998. The NDVI and spectral decomposition for semi-arid vegetation abundance estimation. *International Journal of Remote* Sensing, 19: 3109–3125.

Jain, S. K., Singh, R. D., Jain, M. K., & Lohani, A. K., 2005. Delineation of flood-prone areas using remote sensing technique, *Water Resources Management*, 19,337–347.

Jarrett, R.D., 1984. Hydraulics of high-gradient streams. *Journal of Hydraulic Engineering*, 110 (11), 1519–1539.

Javernick, L., Brasington, J., and Caruso, B., 2014. Modelling the topography of shallow braided rivers using Structure-from-Motion photogrammetry. *Geomorphology*, 213: 166–182.

Jawak, S.D., and Luis, A.J., 2016. High-resolution multispectral satellite imagery for extracting bathymetric information of Antarctic shallow lakes ", Proc. SPIE 9878, Remote Sensing of the Oceans and Inland Waters: Techniques, Applications, and Challenges, 987819: doi:10.1117/12.2222769.

Jensen, J.R., 2000. *Introductory Digital Image Processing: A Remote Sensing Perspective*. Prentice Hall, Inc. Upper Saddle River, NJ 07458, ISBN-13: 978-0131453610.

Ji, L., Gong, P., Geng, X., and Zhao, Y., 2015. Improving the Accuracy of the Water Surface Cover Type in the 30 m FROM-GLC Product, *Remote Sensing*, 7, 13507-13527. doi:10.3390/rs71013507.

Ji, L., Zhang, L., and Wylie, B., 2009. Analysis of Dynamic Thresholds for the Normalized Difference Water Index. *Photogrammetric Engineering & Remote Sensing*, Vol. 75, No. 11, November 2009, pp. 1307–1317.

Jiang, H.; Feng, M., Zhu, Y., Lu, N., Huang, J., and Xiao, T. 2014. An Automated Method for Extracting Rivers and Lakes from Landsat Imagery. *Remote Sensing*, 6, 5067-5089.

Jordan, D.C., Fonstad, M.A. 2005. Two-dimensional mapping of river bathymetry and power using aerial photography and GIS on the Brazos River, Texas. *Geocarto*, 20(3): 1–8.

Kabiri, K., Pradhan, B., Shafri, H.Z.M., Mansor, S.B., Samimi-Namin, K., 2013. A Novel Approach to Estimate Diffuse Attenuation Coefficients for QuickBird Satellite Images: A Case Study

at Kish Island, the Persian Gulf. *Journal of the Indian Society of Remote Sensing*, 41 (4), 797-806.

Keshavaand, N., and Mustard, J.F., 2002. Spectral unmixing, *IEEE Signal Processing Magazine*, vol. 19, no. 1, pp. 44–57.

Kinzel, P.J., Legleiter, C.J., and Nelson, J.M. 2013. Mapping river bathymetry with a small footprint green LiDAR: Applications and challenges. *Journal of the American Water Resources Association*, 49(1): 183-204.

Kirk, J.T.O., 1996. *Light & Photosynthesis in Aquatic Ecosystems*, 2nd ed.; Cambridge University Press: Cambridge, UK.

Lane, C.R., Liu, H., Autrey, B.C., Anenkhonov, O.A., Chepinoga, V.V., and Wu, Q., 2014. Improved Wetland Classification Using Eight-Band High Resolution Satellite Imagery and a Hybrid Approach. *Remote Sensing*, 6, 12187-12216.

Lane, S.N., Widdison, P.E., Thomas, R.E., Ashworth, P.J., Best, J.L., Lunt, I.A., Sambrook Smith, G.H., Simpson, C.J., 2010. Quantification of braided river channel change using archival digital image analysis, *Earth Surface Processes and Landform*, 35(8), pp. 971–985.

Lapointe, M.F., and Carson, M.A., 1986. Migration patterns of an asymmetric meandering river: The Rouge River, Quebec, *Water Resources Research*, 22:731–743.

Leckie, D.G., Cloney, ED., Jay, C., and Paradine, D., 2005. Automated Mapping of Stream Features with High-Resolution Multispectral Imagery: An Example of the Capabilities, *Photogrammetric Engineering & Remote Sensing*. Vol. 71, No. 2, pp. 145–155.

Lee, Z. P., Du, K.P., and Arnone, R., 2005. A model for the diffuse attenuation coefficient of downwelling irradiance. Journal of Geophysical Research, 110, C02016. doi:10.1029/ 2004JC002275.1.

Lee, Z.P., Carder, K.L., Mobley, C.D., Steward, R.G., and Patch, J.S., 1998, Hyperspectral remote sensing for shallow waters: 1. A semianalytical model, *Applied Optics*, 37, 6329 – 6338.

Legleiter, C.J. 2012. Remote measurement of river morphology via fusion of LiDAR topography and spectrally-based bathymetry. *Earth Surface Processes and Landforms*, 37(5): 499-518.

Legleiter, C.J. 2013. Mapping river depth from publicly available aerial images. *River Research and Applications*, 29(6): 760-780.

Legleiter, C.J., 2015, Calibrating remotely sensed river bathymetry in the absence of field measurements: Flow REsistance Equation-Based Imaging of River Depths (FREEBIRD), *Water Resources Research*, 51, 2865–2884.

Legleiter, C.J., and Overstreet, B.T. 2012. Mapping gravel-bed river bathymetry from space. Journal of Geophysical Research-Earth Surface, 117(F04024): doi: 10.1029/2012jf002539.

Legleiter, C.J., and Roberts, D.A., 2009. A forward image model for passive optical remote sensing of river bathymetry. *Remote Sensing of Environment*, 113 (5): 1025-1045.

Legleiter, C.J., Kinzel, P.J., and Nelson, J.M. 2017b. Remote measurement of river discharge using thermal PIV and various sources of bathymetric information. *Journal of Hydrology*, 554 (Supplement C): 490-506.

Legleiter, C.J., Marcus, W.A. and Lawrence, R.L. 2002. Effects of sensor resolution of mapping in-stream habitats, Photogrammetric Engineering & Remote Sensing, 68(8):801–807.

Legleiter, C.J., Mobley, C.D., and Overstreet, B.T. 2017a. A framework for modeling connections between hydraulics, water surface roughness, and surface reflectance in open channel flows. Journal of Geophysical Research - Earth Surface, 122(9): 1715-1741.

Legleiter, C.J., Overstreet, B.T., Glennie, C., Zhigang, P., Fernandez-Diaz, J., and Singhania, A. 2016a. Evaluating the capabilities of the CASI hyperspectral imaging system and Aquarius bathymetric LiDAR for measuring channel morphology in two distinct river environments. *Earth Surface Processes and Landforms*, 41(3): 344-363.

Legleiter, C.J., Roberts, D.A., and Lawrence, R.L. 2009. Spectrally based remote sensing of river bathymetry. *Earth Surface Processes & Landforms*, 34(8): 1039-1059.

Legleiter, C.J., Roberts, D.A., Marcus, W.A, Fonstad, M.A., 2004. Passive optical remote sensing of river channel morphology and in-stream habitat: Physical basis and feasibility. *Remote Sensing of Environment*, 93, pp. 493–510.

Legleiter, C.J., Stegman, T.K., and Overstreet, B.T. 2016b. Spectrally based mapping of riverbed composition. *Geomorphology*, 264: 61-79.

Lesser, MP, Mobley, CD. 2007. Bathymetry, water optical properties, and benthic classification of coral reefs using hyperspectral remote sensing imagery. *Coral Reefs*, 26: 819–829.

Leuven, R.S.E., Pudevigne, I., and Teuww, R.M., 2002. Application of geographical information systems and remote sensing in river studies, Backhuys Publishers, Leiden, The Netherlands, pp. 246.

Li, L., Chen, Y., Xu, T., Liu, R., Shi, K., Huang, Ch., 2015a. Super-Resolution Mapping of Wetland Inundation from Remote Sensing Imagery Based on Integration of Back-Propagation Neural Network and Genetic Algorithm, *Remote Sensing of Environment*, 164, pp. 142-154.

Li, L., Chen, Y., Yu, X., Liu, R., Huang, C., 2015b. Sub-pixel flood inundation mapping from multispectral remotely sensed images based on discrete particle swarm optimization. *ISPRS Journal of Photogrammetry and Remote Sensing*, 101, pp. 10–21.

Li, W., Du, Zh., Ling, F., Zhou, D., Wang, J., Gui, Y., Sun B., and Zhang, X., 2013. A Comparison of Land Surface Water Mapping Using the Normalized Difference Water Index from TM, ETM+ and ALI, *Remote Sensing*, 5, 5530-5549.

Li, X., Zhang, Y., Bao, Y., Luo, J., Jin, X., Xu, X., Song, X., and Yang G., 2014. Exploring the Best Hyperspectral Features for LAI Estimation Using Partial Least Squares Regression. Remote Sensing, 6, pp. 6221-6241.

Ling, F., Du, Y., Li, X., Li, W., Xiao, F., and Zhang, Y., 2013. Interpolation-based super-resolution land cover mapping, *Remote Sensing Letters*, 4:7, 629-638.

Lira, J., 2006. Segmentation and morphology of open water bodies from multispectral images. *International Journal of Remote Sensing*, 27,4015–4038.

Louchard, E.M., Reid, R.P., Stephens, F.C., Davis, C.O., Leathers, R.A., Valerie, D.T., 2003. Optical remote sensing of benthic habitats and bathymetry in coastal environments at Lee Stocking Island, Bahamas: A comparative spectral classification approach. *Limnology and Oceanography*, 48 (2003), pp. 511–521.

Lyzenga, D.R., 1978. Passive remote sensing techniques for mapping water depth and bottom features. *Applied Optics*, 17, 379–383.

Lyzenga, D.R., 1981, Remote sensing of bottom reflectance and water attenuation parameters in shallow water using aircraft and Landsat data, *International Journal of Remote Sensing*, 2:1, 71-82.

Lyzenga, D.R., Malinas, N.P. and Tanis, F.J., 2006. Multispectral bathymetry using a simple physically based algorithm, *IEEE Transactions on Geoscience and Remote Sensing*, 44(8), 2251-2259.

Maddock, I, and Bird, D., 1996. The application of habitat mapping to identify representative PHABISM sites on the River Tavy, Devon UK. In 2nd International Symposium on Habitat Hydraulics,Vol. B. Leclerc M, Capra H, Valentin S, Boudreault A, Coˆte ´ Y (eds). INRSEAU; FQSA; IAHR-AIRH: Que ´bec, Canada; 203–214.

Maddock, I., 1999, The importance of physical habitat assessment for evaluating river health. *Freshwater Biology*, 41: 373-391.

Maglione, P., Parente, C., and Vallario, A., 2014. Coastline extraction using high resolution WorldView-2 satellite imagery. *European Journal of Remote Sensing*, 2014, 47: 685-699.

Mandlburger, G., Hauer, C., Wieser, M., and Pfeifer, N., 2015. Topo-Bathymetric LiDAR for Monitoring River Morphodynamics and Instream Habitats—A Case Study at the Pielach River. Remote Sensing, 7, 6160-6195.

Mandlburger, G., Pfennigbauer, M., Wieser, M., Riegl, U., and Pfeifer, N., 2016. Evaluation of a Novel UAV-Borne Topo-Bathymetric Laser Profiler. *The International Archives of the Photogrammetry, Remote Sensing and Spatial Information Sciences*, Volume XLI-B1, 2016 XXIII ISPRS Congress, 12–19 July 2016, Prague, Czech Republic.

Marchetti, G., 2017. Overall Grain Size Mapping from Sentinel 2 Images. MSc thesis. Politecnico di Milano.

Marcus, W. A., and Fonstad, M.A., 2008. Optical remote mapping of rivers at sub-meter resolutions and watershed extents, Earth Surface Processes & Landforms, 33(1), 4–24.

Marcus, W. A., and Fonstad, M.A., 2010. Remote sensing of rivers: The emergence of a subdiscipline in the river sciences, *Earth Surface Processes & Landforms*, 35(15), 1867–1872.

Marcus, W.A., Fonstad, M.A., Legleiter, C.J., 2012. Management applications of optical remote sensing in the active river channel. In Fluvial Remote Sensing for Science and Management, Carbonneau PE, Piegay H (eds). Wiley-Blackwell: Chichester.

Marcus, W.A., Legleiter, C.J., Aspinall, R.J., Boardman, J.W. and Crabtree, R.L. 2003. High spatial resolution hyperspectral mapping of in-stream habitats, depths, and woody debris in mountain streams. Geomorphology, 55(1-4): 363-380.

Maritorena, S., Morel, A., Gentili, B., 1994. Diffuse-reflectance of oceanic shallow waters influence of water depth and bottom albedo. Limnol. Oceanogr. 39 (7), 1689–1703.

Marteau, B., Vericat, D., Gibbins, C., Batalla, R.J., and. Green, D.R., 2017. Application of Structure-from-Motion photogrammetry to river restoration. Earth Surface Processes and Landforms, 42, 503–515.

Mather, P.M., 2004. *Computer Processing of Remotely Sensed Images*, Third Edition, John Wiley & Sons Ltd, England.

McFeeters, S.K., 1996. The use of the Normalized Difference Water Index (NDWI) in the delineation of open water features. *International Journal of Remote Sensing*, 17, 1425–1432.

Meitzen, K.M., Doyle, M.W., Thoms, M.C., Burns, C.E., 2013. Geomorphology within the interdisciplinary science of environmental flows, Geomorphology, 200 (2013) ,143–154.

Mertens, K.C., Verbeke, L.P.C., Ducheyne, E.I., and De Wulf, R., 2003. Using genetic algorithms in sub-pixel mapping, *International Journal of Remote Sensing*, vol. 24, no. 21, pp. 4241–4247.

Michez, A., Piégay, H., Toromanoff, F., Brogna, D., Bonnet, S., Lejeune, P., Claessens, H., 2013. LiDAR derived ecological integrity indicators for riparian zones: application to the Houille river in Southern Belgium/Northern France. Ecological Indicators 34: 627–640.

Mishra, D.R., Narumalani, S., Rundquist, D., Lawson, M., 2005. Characterizing the vertical diffuse attenuation coefficient for downwelling irradiance in coastal waters: implications for water penetration by high resolution satellite data. ISPRS Journal of Photogrammetry and Remote Sensing. 60 (1), 48–64.

Mitidieri, F., Papa, M.N., Amitrano, D., and Ruello, G., 2016. River morphology monitoring using multitemporal SAR data: preliminary results. *European Journal of Remote Sensing*, 49: 889-898.

Mobley, C.D., 1994. Light and water: Radiative transfer in natural waters. Academic: San Diego, USA.

Mobley, C.D., 1999. Estimation of the remote-sensing reflectance from above-surface measurements. *Applied Optics*, 38 (36), 7442–7455.

Mobley, C.D., and Sundman, L.K., 2008. Hydrolight 5, Ecolight5 User Guide, Sequoia Scientific, Inc., Bellevue.

Mobley, C.D., L.K. Sundman, C.O. Davis, J.H. Bowles, T.V. Downes, R.A. Leathers, M.J. Montes, W.P. Bissett, D.D.R. Kohler, R.P. Reid, E.M. Louchard, and A. Gleason, 2005. Interpretation of hyperspectral remote-sensing imagery by spectrum matching and look-up-tables. *Applied Optics*, 44(17), 3576-3592.

Moody, J. A., Troutman, B. M., 2002. Characterization of the spatial variability of channel morphology. *Earth Surface Processes and Landforms*, 27, 1251–1266.

Mouw, C.B., Greb, S., Aurin, D.A., DiGiacomo, P.M., Lee, Z., Twardowski, M., Binding, C., Hu, C., Ma, R., Moore, T., Moses, W., Craig, S.E., 2015. Aquatic color radiometry remote sensing of coastal and inland waters: challenges and recommendations for future satellite missions. *Remote Sensing of Environment*. 160, 15–30.

Mumby, P. J., and Edwards, A. J., 2000. Water column correction approaches. In E. P. Green, P. J. Mumby, A. J. Edwards, & C. D. Clark (Eds.), Remote sensing handbook for tropical coastal management. Paris: Unesco. 316 pp.

Muslim, A.M., Foody, G.M., and Atkinson, P.M., 2007. Shoreline Mapping from Coarse–Spatial Resolution Remote Sensing Imagery of Seberang Takir, Malaysia. *Journal of Coastal Research*, Volume 23, Issue 6: 1399-1408.

Neal, J., Schumann, G., Bates, P., Buytaert, W., Matgen, P., Pappenberger, F., 2009. A data assimilation approach to discharge estimation from space. *Hydrological Processes*, 3649:3641–3649.

Newson, M.D., and Newson, C.L., 2000. Geomorphology, ecology and river channel habitat: mesoscale approaches to basin-scale challenges. *Progress in Physical Geography*, 24: 195–217.

Niroumand-Jadidi, M. and Vitti, A., 2016b, Optimal Band Ratio Analysis of WorldView-3 Imagery for Bathymetry of Shallow Rivers (case Study: Sarca River, Italy), *ISPRS - International Archives of the Photogrammetry, Remote Sensing and Spatial Information Sciences*, Volume XLI-B8, 2016, pp. 361-364.

Niroumand-Jadidi, M., and Vitti, A., 2015. Sub-pixel mapping of water boundaries using pixel swapping algorithm (case study: Tagliamento River, Italy), Proc. SPIE 9638, Remote Sensing of the Ocean, Sea Ice, Coastal Waters, and Large Water Regions 2015, 96380G; doi:10.1117/12.2194579.

Niroumand-Jadidi, M., and Vitti, A., 2016a, Improving the accuracies of bathymetric models based on multiple regression for calibration (case study: Sarca River, Italy), Proc. SPIE 9999, *Remote Sensing of the Ocean, Sea Ice, Coastal Waters, and Large Water Regions 2016*, 99990Q (October 19, 2016); doi:10.1117/12.2242083.

O'Neill, J.D., Costa, M., Sharma, T., 2011. Remote sensing of shallow coastal benthic sub- strates: In situ spectra and mapping of eelgrass (Zostera marina) in the Gulf Islands National Park Reserve of Canada. *Remote Sensing*, 3 (5), 975.

Orr, H.G., Large, A.R.G., Newson, M.D. and Walsh, C.L., 2008. A predictive typology for characterizing hydromorphology. *Geomorphology*, 100: 32-40.

Otsu, N. 1979. A Threshold Selection Method from Gray-Level Histograms. *IEEE Transactions on Systems, Man, and Cybernetics*, 9: 62–66. doi:10.1109/TSMC.1979.4310076.

Overstreet, B.T., and Legleiter, C.J. 2017. Removing sun glint from optical remote sensing images of shallow rivers. *Earth Surf Processes & Landforms*, 42(2): 318-333.

Pacifici, F., Longbotham, N., and Emery, W.J., 2014. The Importance of Physical Quantities for the Analysis of Multitemporal and Multiangular Optical Very High Spatial Resolution Images, *IEEE Transactions on Geoscience and Remote Sensing*, 52 (10), pp. 6241-6256.

Pahlevan, N., Roger, J.-C., Ahmad, Z., 2017b. Revisiting short-wave-infrared (SWIR) bands for atmospheric correction in coastal waters. *Optics Express*, 25, pp. 6015-6035.

Pahlevan, N., Sarkar, S., Franz, B.A., Balasubramanian, S.V., and He, J., 2017a. Sentinel-2 MultiSpectral Instrument (MSI) data processing for aquatic science applications: Demonstrations and validations, *Remote Sensing of Environment*, 201, 47–56.

Pahlevan, N., Schott, J.R., Franz, B.A., Zibordi, G., Markham, B., Bailey, S., Schaaf, C.B., Ondrusek, M., Greb, S., Strait, C.M., 2017a. Landsat 8 remote sensing reflectance (Rrs) products: Evaluations, intercomparisons, and enhancements. *Remote Sensing of Environment*, 190, 289-301.

Pan, Z., Glennie, C.L., Hartzell, P.J., Fernandez-Diaz, J.C., Legleiter, C.J., and Overstreet, B.T., 2015. Performance Assessment of High Resolution Airborne Full Waveform LiDAR for Shallow River Bathymetry. *Remote Sensing*, 7(5): 5133-5159.

Parasiewicz P., 2001. MesoHABSIM: a concept for application of instream flow models in river restoration planning. *Fisheries*, 26: 6–13.

Parasiewicz P., 2007. The MesoHABSIM model revisited. *River Research and Applications*, 23: 893–903.

Philpot, W. D. 1988. Bathymetric mapping with passive multispectral imagery. *Applied Optics*, 28: 1569–1578.

Piégay, H., Alber, A., Slater, L., and Bourdin, L., 2009. Census and typology of braided rivers in the French Alps. *Aquatic Sciences*, 71: pp. 371–388.

Piégay, H., Kondolf, G.M, and Sear, D., 2016. Integrating geomorphological tools to address practical problems in river management and restoration. In Tools in Fluvial Geomorphology, Kondolf MG, Piégay H (eds). J Wiley and Sons: Chichester, UK.

Poff, N.L., Allan, J.D., Bain, M.B., Karr, J.R., Prestegaard, K.L., Richter, B.D., Sparks, R.E., Stromberg, J.C., 1997. The natural flow regime. *Bioscience*, 47: 769–784.

Poole, G.C., 2010. Stream hydrogeomorphology as a physical science basis for advances in stream ecology. *Journal of the North American Benthological Society*. 29 (1), 12–25.

Poppe, M.; Kail, J.; Aroviita, J.; Stelmaszczyk, M.; Giełczewski, M.; Muhar, S., 2016. Assessing restoration effects on hydromorphology in European mid-sized rivers by key hydromorphological parameters. *Hydrobiologia*, 769, 21–40.

Rice, S. P., and Church, M., 1996. Bed material texture in low order streams on the Queen Charlotte Islands, British Columbia, *Earth Surface Processes and Landforms*, 21, 1–18.

Rinaldi, M., Belletti, B., Bussettini, M., Comiti, F., Golfieri, B., Lastoria, B., Marchese, E., Nardi, L., Surian, N., 2017. New tools for the hydromorphological assessment and monitoring of European streams. *Journal of Environmental Management*, 202, pp. 363-378.

Robison, E.G., Beschta, R.L., 1989. Estimating stream cross-sectional area from wetted width and thalweg depth. *Physical Geography*, 10 (2), 190–198.

Shintani C., and Fonstad, M.A., 2017. Comparing remote-sensing techniques collecting bathymetric data from a gravel-bed river, *International Journal of Remote Sensing*, doi: 10.1080/01431161.2017.1280636.

Silva, T.S.F., Costa, M.P.F., Melack, J.M., Novo, E.M.L.M., 2008. Remote sensing of aquatic vegetation: theory and applications. *Environmental Monitoring and Assessment*, 140, 131–145.

Strayer, D.L., and Malcom, H.M, 2007. Submersed Vegetation as Habitat for Invertebrates in the Hudson River Estuary. *Estuaries and Coasts*. 30 (2): 253–264.

Sundermann, A., Antons, C., Cron, N., Lorenz, A. W., Hering, D. and Haase, P., 2011, Hydromorphological restoration of running waters: effects on benthic invertebrate assemblages. *Freshwater Biology*, 56: 1689–1702. doi:10.1111/j.1365-2427.2011.02599.x

Tamminga, A., Hugenholtz, C., Eaton, and Lapointe, M., 2015. Hyperspatial Remote Sensing of Channel Reach Morphology and Hydraulic Fish Habitat Using an Unmanned Aerial Vehicle (UAV): A First Assessment in the Context of River Research and Management. *River Research and Applications*, 31: 379–391.

Tatem, A.J., Lewis, H.G., Atkinson, P.M., and Nixon, M.S., 2001. Super resolution target identification from remotely sensed images using a Hopfield neural network, *IEEE Transactions on Geoscience and Remote Sensing*, vol. 39, no. 4, pp. 781–796.

Thomson, A.G, 1998. Supervised versus unsupervised methods for classification of coasts and river corridors from airborne remote sensing, *International Journal of Remote Sensing*, 19:17, 3423-3431, DOI: 10.1080/014311698214091.

Thornton, M.W., Atkinson, P.M., Holland, D.A., 2006. Super- resolution mapping of rural land cover objects from fine spatial resolution satellite sensor imagery. *International Journal of Remote Sensing*, 27, 473–491.

Tong, X., Xu, X., Plaza, A., Xie, H., Pan, H., Cao, W., Lv, D., 2016. A new genetic method for subpixel mapping using hyperspectral images. *IEEE Journal of Selected Topics in Applied Earth Observations and Remote Sensing*. 9, 4480–4491.

Tran, T.V., Julian, J.P., and de Beurs, K.M., 2014. Land Cover Heterogeneity Effects on Sub-Pixel and Per-Pixel Classifications. *ISPRS International Journal of Geo-Information*. 2014 (3), pp. 540-553.

Trepel, M., and Kluge, W., 2002. Ecohydrological characterization of a degenerated valley peatland in Northern Germany for use in restoration, *Journal for Nature Conservation*, 10 (3), pp. 155–169.

Vargas-Luna, A., Crosato, A., Uijttewaal, W.S.J., 2015. Effects of vegetation on flow and sediment transport: comparative analyses and validation of predicting models. *Earth Surface Processes and Landforms*, 40 (2), 157-176.

Vaughan, I.P., Diamond, M., Gurnell, A.M., Hall, K.A., Jenkins, A., Milner, N.J., Naylor, L.A., Sear, D.A., Woodward, G. and Ormerod, S.J., 2009. Integrating ecology with hydromorphology: a priority for river science and management. *Aquatic Conservation: Marine and Freshwater Ecosystems*, 19: 113-125.

Vezza, P., Parasiewicz, P., Spairani, M., and Comoglio, C., 2014. Habitat modelling in high gradient streams: the meso-scale approach and application. *Ecological Applications*. 24(4): 844-861.

Villa, P., Mousivand, A., and Bresciani, M., 2014. Aquatic vegetation indices assessment through radiative transfer modelling and linear mixture simulation, *International Journal of Applied Earth Observation and Geoinformation*, vol. 30, pp. 113–127.

Visser, F., Buis, K., Verschoren, V., Meire, P., 2015. Depth Estimation of Submerged Aquatic Vegetation in Clear Water Streams Using Low-Altitude Optical Remote Sensing. *Sensors*, 15(10): 25287-25312. doi:10.3390/s151025287.

Visser, F., Wallis, C., Sinnott, A.M., 2013. Optical remote sensing of submerged aquatic vegetation: opportunities for shallow clear water streams. *Limnologica-Ecology and Management of Inland Waters*, 43 (5), 388–398.

Walther, S.C., Marcus, W.A., Fonstad, M.A., 2011. Evaluation of high resolution, true colour, aerial imagery for mapping bathymetry in a clear water river without ground-based depth measurements. *International Journal of Remote Sensing*, 32 (15), pp. 4343–4363.

Wang, L.G. and Wang, Q.M., 2013. Subpixel mapping using Markov random field multiple spectral constraints from subpixel shifted remote sensing images, *IEEE Geoscience and Remote Sensing Letters*, vol. 10, no. 3, pp. 598–602.

Wang, Q., Atkinson, P.M., and Shi, W., 2015a. Fast Subpixel Mapping Algorithms for Sub-pixel Resolution Change Detection. *IEEE Transactions on Geoscience and Remote Sensing*, VOL. 53, NO. 4.

Wang, Sh., Baig, M.H.A., Zhang, L., Jiang, H., Ji, Y., Zhao, H., Tian, J., 2015b. A Simple Enhanced Water Index (EWI) for Percent Surface Water Estimation Using Landsat Data, *IEEE Journal of Selected Topics in Applied Earth Observations and Remote Sensing*, vol.8, no.1, pp.90-97.

Westaway, R.M., Lane, S.N., and Hicks, D.M., 2001. Airborne remote sensing of clear water, shallow, gravel-bed rivers using digital photogrammetry and image analysis. *Photogrammetric Engineering and Remote Sensing*, 67: pp. 1271–1281.

Wetherley, E.B., Roberts, D.A., McFadden, J., 2017. Mapping spectrally similar urban materials at sub-pixel scales. *Remote Sensing of Environment*, 195, pp. 170–183.

Whiteside, T.G., and Bartolo , R.E., 2015. Mapping Aquatic Vegetation in a Tropical Wetland Using High Spatial Resolution Multispectral Satellite Imagery. *Remote Sensing*, 7(9), 11664-11694; doi:10.3390/rs70911664

Winterbottom, S.J. and Gilvear, D.J., 1997. Quantification of channel bed morphology in gravel-bed rivers using airborne multispectral imagery and aerial photography. *Regulated Rivers: Research and Management*, 13: pp. 489-499.

Wolf, A.F., 2012. Using WorldView-2 Vis-NIR multispectral imagery to support land mapping and feature extraction using normalized difference index ratios, Proc. SPIE 8390, Algorithms and Technologies for Multispectral, Hyperspectral, and Ultraspectral Imagery XVIII, 83900N, doi:10.1117/12.917717.

Wolf, P., Rößler, S., Schneider, T., Melzer, A., 2013. Collecting in situ remote sensing reflectances of submersed macrophytes to build up a spectral library for lake monitoring. *European Journal of Remote Sensing*. 46, 401–416.

Woodget, A.S., Carbonneau, P.E., Visser, F., and Maddock, I.P., 2014. Quantifying submerged fluvial topography using hyperspatial resolution UAS imagery and structure from motion photogrammetry. *Earth Surface Processes and Landforms*, 40: 47–64.

Wu, C., 2004. Normalized spectral mixture analysis for monitoring urban composition using ETM+ imagery. *Remote Sensing of Environment*, 93 (4): pp. 480–492.

Xiao, J., Moody, A., 2005. A comparison of methods for estimating fractional green vegetation cover within a desert-to-upland transition zone in central New Mexico, USA. *Remote Sensing of Environment*, 98: 237–250.

Xiao, J., Moody, A., 2005. A comparison of methods for estimating fractional green vegetation cover within a desert-to-upland transition zone in central New Mexico, USA. *Remote Sensing of Environment*, 98: 237–250.

Xiaocheng, Z., Tamas, J., Chongcheng, C., and Malgorzata, W.V., 2012. Urban Land Cover Mapping Based on Object Oriented Classification Using WorldView 2 Satellite Remote Sensing Images. In Proceedings of International Scientific Conference on Sustainable Development & Ecological Footprint, Sopron, Hungary.

Xie, C., Huang, X., Zeng, W., and Fang, X., 2016. A novel water index for urban high-resolution eight-band WorldView-2 imagery, *International Journal of Digital Earth*, DOI: 10.1080/17538947.2016.1170215.

Xu, Y. and Huang, B., 2014. A spatio-temporal pixel-swapping algorithm for subpixel land cover mapping, *IEEE Geoscience and Remote Sensing Letters*, vol. 11, no. 2, pp. 474–478.

Xu. H., 2006. Modification of normalised difference water index (NDWI) to enhance open water features in remotely sensed imagery, *International Journal of Remote Sensing*, 27, pp. 3025–3033.

Zhang, L., Wu, K., Zhong, Y., and Li, P., 2008. A new sub-pixel mapping algorithm based on a BP neural network with an observation model. *Neurocomputing*, vol. 71, no. 10–12, pp. 2046–2054.

Zoffoli, M.L., Frouin, R., Kampel, M., 2014. Water column correction for coral reef studies by remote sensing. *Sensors*, 14 (9), 16881–16931.